Winter 2017

Shining Light on The Phase Transitions of Vanadium Dioxide

Tyler J. Huffman
College of William and Mary - Arts & Sciences, tjhuffman@protonemail.com

Recommended Citation

Huffman, Tyler J., "Shining Light on The Phase Transitions of Vanadium Dioxide" (2017). *Dissertations, Theses, and Masters Projects.* Paper 1499450049.
http://doi.org/10.21220/S2607K

Shining Light on the Phase Transitions of Vanadium Dioxide

Tyler James Huffman

Kittanning, Pennsylvania

Bachelor of Science, Muhlenberg College, 2010
Master of Science, College of William & Mary, 2012

A Dissertation presented to the Graduate Faculty
of The College of William & Mary in Candidacy for the Degree of
Doctor of Philosophy

Department of Physics

College of William & Mary
May, 2017

APPROVAL PAGE

Dissertation is submitted in partial fulfillment of
the requirements for the degree of

Doctor of Philosophy

Tyler J. Huffman

Tyler J. Huffman

Approved by the Committee, March, 2017

Committee Chair
Associate Professor M. Mumtaz Qazilbash, Physics
College of William & Mary

Professor Henry Krakauer, Physics
College of William & Mary

Associate Professor Irina Novikova, Physics
College of William & Mary

Gina L. Hoatson

Professor Gina L. Hoatson, Physics
College of William & Mary

Robert D. Pike

Floyd Dewey Gottwald, Sr. Professor Robert D. Pike, Chemistry
College of William & Mary

ABSTRACT

The salient feature of the familiar structural transition accompanying the thermally-driven metal-insulator transition in bulk vanadium dioxide (VO_2) is a pairing of all the vanadium ions in the monoclinic M_1 insulating phase. Whether this pairing (unit cell doubling) alone is sufficient to open the energy gap has been the central question of a classic debate which has continued for almost sixty years. Interestingly, there are two less familiar insulating states, monoclinic M_2 and triclinic, which are accessible via strain or chemical doping. These phases are noteworthy in that they exhibit distinctly different V-V pairing. With infrared and optical photon spectroscopy, we investigate how the changes in crystal structure affect the electronic structure. We find that the energy gap and optical inter-band transitions are insensitive to changes in the vanadium-vanadium pairing. This result is confirmed by DFT+U and HSE calculations. Hence, our work conclusively establishes that intra-atomic Coulomb repulsion between electrons provides the dominant contribution to the energy gap in all insulating phases of VO_2.

VO_2 is a candidate material for novel technologies, including ultrafast data storage, memristors, photonic switches, smart windows, and transistors which move beyond the limitations of silicon. The attractiveness of correlated materials for technological application is due to their novel properties that can be tuned by external factors such as strain, chemical doping, and applied fields. For advances in fundamental physics and applications, it is imperative that these properties be measured over a wide range of regimes. Towards this end, we study a single domain VO_2 crystal with polarized light to characterize the anisotropy of the optical properties. In addition, we study the effects of compressive strain in a VO_2 thin film in which we observe remarkable changes in electronic structure and transition temperature. Furthermore, we find evidence that electronic correlations are active in the metallic rutile phase as well.

VO_2 films exhibit phase coexistence in the vicinity of the metal-insulator transition. Using scanning near-field infrared microscopy, we have studied the patterns of phase coexistence in the same area on repeated heating and cooling cycles. We find that the pattern formation is reproducible each time. This is an unexpected result from the viewpoint of classical nucleation theory that anticipates some degree of randomness. The completely deterministic nature of nucleation and growth of domains in a VO_2 film with imperfections is a fundamental finding. This result also holds promise for producing reliable nanoscale VO_2 devices

Table of Contents

ACKNOWLEDGEMENTS

I wish to express my sincerest appreciation for Professor Mumtaz Qazilbash. His commitment, drive, persistence, and talent are unrivaled. It was a particular privilege to work with him during the earliest stages of his lab. It involved a great deal of trust, and no small amount of risk, to give me that opportunity. I will be forever grateful.

I couldn't have asked for better collaborators. It's been a pleasure.

I owe my sincerest thanks to each and every one of my fellow students in the lab. I've learned something from each and every one of you. More important has been the support and companionship along the way.

M, this one is for you.
I could not have done this without you.
Thanks, again, for everything.

SHINING LIGHT ON THE INSULATING PHASES OF VANADIUM DIOXIDE

Chapter 1

Motivation and introduction

Although the ions and electrons that serve as the building blocks for all condensed matter systems are extremely well understood, the properties that emerge when many of these particles interact strongly are anything but. After quantum mechanics had taken form, Dirac observed[1]:

> "The underlying physical laws necessary for the mathematical theory of a large part of physics and the whole of chemistry are thus completely known, and the difficulty is only that the exact application of these laws leads to equations much too complicated to be soluble."

While Dirac was quite correct in principle, we find that, in direct conflict with the reductionist hypothesis, that the emergent properties of a complex, collective system cannot be extrapolated from the component parts in a straight-forward manner[2]. The problem lies not with reductionism itself, but with the corollary proposition of *constructionism*; the individual electrons and ions that constitute fundamental building blocks of these systems are not necessarily the appropriate objects for gaining insight into emergent physics.

Condensed matter physics has been remarkably successful in applying the principles of quantum mechanics with various approximation schemes to explain "simple" systems such as silicon and gold, where particles do not interact strongly with each other. Nevertheless, for a nontrivial strongly interacting system, these approximations break down, and an exact – or often even a qualitatively correct - quantum mechanical calculation from first principles is not merely inconvenient for a human to solve by hand, but can exceed what can be simulated in a finite time.

Handling the complexity of these systems is not simply a matter of applying quantum mechanics. New insights beyond quantum mechanics may be necessary. Through this lens, condensed matter physics should be viewed not merely as applied quantum mechanics, but as a new field which focuses on comprehending this complexity. Investigating this complexity requires a joint experimental and theoretical effort. Experiment provides critical insights and constraints necessary to guide theory in formulating new paradigms for accurately modeling correlated systems.

The difficulties of complexity and scale would perhaps be purely academic concerns were it not for the novel emergent properties of these systems, which include high temperature superconductivity, colossal magnetoresistance, multiferroicity, and metal-insulator transitions. The potential for applications lies not just in these novel properties themselves, but in that strong interactions lead to extreme sensitivity of these properties to external factors such as strain, temperature, chemical doping, and applied fields. An understanding sufficient to predict the conditions necessary for desired properties to emerge – in essence, the ability to design these systems – is, without hyperbole, the holy grail of materials science. Additional complications arise when the translation symmetry of the crystal lattice is broken by the defects, chemical impurities, and microstructure inherent in real materials. These factors can lead to novel and unexpected effects, such as phase coexistence and pattern formation on the nanoscale. Such phenomena offer further potential for applications. Thus, developing a useful framework for understanding and controlling strongly interacting systems is of interest to applied science as well as fundamental physics.

Our best hope to tackle this problem lies in abstraction; that is, to approach the problem in a way that is decidedly non-reductionist. This sort of abstraction has been quite successful historically in the sciences. For example, Mendel did not need the details of the carbon, nitrogen, phosphorus, oxygen, and hydrogen atoms that make up DNA to father the field of genetics. Instead, it was more insightful – more powerful – to think in terms of the genes themselves. Instead of focusing on the individual electrons and ions that make up condensed matter systems, it's often more useful to think about objects like the lattice, phonons, bands, energy gaps, spin and charge density waves, et cetera. These collective/emergent phenomena, which exist as a consequence of the many particles of the solid, are generally the relevant degrees of freedom in these materials.

As a consequence of the strong interactions between the fundamental particles, these degrees of freedom also interact strongly. Correlated materials are so sensitive to factors such as chemical purity and strain that it is imperative to track all of the relevant degrees of freedom to gain a clear experimental picture. Failure to do so can lead to unsubstantiated assumptions about the untracked degrees of freedom and thus undue importance might be assigned to the degrees of freedom that are being actively observed. With broadband photon spectroscopy, we are able to cover almost 4 decades of energy to track many of the relevant degrees of freedom in condensed matter systems. While specialized techniques may sometimes be necessary to provide additional detail or confirmation, photon spectroscopy serves as the ideal primary technique for experimental studies of these systems.

Broadband photon spectroscopy is perhaps *the* natural technique for humans to gain understanding of our world. In some sense, it is a simple generalization of human color vision outside the visible spectrum (λ=0.4 to 0.7 µm), into the very far infrared (≈100 µm) and the ultraviolet (≈0.2 µm). Traditionally in spectroscopy, either the inverse wavelength ($\nu = 1/\lambda$) expressed in inverse centimeters (cm^{-1}) or the phonon energy ($hc\nu$) is used instead of the wavelength. The raw experimental data is acquired as a transmission spectrum ($T(\nu)$), a reflectance spectrum $R(\nu)$ or as spectroscopic ellipsometric coefficients ($\psi(\nu)$and $\Delta(\nu)$). This data is analyzed using Kramers-Kronig consistent oscillators to extract the optical constants, which can either be expressed as the complex dielectric function ($\hat{\varepsilon}(\nu)$), the complex conductivity ($\hat{\sigma}(\nu)$) or the complex index of refraction ($\hat{N}(\nu)$). These quantities contain the same information about the response of the material to light. In some situations, one of these techniques may not be appropriate, for example transmission in regions of the spectrum where the sample is opaque. Nevertheless, in the event that both the real and imaginary optical constants can be determined in some region of the spectrum - for example, if $R(\nu)$ is measured at low frequencies and $\psi(\nu)$ and $\Delta(\nu)$ are measured at higher frequencies - the optical constants can typically be extracted with an uncertainty on the order of 1% over the entire spectral range.

While correlated systems are incredibly diverse, a quite general characteristic of these materials is a partially filled valence *d* or *f* orbitals. The electrons in these orbitals experience, for example, stronger Coulomb repulsion because of their higher degree of spatial confinement. Many of these systems have large unit cells, complicated stoichiometry, and require chemical doping to induce the novel properties we're interested in. Following the example of Mendel, we choose a relatively simple yet representative system, as the more complicated systems, while interesting, could obfuscate the understanding we seek. Vanadium dioxide (VO_2) will serve as our *drosophila* – a comparatively simple system to observe and draw conclusions which could be quite broadly applicable. Vanadium dioxide's relatively simple unit cell, simple stoichiometric formula, and the fact that it experiences a metal-insulator transition near room temperature makes it an ideal candidate for study. Moreover, there is only one correlated *d*-electron per vanadium atom to consider. Nevertheless, even in this "simple" correlated system, the physics is incredibly rich. A deep look into the properties and history of research on VO_2 gives one an appreciation for the depth of the correlated electron problem, the potential of these systems to drive disruptive technology, and the challenges these systems pose to researchers (See Chapter 2).

In VO_2, the vanadium ions are in the 4+ valence state. The single unpaired $3d$ $3d$ electron implies an unfilled valence band. Thus one might naively expect the material to be a metal at all temperatures. However, the insulating behavior arises when the bulk material is cooled below 340K. The thermally-driven metal-insulator transition (MIT) is accompanied by a structural transition between the insulating monoclinic M_1 and metallic rutile phases (See Fig. 1.1). The insulating behavior arises as a result of the splitting of the valence (a_{1g}) band and the upshift of the e_g^π bands such that an energy gap of ≈0.6 eV occurs between the valence $\mathrm{a_{1g}}$ band and the e_g^π band. Since the 1950s, the specific mechanism that leads to insulating behavior has been the subject of a glorious debate which has involved several prolific researchers, including Sir Neville Mott himself. While the details will be discussed more thoroughly in Chapter 2, VO_2 researchers generally have fallen into two factions. The first, proponents of the Peierls mechanism, argue that the insulating behavior arises as a consequence of the change in lattice structure. In the Peierls picture, unit cell doubling leads to splitting of the bands at the Brillouin zone boundary, which now corresponds to the Fermi energy in the doubled unit cell. The second camp argues for the Mott-Hubbard mechanism: that the splitting

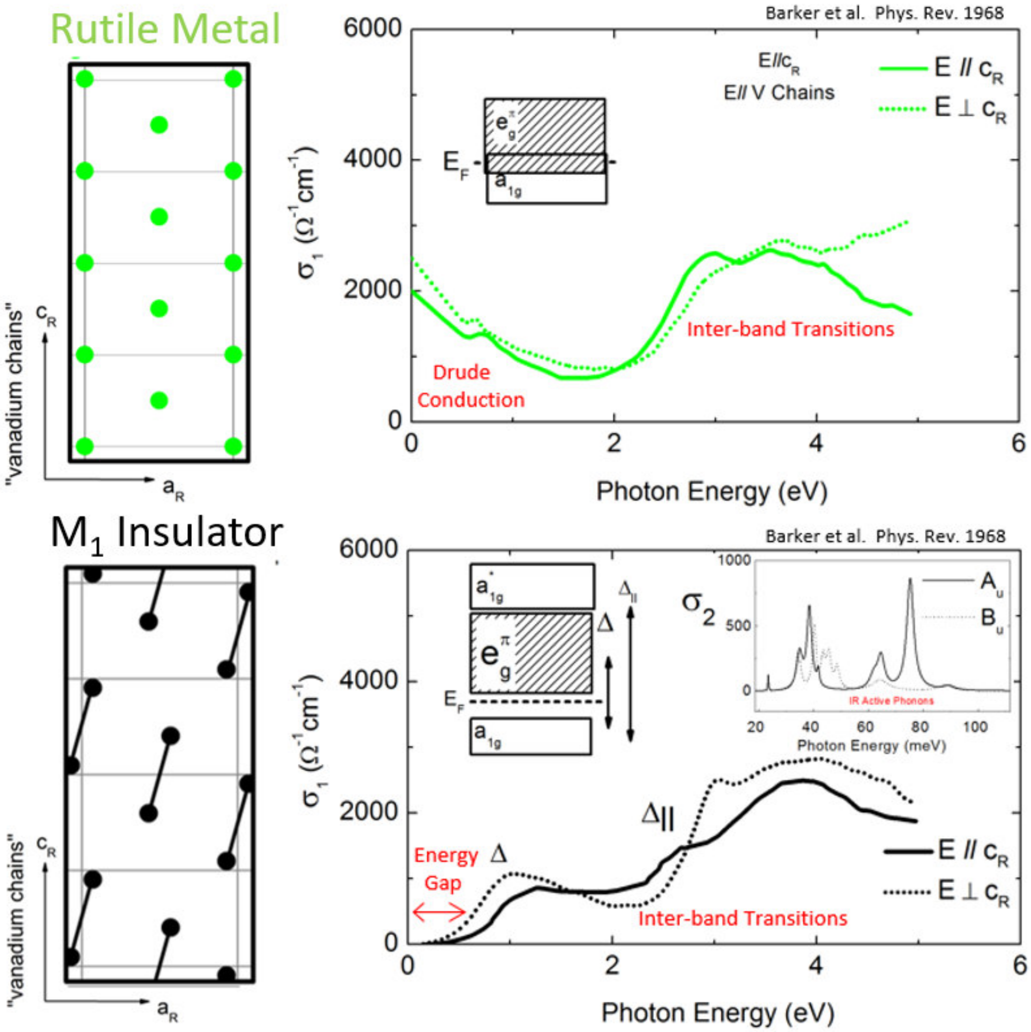

Figure 1.1 — Lattice structure schematics and conductivity spectra for the rutile metal (green) and insulating M_1 (black) phases in bulk VO_2. Notable spectral features are annotated (red).

results from strong intra-atomic coulomb repulsion in the a_{1g} band. In the picture, the structural transition alone cannot lead to the insulating phase, and electronic correlations dominate the opening of the gap. Ultimately the primary question in VO_2 research is to uncover the connection between the lattice structure and the electronic properties. Infrared spectroscopy is ideally suited for this purpose because it can track both the electronic orbitals, through the inter-band transitions, and the lattice structure, through the infrared active phonons (See Fig. 1.1).

This thesis is organized as follows: we start with a review of the material and description of the current state of the field in Chapter 2. In Chapter 3, the anisotropic infrared response of a single domain VO_2 crystal is determined. In Chapter 4, a study of two additional insulating lattice structures, monoclinic M_2 and triclinic (T), settles the longstanding debate over the cause of insulating behavior in favor of electronic correlations. In Chapter 5, shifts in the electronic structure are observed in a compressively strained VO_2 film. In Chapter 6, we report that the patterns of phase coexistence that occur in the vicinity of T_c are reproducible each time the VO_2 film is cycled through the metal-insulator transition.

Chapter 2

Overview of VO_2

2.1 PROLOGUE

That VO_2 undergoes a metal-insulator transition (MIT) at 340K was discovered by Morin in 1959[3]. The emergence of insulating behavior was surprising, as the material was expected to have a partly filled band, and thus, according to "Wilson's Rule" should be metallic at all temperatures[4]. Shortly thereafter, various mechanisms were proposed outlining how Wilson's rule might be violated, most notably via electronic correlations[5] or lattice distortion[6]. Complications arise as the VO_2 system has features reminiscent of both mechanisms. For reasons that will be made clear later, decoupling the two effects has proven to be highly nontrivial. As a result, the insulating phases of VO_2 have gone unclassified – and ultimately unexplained – for more than half a century.

In this chapter, my aim is to present a self-contained and coherent account of research on the VO_2 problem. Given the long history of the field and the iterative nature of research, a purely historical approach may not be the best approach. Instead, I contend that the history of the physics of VO_2 is best understood with the benefit of hindsight. I abandon any pretense of a chronological treatment in the interest of clarity and impact. The chapter is thus organized as follows:

In Section 2.2, the settled experimental facts regarding the lattice structure of the VO_2 phases, including the monoclinic M_2 and T insulating phases, which can be accessed by strain or chemical doping, are presented. The lattice structures of the M_2 and T phases suggests a powerful framework – the idea that the vanadium atoms form quasi-1 dimensional (1D) chains along the c_r axis - that reveals a deep connection between all four lattice structures.

In Section 2.3, the classic works of J.B. Goodenough in 1971 and Zylbersztejn and Mott in 1975 are summarized. These serve as the canonical works of the Peierls and Mott-Hubbard sides of the debate, respectively. These summaries serve to build a rigorously defined vocabulary to discuss later works.

In Section 2.4, now that the necessary foundation has been laid, we establish the experimental facts about the VO_2 system. Experimental facts are discussed within the framework established in Section 2.2 and Section 2.3 where appropriate.

Here, I purposefully focus on the uncontentious and well characterized properties of the material.

A number of more modern VO_2 studies - despite the high quality of the experimental and computational work - have reached very strong and often contradictory conclusions. These studies are summarized and discussed in Section 2.5.

2.2 LATTICE STRUCTURE

Ultimately, a solution to the VO_2 problem describes the connection between the lattice structure and the electronic properties. While the bulk material only exhibits the rutile and M_1 lattice structures, two additional lattice structures - monoclinic M_2 and triclinic (T) - are accessible by chemical doping[7], tensile strain along c_R[8], and compressive strain along $(110)_R$[9] (See Fig. 2.1). While some might argue that the M_2 and T phases are somehow superfluous, we emphasize that any complete explanation of VO_2 *necessarily* includes all four phases. Moreover, as will become clear presently, the four lattice structures are deeply related.

The lattice structures of the four phases were well characterized in the x-ray diffraction (XRD) works of Longo, Kirkengard, Ghedira, McWhan, Marezio,

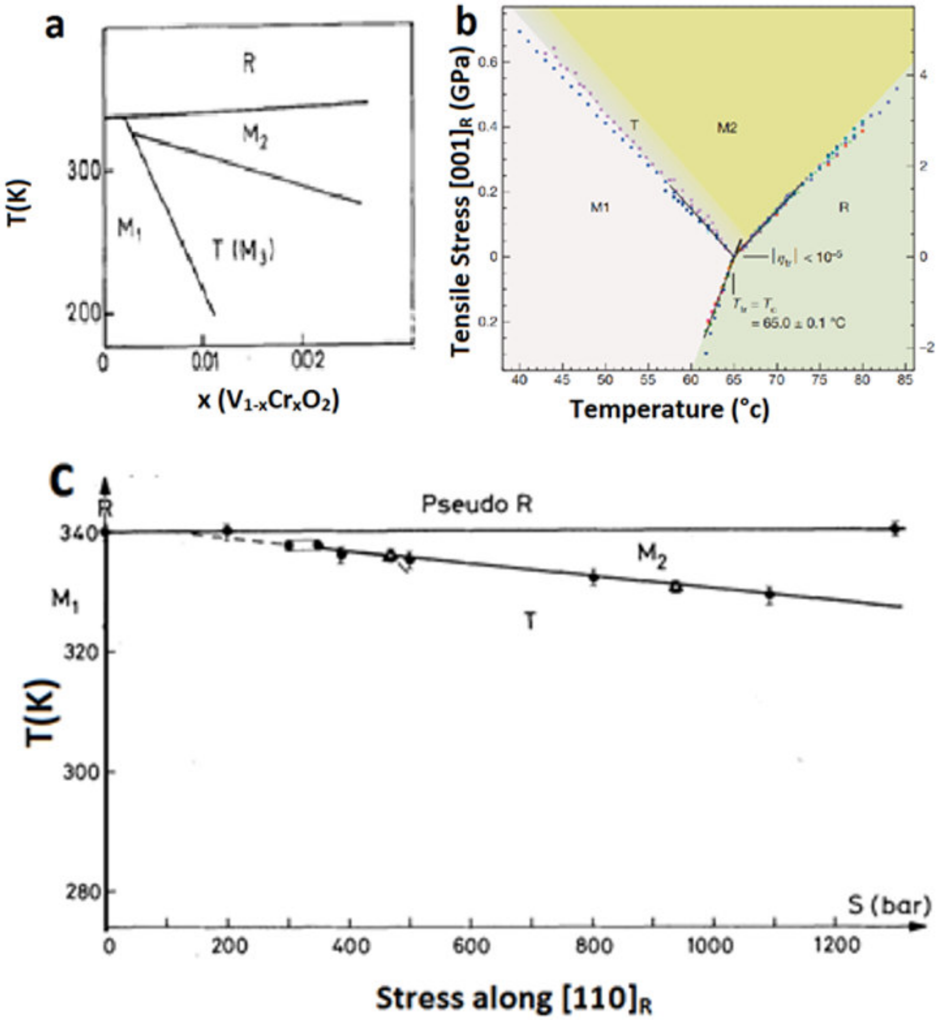

Figure 2.1 — (a) Phase diagram of $V_{1-x}Cr_xO_2$ as a function of chromium doping[7]. (b) and (c) Strain-temperature phase diagram of pure VO_2 for strain (b) along c_R [8] and (c) along $[110]_R$ [9].

and others[10–16]. The approximate relations between the rutile phase and these these three phases are shown in table 2.1.

It is noteworthy that the monoclinic phases do not share a 2-fold rotation axis (b_m). In the M_1 phase, the 2-fold axis (b_{M1}) is oriented along a_R, while b_{M2} is oriented along c_R. Due to the γ and α angles in the triclinic structure being very

M_1	$c_R \leftrightarrow a_{M1}$	$a_R \leftrightarrow b_{M1}$	$a_R - c_R \leftrightarrow c_{M1}$
M_2	$2c_R \leftrightarrow b_{M2}$	$a_R \leftrightarrow -c_{M2}$	$a_R \leftrightarrow a_{M2}$
T	$2c_R \leftrightarrow b_T$	$a_R \leftrightarrow c_T$	$a_R \leftrightarrow a_T$

Table 2.1 — Approximate lattice relations in the VO_2 crystallographic system in terms of the Rutile structure.

close to 90 degrees, the structure was mistakenly indexed early on as monoclinic (M_3) of point group C2/m. Nuclear magnetic resonance (NMR) experiments that all vanadium atoms are dimerized in the T structure, confirming in Pouget's notation [7], is the correct point group.

The lower symmetry M_1, M_2 and T phases can be viewed as distortions of the higher symmetry rutile structure. The rutile VO_2 structure is shown schematically in Fig. 2.2. Qualitatively, the vanadium positions in the rutile structure are in a body centered tetragonal arrangement. Each vanadium atom is surrounded by an oxygen octahedron. In contrast to the somewhat more

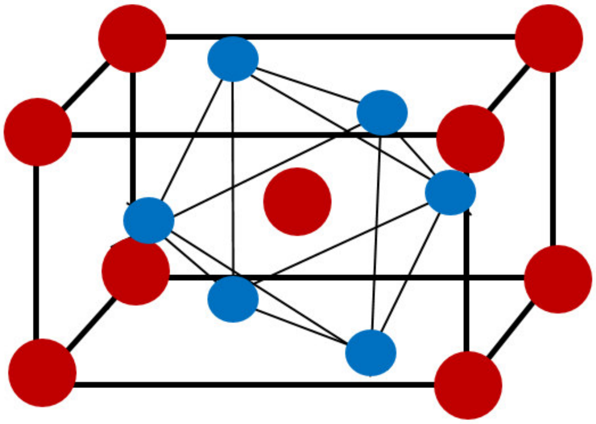

Figure 2.2 — Rutile lattice structure. Vanadium atoms shown in red, oxygen atoms in blue.

familiar perovskite structure, the oxygen atoms are not located on each face of the unit cell. Instead, two equatorial oxygens lie on each a_R-plane surface of the unit cell, while the apical oxygens are contained inside the cell. It's interesting to note that the octahedra which surround the central vanadium atom are rotated relative to the octahedra around the vanadium atoms at the corners of the unit cell by 90 degrees about c_R.

While it is not obvious from the symmetries of the unit cells, there is a deep connection between the four VO_2 lattice structures that is apparent when one views the displacements of the vanadium atoms from the rutile positions (See Fig 2.3). Vanadium atoms belong to one of two distinct vanadium "chains", which are oriented along the c_R axis. The chains in the rutile and M_1 phases are equivalent, except for the aforementioned relative rotation of the oxygen octahedra on each chain. In the M_1 phase, all vanadium atoms dimerize and tilt to an equivalent degree. In contrast, the vanadium chains in the M_2 and T phases are not equivalent. In the M_2 phase, one chain exhibits an equally spaced zigzag type distortion, while the vanadium atoms of the other chain dimerize, but do not tilt. The triclinic phase is intermediate between the two monoclinic phases, with the two chains having unequal degrees of dimerization and tilting. Interestingly, it can now be seen that the degree of dimerization and the tilt of the dimers are not

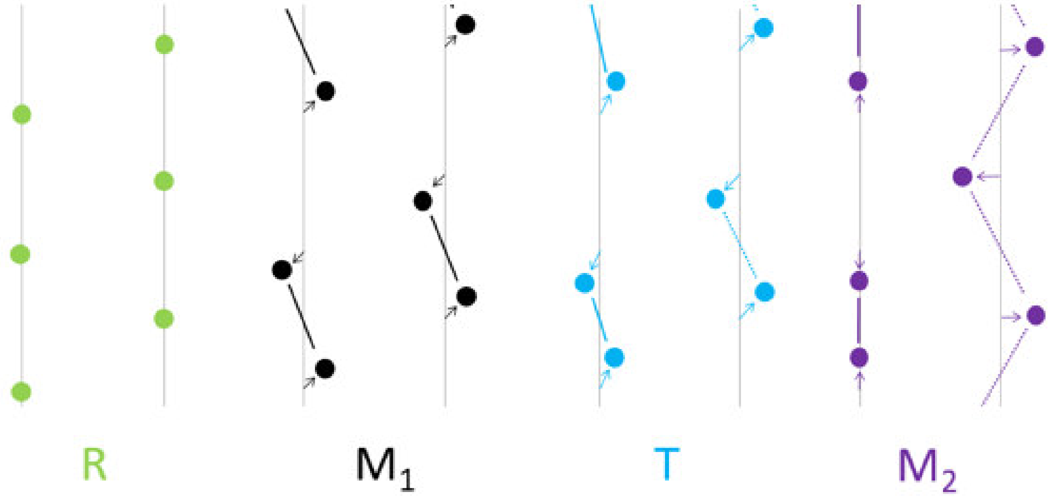

Figure 2.3 — Schematic positions of the vanadium atoms in the VO_2 lattice structures as viewed along $[100]_R$. Arrows indicate displacements of the vanadium atoms from their Rutile positions. Lines indicate shortest distance between vanadium atoms on the same chain.

independent effects. To illustrate, consider the M_2 structure. As the positively charged vanadium atoms repel one another, pairing on one chain encourages on the neighboring chain, and vice versa.

It should be emphasized that while this quasi-1D idea of vanadium chains is quite simple, it should not be dismissed as overly simplistic. In the tradition of William of Occam – only the necessary complexity of the lattice structures is maintained. As a result, the deep connection between the four lattice structures becomes clear. Thus, with the four lattice structures placed within a clear and comprehensive framework, we are now in a position to consider what effect these different lattice structures might have on the electronic structures.

2.3 DEBATE OVER THE CAUSE OF THE INSULATING BEHAVIOR

Ever since the discovery of the MIT in VO_2 by Morin in 1959, researchers have struggled to account for the unexpected insulating M_1 phase[3]. As alluded to previously, two distinct theoretical descriptions of the insulating behavior emerged early on, establishing the foundation on which the subsequent debate in the field has been built. The first work, published in 1971 by J.B. Goodenough[17], described the effect of the structural phase transition on the electronic band structure. In this "Peierls" picture - so named because the dimerization of the vanadium atoms is similar to an effect which always occurs in any half-filled one dimensional chain and leads to the opening of an energy gap – Goodenough argues that the structural transition alone induces the insulating M_1 phase band structure. In contrast, Zylbersztejn and Mott[18] argued that the while the non-interacting band theory considerations described by Goodenough certainly occur in the VO_2 system, alone they are insufficient to open the experimentally measured energy gap. Instead, they argue that electronic correlations are the dominant factor. Although the bulk of VO_2 research has focused on the M_1 phase, both Goodenough[19] and Mott[18,20] addressed the M_2 and triclinic phases in the context of their respective pictures.

As should be clear from the above discussion, the essence of the VO_2 problem is to understand the connection between the lattice structure and the electronic properties. The most conspicuous structural element of all of the VO_2 phases is the oxygen octahedra surrounding the vanadium atoms. As this is a common structural element in the transition metal oxides, its effect is discussed below. It is helpful to first define a coordinate system where the z axis is oriented along the direction between the apical oxygens. This causes the lobes of the $m_z=0$ d orbital to point towards the apical oxygens. The rotation of the coordinate system about the z axis should be chosen to point the lobes of one of the $m_z=2$ towards the equitorial oxygens, for example $\hat{x} \parallel c_R$ (See Fig. 2.4). Thus, all six

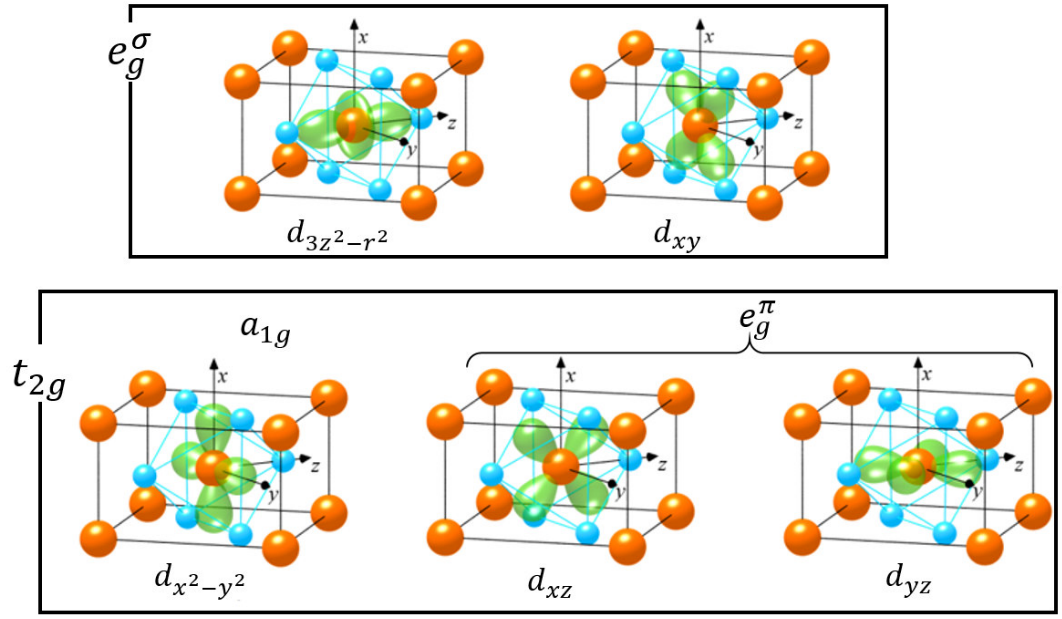

Figure 2.4 — Angular part of the vanadium (red) d orbitals within an oxygen (blue) octahedron. Modified from Ref. [78].

lobes of these two orbitals – $d^2_{z^2-r^2}$ and d_{xy} for our example – point toward the six oxygens of the octahedron. These orbitals, collectively henceforth referred to as e_g^σ, hybridize strongly with the O_{2p} orbitals, such that these states are raised in energy due to the negative charge ($\approx 2^-$) on the oxygen atoms. The remaining three $3d$ orbitals, collectively referred to as t_{2g}, are shifted to lower energies. The t_{2g} orbitals are further split as the orbital which lies along the rutile c_R axis (a_{1g}) is shifted to lower energy relative to the other two (e_g^π) orbitals by the by the tetragonal symmetry of the Rutile phase. This scenario is shown schematically in Figure 2.5. This is the situation in the rutile structure. As there are empty states above the Fermi energy for the one vanadium 3-d electron, the material is expected to be metallic in the band picture, in agreement with the existence of the rutile metal.

In the foundational work of the Peierls picture of VO_2, Goodenough qualitatively describes the effect of the structural transition to the M_1 phase within the context of band theory[17]. As we've discussed previously, Goodenough

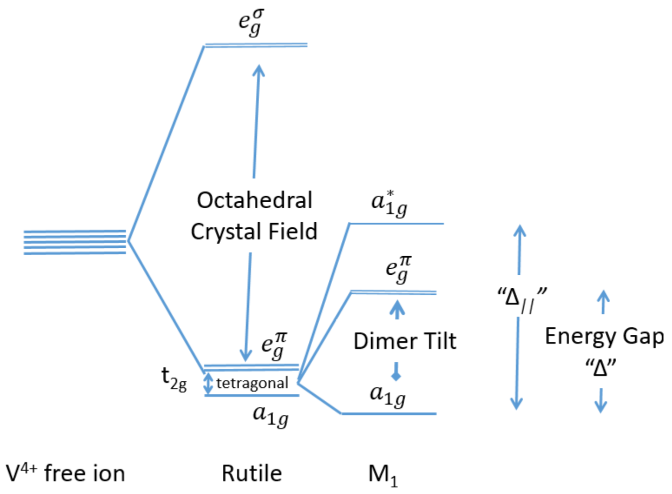

Figure 2.5 — Schematic of band splitting in VO_2. Δ and $\Delta_{||}$ are shorthand referring to the energy gap and the splitting between the bonding and anti-bonding a_{1g} bands, respectively.

identified the two salient features of the structural transition, the dimerization of the vanadium atoms along the c_R axis, and the anti-ferroelectric like tilt of those dimers. The effect of the dimerization, and equivalently the unit cell doubling along c_R, is to split the other m_z=2d orbital, $d_{x^2-y^2}$ in our coordinate system, into bonding and anti-bonding components. These orbitals are referred to as a_{1g} and a_{1g}^*, respectively. The tilting of the dimers results in a raising of the other two t_{2g} orbitals, now the e_g^π band, above the Fermi energy. Goodenough notes that, qualitatively, these two effects are sufficient to open the energy gap (See Fig. 2.5). Strictly speaking, a Peierls transition refers to the dimerization - and subsequent gap opening - of a half filled chain. However, in VO_2 the Peierls mechanism is generally used to refer to both effects. Note that the common thread of the two effects is that they are responses of the single particle (non-interacting) electronic band structure to the structural transition. Zylbersztejn and Mott agree that both effects described by Goodenough, the splitting of the a_{1g} band, and the upshift of the e_g^π band, are necessary to open the energy gap. It is worth emphasizing that this band scheme is supported by optical, x-ray absorption, and photoemission spectroscopic experiments[21–25]. However, the debate is whether or not the dramatic changes in the electronic structure across the MIT can be explained primarily by a structural transition. Zylbersztejn and Mott argued that no quantitative description is possible without taking into account the intra-atomic Coulomb repulsion, the Hubbard U parameter[18].

2.4 THE EXPERIMENTAL RECORD

Ultimately it falls to experiment to determine the physical reality of the system. While the literature still lacks a conclusive experimental result to settle the debate, there has been a great deal of experimental work done on the VO_2 system over the 67 years since the discovery of the MIT[3]. The experimental situation thus far, is as follows:

A. Thermodynamics

The first order transition between the M_1 and rutile phases has a latent heat of 1020 cal/mol, which corresponds to an entropy change (ΔS) of approximately $1.6k_B$ per formula unit[26]. Early on, it was estimated that the electronic entropy of the rutile metal accounts for approximately 1/3 of the entropy change[6,18]. In line with this early estimate, neutron and inelastic x-ray scattering reveals that 70 percent of the entropy change is due to the soft phonon modes of the rutile [27]. That the thermodynamics are partly lattice driven illuminates why the transition temperature is sensitive to oxygen isotope substitution[28].

Interestingly, in pure, unstrained VO_2 the four phases have been shown to be degenerate at T_c [8]. The latent heats between the various phases induced by chromium doping is shown in Table 2.2, reproduced from Ref. [7]. There is a negligible latent heat between the M_1 and T phase, resulting in a second order phase transition[7]. This is consistent with the suggestion that the T phase is transitional between M_1 and M_2; the T phase is really a continuum of VO_2 lattice structures with unequal vanadium pairing on all chains. In contrast, the T to M_2 phase transition is first order - except when induced with very large

Table 2.2. Latent heats per formula unit of various structural phase transitions in $V_{1-x}Cr_xO_2$[7].

x	Transition	Latent heat (meV/F.U.)
0	$M_1 \rightarrow R$	44.67
0.003	$M_1 \rightarrow T$	unmeasurable
	$T \rightarrow M_2$	7.11
	$M_2 \rightarrow R$	34.7
0.03	$T \rightarrow M_2$	1.17
	$M_2 \rightarrow R$	33.4

Cr concentrations ($\geq$3%) – with a latent heat of 7.11 meV/F.U.[7]. That there is an entropy difference between the M_2 and the T/M_1 insulating phases was shown to correspond to the magnetic entropy of the (undimerized) antiferromagnetic chains in the M_2 phase[7] (See Section 2.4D).

B. Lattice dynamics

It was identified early on that the R $\rightarrow$ M_2 structural transition is consistent with a soft acoustic mode at the R-point of the rutile phase[29]. This mode is doubly degenerate, and an equal superposition of both modes corresponds to the M_1 phase structure. The doubled unit cell of the M_1 phase, relative to the R phase, changes the symmetry of these modes to A_g (Raman active), and fold them to the zone center (Γ)[30]. The soft R-point acoustic modes were also seen by Gervais and Kress in shell model calculations [31]. There is extensive experimental data supporting the notion that quite generally, the phonon modes associated with the structural transition soften ($\nu_i \rightarrow 0$):

- X-ray diffuse scattering experiments have confirmed that there is indeed a soft mode at the rutile phase R-point[32]. This is further confirmed by Neutron diffraction and inelastic x-ray scattering.

- Raman spectroscopy reveals softening of the A_g modes associated with the structural transition from the lower symmetry structures[33,34].

Of course, that this would be the case was known form the outset; the structural transition must necessarily proceed through an instability in the lattice.

Interestingly, there is extensive experimental evidence that the rutile phase lattice dynamics are quite different from those of the insulating phases. For example:

- In their x-ray diffraction study, McWhan *et al.* observed large thermal displacements in the rutile phase [11].
- Neutron diffraction and inelastic x-ray scattering shows that the rutile acoustic R-point mode in energy space is unusually broad. Such broadening corresponds to an unusually short phonon lifetime[27].
- Rutile phase infrared [35,36] and Raman [37] phonon spectra show optical phonon modes much broader than their insulating phase counterparts.

These results indicate that the ions in the rutile phase interact through highly anharmonic potentials. Equivalently, their phonons have very short lifetimes compared to the insulating phases. The broad phonon features of the rutile phase are a signature of the high lattice entropy discussed previously.

As pointed out by Mott, the dramatic change in the phonon lifetimes between the different electronic states suggests strong electron-phonon coupling[18]. Mott contends that the factors that lead to high lattice entropy - soft modes and short lifetimes - ultimately result from the electrostatic screening provided by the conduction electrons in the rutile metal. Such screening results in anharmonic interactions between the ions, and accounts for both effects. This electrostatic screening is significantly reduced in the insulating phase, which explains why the phonon features are much less broad.

C. DC transport

Quite generally, transport and optical techniques indicate that the rutile conductivity is higher along c_R than a_R. While dc electrical transport measurements indicate that the conductivity can be an order of magnitude or more larger along c_R that a_R in the rutile metal[38,39], optical spectroscopy indicates that the conductivity ratio is of order unity [24,35,36]. It is thus reasonable to conclude that the fairly small anisotropy observed in the optical experiments is the intrinsic anisotropy, while the transport measurements reveal extrinsic effects, such as film microstructure, micro-cracks, or phase coexistence. In support of this argument, transport measurements on free-standing VO_2 nanorods, which are extremely clean samples, give a conductivity along c_R in the rutile phase of approximately 2000 $\Omega^{-1}cm^{-1}$, in good agreement with the infrared optics data[40]. The conductivity anisotropy, although small, may be taken as evidence that multiple bands (a_{1g} and a_{1g}^*) cross the Fermi energy, in agreement with the schematic band structures suggested by Goodenough and Mott[26].

Across the metal-insulator transition to the M_1 phase, the dc conductivity can change by as much as five orders of magnitude, depending on the sample. The magnitude of this change has been shown to be highly dependent on optimal stoichiometry[3,38,41]. The three insulating phases have very similar dc resistivities, with the M_1 and T phase resistivities being quite similar, and the M_2 phase resistivity being approximately a factor of two higher[14]. The notion that the three insulating phases are quite similar is highlighted by the fact that the activation energy of the conductivity, 0.4 eV in M_2 and T phase VO_2 induced by 0.4% Cr doping, is quite similar to the 0.45 eV activation energy for the M_1 phase of pure VO_2 [18,42].

D. Magnetism

The magnetic properties and electronic structure of VO_2 is best thought about about in the vanadium chains framework discussed previously. Pouget *et al.*, in in Ref. [7], recognized that both the band (Peierls) and correlated (Mott) pictures pictures of VO_2 are merely limiting cases of the Hubbard model on the chains. The vanadium chains in VO_2 are analogous to the more familiar problem of a chain of hydrogen atoms. On the dimerized chains, the two *d* electrons of each dimer form a bonded spin singlet. This is responsible for the very small paramagnetic susceptibility seen in the M_1 and T phase[7]. As expected, these ground state singlets result in a Van Vleck paramagnetism that is largely temperature independent. It's interesting to note that the intra-dimer exchange constant (J_{intra}) is quite large, a lower bound for the M_1 phase is estimated to be $J_{intra} \geq 1{,}000$ K[7]. In the M_2 phase, where half of the dimers are broken to form equally spaced chains, a negative Knight shift (K= - 0.13%) is observed via NMR on these chains, which is indicative of localized electrons. These localized moments have an antiferromagnetic coupling with an exchange constant 2J between 40-60 meV [18,43,44]. This corresponds to J≈230 K to 350 K. Thus, the fairly small region of the phase diagram near 340 K occupied by the M_2 phase is probably above the Néel temperature, and the local magnetic moments on the undimerized chains may not be ordered. Pouget *et al.* estimate the magnetic entropy of this situation to be 5.6 meV/F.U., which is quite comparable to the entire latent heat between the T/M_1 phases and the M_2 (7.11meV/F.U.) [7]. Upon the transition to the rutile phase, as all dimers are broken, the (still) paramagnetic susceptibility increases by almost a factor of 10[26]. Berglund and Guggenheim interpreted this as evidence of the rutile phase having two bands: a wide band which would account for the transport properties (e_g^π) and a narrow band with a very high effective mass (a_{1g}) which would make the major contribution to the magnetic susceptibility.

E. Electronic structure

Various experimental probes of the electronic structure have confirmed the band structure of both bulk phases of pure VO_2 (R and M_1) to be qualitatively

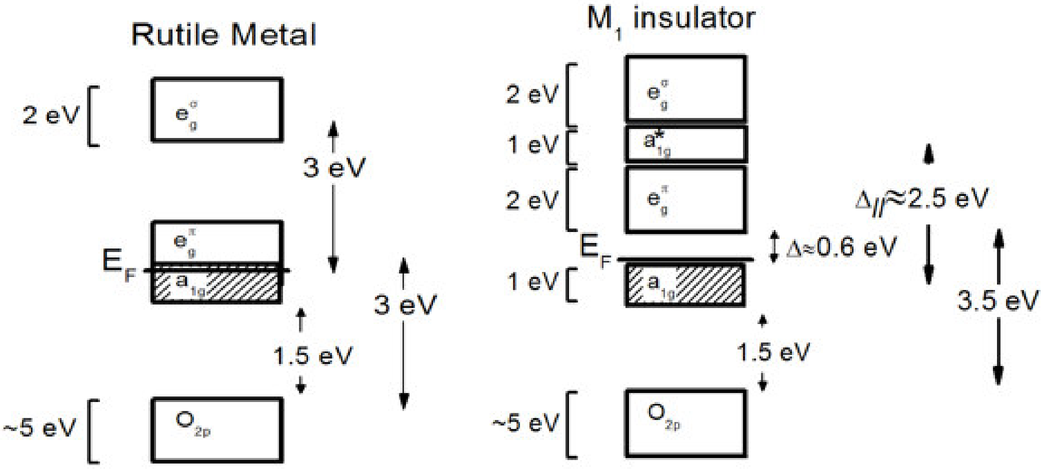

Figure 2.6 — Energy level diagram of the VO_2 bulk phases

similar to what was suggested by both Goodenough and Mott. While there is some quantitative disagreement – which is most likely attributable to differences in sample preparation and other systematic effects – infrared and optical photon spectroscopy, photoemission, and x-ray absorption spectroscopy all indicate the band structure shown in Fig. 2.6 for the rutile and M_1 phases. In the rutile phase, both the a_{1g} and e_g^π bands overlap the Fermi energy. The oxygen $2p$ orbitals lie ≈ 1.5 eV below the a_{1g} band. The crystal-field splitting between the t_{2g} orbitals (a_{1g} and e_g^π) and the e_g^σ orbitals is approximately 3 eV.

In the monoclinic M_1 phase, we see the two qualitative effects described by Goodenough to open the energy gap, Δ, which is a quite rigid spectral feature of 0.6 eV. The a_{1g} bands are split by approximately 2.5eV, forming a narrow (≈ 1eV) bonding (a_{1g}) and anti-bonding (a_{1g}^*) band. We refer to this splitting as $\Delta_{//}$, as it is the splitting of the d orbitals aligned parallel to the c_R axis. The upshift of the e_g^π band across the transition to the M_1 phase is approximately half an electron volt [21,23,24]. The O_{2p} bands lie around 1.5 eV below the bonding a_{1g} band.

2.5 THE CURRENT STATE OF VO_2 RESEARCH

A. Theoretical work

i. Density functional theory

Ultimately, the qualitative similarity in the electronic structure predicted the Peierls and Mott-Hubbard pictures presents a real challenge. In 1994, structure calculations were performed by Wentzcovich *et al.* using the local approximation (LDA) of density functional theory[45]. This mean-field calculation represents the single-particle band theory (Peierls) prediction. It does not include intra-atomic Coulomb correlations. The result was a semi-metallic M_1 phase, where the a_{1g} and e_g^π bands overlap by 0.04 eV[45]. Objectively, as the direct band calculation does not predict an insulator, let alone the experimental gap of 0.6 eV, this result is decidedly not in support of the Peierls picture. However, the authors attributed the lack of a band gap to a tendency of LDA to underestimate the band gap. Thus, the calculational result was ambiguous, but the authors' interpretation was in support of the Peierls mechanism, as the LDA calculation showed the same qualitative effects predicted by Goodenough. Of course, that these qualitative effects would be seen in a band theory calculation was never actually at issue, as both pictures agree that they will occur to some degree. The debate has always been over the relative contribution of band (Peierls) and electronic correlation (Mott-Hubbard) effects in the real system. It could be argued that LDA calculations suggest that the Peierls mechanism alone is not sufficient to open the experimental experimental energy gap.

ii. Hybrid functionals

Further calculations also faced quantitative discrepancies compared to experiment. In 2011, V. Eyert performed calculations on both the M_1 and M_2 phases using hybrid functionals[46]. Hybrid functionals mix non-correlated DFT with exact Hartree-Fock exchange. Eyerts results correctly predict insulating behavior, but dramatically overestimated the band gap, by a factor of 2. It can be shown that while Hybrid functionals are formulated somewhat differently, they do include intra-atomic correlations in a Mott-Hubbard-like manner [47]. However, the title of Eyert's work, "VO_2: A novel view from *band* theory", seemingly implies a non-correlated picture. While Eyert's results do capture the insulating behavior, there were other issues: his calculations found that the M_1 ground state is higher in energy than the rutile phase, and the predicted magnetic properties disagree with experiment.

iii. Dynamical mean field theory

Several Dynamical Mean Field Theory (DMFT) studies have been Early on, it was recognized that the cluster extension, which is used to consider the vanadium dimer as an "impurity", was necessary to form bonded singlets the dimers to yield the experimental magnetic properties[48]. DMFT studies have been performed by two different research groups. Biermann and coworkers describe the M_1 phase modeled by cluster DMFT as a "correlation-assisted Peierls insulator"[48–51]. To clarify this seemingly contradictory jargon, they argue that while the correlations are necessary to open the energy gap, the M_1 insulator is Peierls-like in the sense that the bands do not have very short lifetimes, a hallmark of Mott-Hubbard insulators. In contrast, Kotliar and coworkers emphasize the importance of electronic correlations[52–54]. In an striking inversion of phrase, they describe the M_1 phase as a "Peierls assisted orbital selective Mott transition"[53]. In their more recent work, which also includes the M_2 phase, they go further, to describe the rutile to M_1 phase transition as a "Mott transition in the presence of strong intersite exchange"[54], where the function of the strong intersite exchange is to encourage bonding on the vanadium dimers. Interestingly, the calculated electronic structures of the M_1 and M_2 phases are quite similar[54].

B. Experimental challenges

Researchers have struggled to decouple the effect of the lattice distortion from that of Coulomb correlations. Although the experimental and theoretical work has generally been of the highest quality, the interpretation of the results can be quite challenging. Often, the field in general has been somewhat overzealous in interpreting results, leading to contradictory and misleading conclusions. Ultimately, a definitive experimental work is necessary to distinguish between the two mechanisms, and permit a coherent re-interpretation of the existing literature.

To illustrate the difficulty, we return to the Hubbard model on the vanadium chains discussed previously. The ground state in both the Mott-Hubbard and Peierls limits is characterized by a bonded spin singlet on the vanadium dimers. There is no clear physical distinction between the two situations in the M_1 phase, where all of the vanadium atoms dimerize equivalently. Pouget *et al.* identified this difficulty early on [7]. Their insight led them to study the M_2 and T phases, in addition to the more well studied bulk phases, and permitted the most significant experimental work with regards to the VO_2 debate. Their NMR results revealed the presence of local magnetic moments of about one Bohr magneton on the equispaced chains in the M_2 phase. The presence of these local moments, which is confirmed by electron paramagnetic resonance [55], is a clear hallmark of a Mott-Hubbard insulator. They argued that the since the transport properties of the insulating phases are quite similar, and the transition between the M_1 and T phases is continuous, that all insulating phases lie near the Mott-Hubbard limit. However, they left the conclusive experiment to future work:

> "However, the resistivity is probably extrinsic in origin and not a reliable guide to the behavior of the intrinsic energy gap. In this regard it would be of interest to measure the optical gap in the M_2 phase and compare it to the value in the M_1 phase."

In Chapter 4, we present the first such measurement in confirmation of Pouget's argument. The conclusion is supported by hybrid functional (HSE) calculations with parameters more appropriate for 3-d oxides[56] than those used in previous hybrid functional calculations on VO_2[46]. The argument does not rest on any particular model, as it is also supported by the Hubbard model on the vanadium chains discussed in Pouget's work, as well as the most recent DMFT study discussed previously [54].

Strangely, Pouget's insight into the importance of studying the M_2 and T phases was largely ignored by subsequent experimental works, which focused primarily on the M_1 and rutile phases of bulk VO_2. It is instructive to review selected recent experimental studies from the literature. While these works often make very bold and sometimes contradictory claims, they are ultimately inconclusive.

Photoelectron and x-ray absorption spectroscopy

The primary observation of photoelectron spectroscopy is that the 3-dimensional character of the rutile metal is transformed to a quasi-one dimensional character in the M_1 phase[21,25]. This is essentially a confirmation of the qualitative electronic structure agreed upon by both Zylbersztejn and Mott, and Goodenough[17,18]. The authors of these works attribute the change from three dimensional to quasi one dimensional character as being driven by electronic correlations, but then point out that the now one dimensional vanadium chains contain half-filled orbitals, and are thus susceptible to a Peierls like transition. These experiments, being unable to decouple the magnitude of the two effects, resorted to describing the transition mechanism as "collaborative". While this interpretation is quite attractive, particularly given the difficulty of decoupling the two effects, there is no reason to assume that the Peierls and Mott-Hubbard mechanisms both make significant contributions to opening of the energy gap.

In 2016, an x-ray absorption spectroscopy study by Grey *et al.* argued that electronic correlations soften prior to the MIT and structural transition. This result would be strongly in support of the Peierls picture, if the insulating phase of VO_2, with the same band gap, can exist despite the absence of intra-atomic coulomb repulsion. They argue that a particular spectral feature is indicative of electronic correlations based on the theoretical work of Biermann *et al.* from 2005[48]. It follows from this assignment of the upper Hubbard band that the a_{1g} to a_{1g}^* splitting is reduced by electronic correlations is in conflict with the later works of Biermann *et al.*, as well as those of Kotliar *et al.*[49,53,54,57]. As their conclusion hinges on this somewhat suspect assignment, their results are ultimately ambiguous.

i. Neutron diffraction and inelastic x-ray scattering

Neutron diffraction and inelastic x-ray scattering have attributed the mechanism of the opening of the energy gap to the Peierls mechanism[27]. These experiments observe the soft phonon modes corresponding to the structural transition and the broad rutile phase phonons discussed previously. They find, as was deduced early-on[18,26], that the thermodynamics of the phase transition is dominated by the high lattice entropy of the Rutile phase. Thus, their experimental work further characterizes the lattice dynamics, and confirms the previously established facts regarding the lattice dynamics of VO_2.

Given the strong electron-phonon coupling in VO_2, the fact that the thermodynamics are dominated by the lattice is not conclusive experimental evidence in favor of the Peierls mechanism. This point was argued by Zylbersztejn and Mott[18]. Moreover, it can be argued that the change in transition temperature as a function of oxygen isotope (O^{18}) substitution suggests that the MIT is driven primarily by changes in the electronic structure[28]. It is worth noting that such an isotope effect is also observed in V_2O_3, which is unambiguously classified as a Mott-Hubbard insulator[28].

Their argument in favor of the Peierls mechanism depends on supporting molecular dynamics calculations of the phonons, which are quite successful in reproducing the measured lattice dynamics. Their argument ultimately fails due to a mischaracterization of the HSE06 model as uncorrelated, when this is not the case. To summarize: They find that the lattice instability occurs using both the HSE06 and PBE+U (U=3.4 eV) methods. They assert that the HSE06 calculations do not include electronic correlation effects, and thus argue that correlation effects are not necessary to induce the structural transition. Moreover, they note that HSE06 actually overestimates the energy gap at 1.1 eV, in comparison to the experimental value of ≈0.6 eV. However, it can be shown that HSE06 is in fact a Hubbard-like model [58]. Therefore, their claim that HSE06 does not include correlation effects is incorrect. Moreover, in conflict with their conclusion, their results with a truly uncorrelated model (PBE (U=0)) does not show a lattice instability corresponding to the structural transition and opens only a very ($<$0.1 eV) energy gap[27]. Thus, their results actually strongly support the that the energy gap and the structural transition occurs as a result of electronic correlations.

ii. Time-resolved experiments

To decouple the two mechanisms, ultrafast pump-probe measurements have attempted to leverage the separation in timescales between the lattice and the electronic degrees of freedom. One such work, performed early on by Cavalleri[30], used near near-infrared and optical pumps – above the band gap of VO_2 – to induce a metal-insulator transition. Using photons of the same energy to probe the phase transition, they observed that they could not drive the transition faster than approximately 100 fs. This timescale corresponds to ½ the oscillation period of the phonons involved in the structural transition. This led them to conclude that the structural transition is the essential component in the MIT, in favor of the Peierls mechanism.

However, in a more recent work using a similar pump ($\lambda \approx$800 nm), an ultrafast electron diffraction probe reveals that the transition proceeds through a metastable metallic state with the M_1 lattice structure[59]. This result was taken as strong evidence of the Mott-Hubbard nature of the insulating state, as the M_1 lattice structure was insufficient to open the energy gap. The picture from ultrafast experiments is thus unclear, in part due to the fact that the metastable and transient phases induced by ultrafast excitations inherently convolute the issue. It is not apparent how the properties of these transient phases relate to the equilibrium phases, and therefore it is unclear how much insight they provide regarding the equilibrium phases.

iii. Monoclinic metals

A number of studies have observed monoclinic phases with metallic electronic properties[59–61]. The existence of such a phase is a strong indication that the Peierls mechanism alone is not *sufficient* to open the energy gap. Nevertheless, as these phases are observed in extreme circumstances such as nano-scale sized domains[61], ultrafast optics experiments[59] or under high hydrostatic pressure[62,63], the full characterization of these phases is challenging. Certainly, the electronic properties of these phases seems to be quite different from the bulk rutile metal [62]. Moreover, it is unclear that the dimerization (unit cell doubling) is the only thing that is changed in these materials. It is quite possible that intra-atomic correlations (Hubbard U) are modified across the phase transition. Thus, it is at present not possible to rule out the Peierls mechanism from having a significant effect on the electronic structure.

C. State of the debate

The present state of the debate is as follows: While there is significant evidence that electronic correlations play some role - based both on the experimental work, in particular the observation of monoclinic metals, and the calculational result that LDA, a Peierls (band) like model, fails to open an energy gap – the contribution of the Peierls distortion remains unclear. Thus, the relative contributions of electronic correlations and lattice structure to the MIT need further investigation.

Chapter 3

Anisotropic infrared response of VO_2 microcrystals

3.1 INTRODUCTION

The anisotropy of the monoclinic M_1 and rutile lattice structures of VO_2, along with the inherent anisotropy of the electronic *p* and *d* orbitals, may be expected to lead to anisotropy in the electronic and phonon properties. The directional dependence of these properties could play a major role in the MIT. Evidence for the relevance of anisotropy is provided by photoemission and x-ray absorption experiments that have documented the changes in occupation of the a_{1g} and e_g^{π} orbitals across the phase transition[21]. Accurate measurements of the anisotropy of the lattice dynamics and the infrared electronic properties in the monoclinic M_1

and the rutile phases are therefore important in the investigation of the cause(s) of the MIT.

Previous infrared spectroscopy experiments on polycrystalline thin films or crystals have been limited in their ability to investigate the anisotropy of VO_2 due to the nature of their samples[23,24,35,64]. For example, as large VO_2 single crystals go through the structural transition, they exhibit twinning because the symmetry of the rutile (tetragonal) structure is broken in the monoclinic M_1 structure. The rutile c_R axis always becomes the monoclinic a_m axis, but only one of the rutile a_R axes can transform to the monoclinic b_{M1} axis leading to two possible orientations of the b_{M1} axis differing by a 90 degree rotation about the c_R axis[65]. Domains approximately 40 micrometers in size result, the difference between the two types of domains being the orientation of the b_{M1} axis[35]. A macroscopic infrared measurement averages over these domains[35]. Therefore, twinning is a problem for measuring the anisotropy of charge dynamics of VO_2. Moreover, multi-domain crystals also tend to crack or break as they go through the MIT[35]. As the cracks may introduce new reflection planes, extracting the optical properties from such a crystal is fraught with difficulties. Polycrystalline thin films typically have grains with different orientations. Therefore, in both types of samples, assignment of phonon symmetries and parameters is difficult. Thus either a single domain crystal or an epitaxial, untwinned film is required to make meaningful, specific measurements of the anisotropy of the electronic properties and phonon parameters.

Recently it has become possible to grow untwinned single domain VO_2 microcrystals on oxidized silicon substrates by the vapor transport method[40,65]. Single domain crystals are less likely to crack as they go through the MIT. At room temperature, the a_m axis of the monoclinic M_1 phase of the microcrystal is parallel to the plane of the substrate[66]. Previously, infrared spectroscopy has been performed on VO_2 microcrystals in the spectral range between 1000 cm^{-1} and 7000 cm^{-1}. However, these experiments did not consider the anisotropic nature of the VO_2 microcrystal and could not measure the infrared active phonons[67]. Broadband infrared microspectroscopy with polarized light allows us to measure a single domain sample to obtain the true anisotropy of the optical constants. In this work, we report the center frequencies, oscillator strengths, and broadenings of 14 of the 15 infrared (IR) active phonons in monoclinic M_1 VO_2 and all 4 infrared active phonons in rutile VO_2, and assign them their proper group theory labels. We compare our results to previous work done on twinned bulk crystals in Ref. [35] and to zone-center frequencies calculated with first principles theory. We also report the directional dependence of the low frequency optical conductivity of metallic rutile VO_2 between 200 and 6000 cm^{-1}.

The chapter is organized as follows: in the next section we present the salient aspects of the experimental methods and data analysis followed by an account of the theoretical methods. Next, we discuss the experimental and theoretical results for the monoclinic phase and then the rutile phase. We conclude by reviewing our main results. Finally, we present technical details about our experiment and data analysis for the experts in Appendix A.

3.2 METHODS

A. Experimental methods

The single domain microcrystals used in this experiment were grown by vapor transport on oxidized silicon substrate[40]. Most of these crystals grow in long, thin rods that are not particularly suitable for infrared microspectroscopy because their narrow dimension tends to be smaller than the diffraction-limit. However, there are a few large microcrystals with low aspect ratios among the ensemble, and we chose one of the largest crystals for our experiment (See Fig. 3.1a). The thickness of the VO_2 microcrystal was directly measured by an atomic force microscope. Layer thicknesses used in the

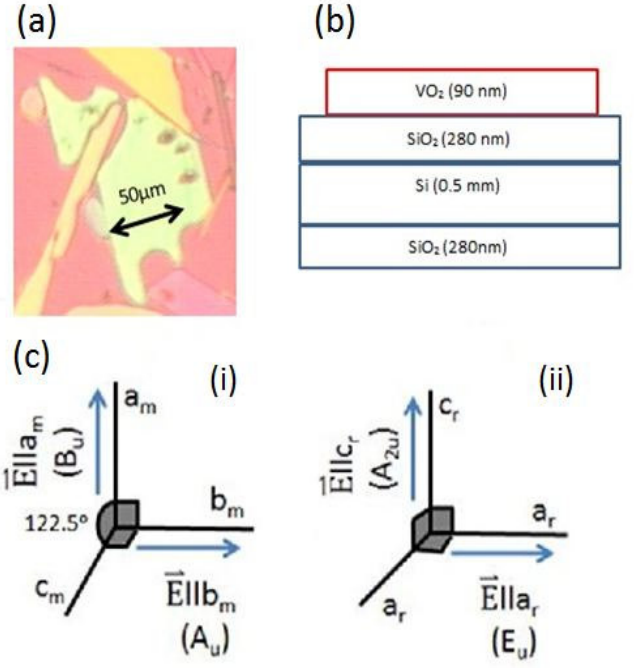

Figure 3.1 — (a) Optical image of the VO_2 microcrystal studied. The double-ended arrow indicates the size of the crystal. (b) Schematic cross sectional view of the microcrystal and oxidized silicon substrate. The thicknesses of the various layers are given in parentheses. (c) Diagram of the polarizations used with respect to the crystallographic axes in (i) the monoclinic M_1 phase and (ii) the rutile phase.

modeling are shown in Fig. 3.1b. As the substrate is transparent in the infrared spectral range, it is possible to make transmission measurements for obtaining the frequency-dependent complex dielectric function of VO_2 microcrystals.

Preliminary characterization of the VO_2 microcrystals with infrared microscopy at frequencies greater than 800 cm^{-1} was carried out at the Advanced Light Source at Lawrence Berkeley National Laboratory. To extend our spectral range into the phonon region, we later performed broadband infrared micro-spectroscopy between 200 cm^{-1} and 6000 cm^{-1} on the VO_2 microcrystal at the U12IR beam line at National Synchrotron Light Source. A Fourier Transform Infrared (FTIR) Spectrometer was used to measure the broadband infrared transmission of the VO_2 microcrystal and substrate normalized to the transmission of the substrate between 200 cm^{-1} and 6000 cm^{-1}. A 15X 0.58 NA Schwarzschild microscope objective focused the FTIR beam onto the microcrystal[68]. A wire-grid on 5 substrate polarizer was used to orient the electric field of the incident light perpendicular and parallel to the a_m axis of the M_1 phase (see Fig. 3.1c). The orientation of the a_m axis in the VO_2 microcrystal was determined by rotating the polarizer until the A_u phonon around 600cm^{-1} was absent in the spectrum[35]. Then, the polarizer was oriented perpendicular to the a_m axis. As the resulting spectrum for $\vec{E}\perp a_m$ contains none of the B_u phonons seen in the $\vec{E}//a_m$ spectrum, it can be concluded that the crystal is oriented such that both the a_m and b_m axes are in the plane of the crystal, i.e. $\vec{E}\perp a_m$ is in fact $\vec{E}//b_m$. In the rutile phase, the incident light was polarized parallel to the a_r and c_r axes (see Fig. 3.1c). Normalized, broadband transmission spectra were taken at 295 K for the monoclinic M_1 phase, and at 400 K for the rutile phase. The absolute transmission of the substrate was also measured at both these temperatures (See Appendix A).

Kramers-Kronig consistent oscillators were used to model the normalized transmission spectra and extract ε_1 and ε_2, the real and imaginary parts of the complex dielectric function. Phonon features in the normalized transmission spectra were modeled with Lorentz oscillators of the following form:

$$\varepsilon(\nu) = \sum_{i=1}^{n} \frac{s_i}{1 - \frac{\nu^2}{\nu_i^2} - \frac{i\gamma_i \nu}{\nu_i}} \qquad 3.1$$

Where ν_i is the center frequency (inverse wavelength) of the i^{th} phonon, s_i is the oscillator strength parameter, and γ_i is the broadening parameter. The electronic response of the rutile metal was modeled with Lorentz, Tauc-Lorentz and Drude functions.

B. Theoretical methods

First-principles density functional theory (DFT)[69] calculations were performed by the Krakauer group at William & Mary using the "Quantum Espresso"[70] computational package, with the DFT+U[71] extension, in order to describe strong V *d-d* orbital correlations. The PBE[72] version of the generalized gradient approximation (GGA) was used for all calculations and only non-magnetic ground states were considered throughout this work. The rotationally invariant[73] form of the GGA+U approach is used to apply the Hubbard U correction. For all systems, we investigated a range of U corrections ranging from 0 → 7 eV. A Hubbard U value of 5 eV was found to give good agreement for both structures, as discussed further below. Lattice parameters for rutile[11] and monoclinic M_1[15] structures were fixed at values obtained from x-ray diffraction measurements. All internal atomic coordinates were relaxed until the calculated forces were less than

1 mRy/Bohr (≈0.03 eV/Å). Ultrasoft pseudopotentials[74] were obtained from the Quantum Espresso website for vanadium and oxygen[75]. Tests showed that a wave function planewave cutoff of $E_{cut} = 50$ Ry and a charge density cutoff of 300 Ry was sufficient to yield converged total energies and forces. Brillouin zone integrations were performed using 6x6x8 and a 4x4x4 Monkhorst-Pack[76] k-point meshes for the rutile and monoclinic structures, respectively; a small Fermi-Dirac type temperature broadening of 0.05 eV was also used in the metallic rutile phase. Zone center phonons were calculated using the method of small displacements and analyzed using the "Phonopy"[77] program, and Born effective charge tensors Z^* and ε_∞ were used to include non-analytic contributions to the dynamical matrix.

3.3 RESULTS AND DISCUSSION

A. Monoclinic M_1 phase

There are 12 atoms in the unit cell of monoclinic M_1 VO_2 of space group $P2_1/c$[78]. Group theory then demands that there will be 36 phonon modes, of which 3 are acoustic, 18 are Raman active, and 15 are IR active. The longitudinal or transverse character of a particular IR active mode depends

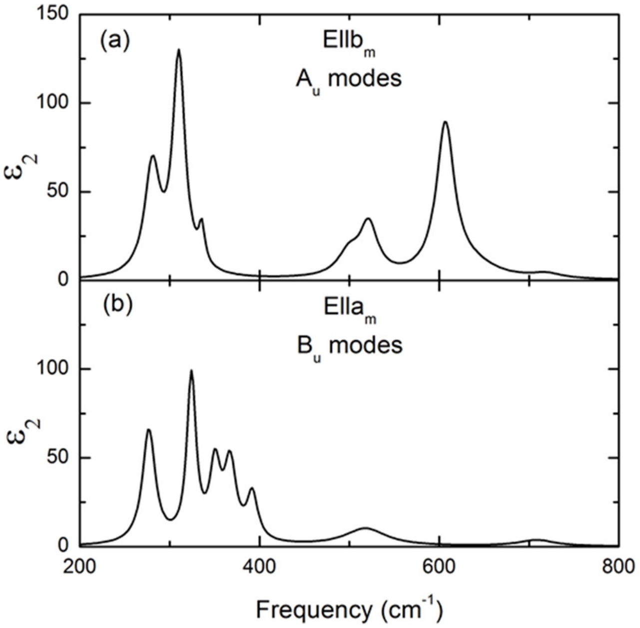

Figure 3.2 — The experimentally derived imaginary part of the complex dielectric function for monoclinic (M_1) VO_2 at T=295K for (a) $\vec{E}//b_m$ (A_u) and (b) $\vec{E}//a_m$ (B_u) in the phonon spectral region.

upon the direction of the phonon wave-vector *q*. When *q* is along the b_m axis, the 8 A_u IR modes have purely longitudinal character, while the 7 B_u IR modes have purely transverse character[79]. That is to say that the net dipole moments are along b_m for the A_u modes and perpendicular to b_m for the B_u modes. Along other wave vectors the phonons will have mixed transverse/longitudinal character due to the low symmetry of the M_1 phase. In the present experiment, the wave vector is perpendicular to the a_m-b_m plane so all 15 IR modes are expected to be seen: 8 A_u modes when the light is polarized along b_m and the 7 B_u modes when the light is polarized along a_m (perpendicular to b_m).

Experimentally, we see 7 distinct phonon features when the electric field $(\vec{E})$ of the incident light is parallel to a_m (B_u), and 7 distinct features when $\vec{E}$ is parallel to b_m (A_u) (See Fig. 3.2). The eighth A_u feature, which has been seen by Barker *et*

Table 3.1 — Lorentz oscillator fit parameters for monoclinic (M_1) VO_2 zone-center infrared active phonons

	A_u modes			B_u modes		
Mode no.	ν_i (cm^{-1})	s_i	γ_i	ν_i	s_i	γ_i
(1)	(189)	(0.54)	(0.012)	277	4.01	0.062
2	281	4.53	0.074	324	3.49	0.038
3	310	6.69	0.055	351	1.67	0.041
4	336	0.49	0.023	367	1.88	0.044
5	500	0.77	0.060	392	0.99	0.038
6	521	1.34	0.047	519	1.08	0.110
7	607	3.42	0.040	709	0.25	0.071
	637	0.67	0.100	-	-	-
8	720	0.15	0.056	-	-	-

Notes: A_u mode 1 is from Ref. [35] as it falls just outside our spectral range. A_u mode 7 is asymmetric and requires two oscillators for a proper fit.

al.[35] at 189 cm^{-1} in a bulk, twinned crystal, is outside of our spectral range. 8 A_u modes are thus accounted for. Table 3.1 tabulates the measured phonon parameters. The A_u peak near $\approx$ 600 cm^{-1} in Fig. 3.2 is asymmetric, which required two Lorentz oscillators, ω = 607 and 637 cm^{-1}, to fit, as shown in Table 3.1. We speculate that the apparent asymmetry observed near $\approx$ 600 cm^{-1} could be due to two-phonon processes arising from phonons near $\approx$ 300 cm^{-1}.

In general, our A_u center frequencies are in good agreement with Ref. [35] (See Fig. 3.3). Whereas Ref. [35] only identifies one mode at 505 cm^{-1}, our increased spectral resolution of 2 cm^{-1}, as opposed to the $\approx$7.5 cm^{-1} resolution of Ref. [35], allows us to resolve two distinct features at 500 cm^{-1} and 521 cm^{-1}, so that we see 7 IR active A_u modes within our measured spectral range. The

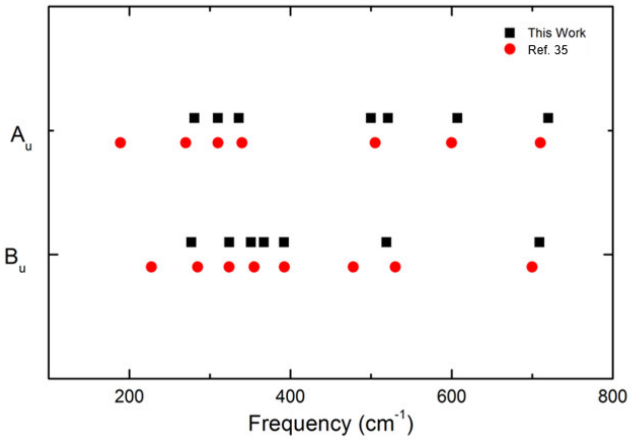

Figure 3.3 — Comparison of VO_2 monoclinic (M_1) center frequencies of A_u and B_u phonon modes from our experiment (black squares) and Ref. [35] (red circles).

broadenings of the A_u modes are within 10% of those measured by Ref. [35] for comparable modes. It should be noted that the A_u parameters in Ref. [35], measured as $E\perp a_{M1}$, were extracted from a spectrum with all 15 IR active phonons due to the twinning of the bulk crystal. Our B_u ($\vec{E}//a_{M1}$) mode center frequencies largely agree with Ref. [35]. However, we resolve two distinct modes at 351 cm^{-1} and 367 cm^{-1} whereas Ref. [35] reports a single mode at 355 cm^{-1}. With the inclusion of this mode, all 7 B_u modes are accounted for in our data. Ref. [35] also reports very weak modes at 227.5 cm^{-1} and 478 cm^{-1}, which do not appear in our data. For comparable modes, the broadenings for the B_u modes agree reasonably well with those of Ref. [35], with the exception of B_u mode 6, which is nearly twice as broad in the present work. It should be noted that this discrepancy is due in part to the “extra” mode used in Ref. [35] at 478 cm^{-1}. Moreover, the larger broadening of B_u mode 6 could be due to contribution from two phonon processes associated with B_u mode 1. Even though the a_{M1} axis is in the same direction for all the domains in Ref. [35]’s twinned crystal, the phonon parameters, particularly the oscillator strengths, will depend on the orientation of the wave vector of the incident light relative to the b_{M1} and c_{M1} axes. Thus, the oscillator strengths between our measurements on an untwinned crystal and those of Ref. [35] cannot be directly compared.

The phonon center frequencies at the gamma point have been calculated using GGA+U calculations. A Hubbard U = 5 eV yields good agreement with our experimental frequencies as seen in Table 3.2. Furthermore, this value yields a band gap of ≈ 1.0 eV which is in line with the experimentally determined band gap of ≈ 0.6 eV[21,23,64,80,81]. In general, there will be a frequency shift in the IR modes due to LO/TO-type splitting. These require knowledge of the high-frequency (above the phonon region) dielectric constant ε_∞ as well as the Born effective charge tensors Z*. Due to technical complications in calculating ε_∞ and Z* with GGA+U, we used the experimentally determined value $\varepsilon_\infty \approx 12$ from the present work; two sets of Z* tensors were used, the first from monoclinic ZrO_2 from Ref. [79] and, for comparison, the second using nominal diagonal values $Z_{\alpha\beta}^*(V)=+5e\delta_{\alpha\beta}$ and $Z_{\alpha\beta}^*(O)=-2.5e\delta_{\alpha\beta}$ [$Z_{\alpha\beta}^*(O)$ were simply fixed using the acoustic sum rule]. For the sample geometry, photon wave vectors are perpendicular to the a_m-b_m plane (the Γ to Y direction in the Brillouin zone), so only the B_u frequencies depend on ε_∞ and Z*[79].

Table 3.2 — Comparison of experimental and theoretical phonon frequencies for monoclinic (M_1) VO_2. The Mean Absolute Difference (MAD) between the theory and experiment is given for both phonon symmetries. For the B_u theory values the non-analytic correction includes ZrO_2 Born effective charges, whereas the frequencies in parentheses used nominal charges for V and O.

Mode no.	A_u mode center frequencies (cm^{-1})			B_u mode center frequencies (cm^{-1})		
	Experiment	Theory	Difference	Experiment	Theory	Difference
1	(189)	149	40	277	218 (227)	59 (50)
2	281	246	35	324	292 (292)	32 (32)
3	310	275	35	351	370 (370)	-19 (-19)
4	336	355	-19	367	403 (402)	-36 (-35)
5	500	417	83	392	466 (434)	-74 (-42)
6	521	466	55	519	544 (551)	-25 (-32)
7	607	512	95	709	738 (754)	-29 (-45)
8	720	720	0	-	-	-
			MAD			MAD
			45cm^{-1}			39 (36) cm^{-1}

Notes: A_u mode 1 is from Ref. [35] To compare with theory, 607cm^{-1} is used as the center frequency for A_u mode 7, as it is the center frequency of the stronger of the two oscillators used to model A_u mode 7 (See Table 1). B_u theoretical values are for Z^* taken from ZrO_2 in Ref. [79]. while values in parenthesis are for nominal Z^* values (see text).

As seen in Table 3.2, the agreement between experiment and theory is slightly slightly better for the B_u modes than for the A_u modes. The computed mean absolute deviation (MAD) for the A_u modes is 45 cm^{-1} while for the B_u modes it is 39 cm^{-1} or 35 cm^{-1} depending on the choice of Born tensors: values in parenthesis are for the nominal Z* discussed above. The agreement between our measured and computed frequencies (and the band gap) can be improved by decreasing the Hubbard U correction to 3 - 4 eV. However, this greatly increases the discrepancy for the rutile phase.

B. Rutile phase

The rutile structure is a simple tetragonal unit cell containing 6 atoms with space group $P4_2/mnm$[11,16]. Group theory predicts that there will be 18 rutile VO_2 phonons: 3 acoustic, 3 silent, 5 Raman active and 7 infrared active modes. Of the 7 infrared active phonons, 3 are doubly degenerate. Thus, we expect to see 1 A_{2u} mode when $\vec{E}//c_R$, and 3 E_u modes when $\vec{E}//a_R$. Experimentally, all four rutile infrared active phonons of VO_2 are seen for the first time. The measured phonon parameters and the low frequency optical conductivity are shown in Table 3.3 and Fig. 3.4 respectively. The rutile VO_2 phonons are roughly three times as broad as those of the monoclinic *M1* phase and insulating rutile TiO_2[82]. This broadening implies a decrease in phonon lifetime possibly due to electron-phonon coupling.

Phase coexistence in the form of a stripe pattern with alternating insulating and metallic regions in the microcrystals was observed through an optical microscope in the MIT regime. Similar stripe patterns have previously been observed in VO_2 nano-rods. These stripes have been shown to be phase domains

Table 3.3 — Lorentz oscillator fit parameters for rutile VO_2 zone- center infrared active phonons

	A_{2u} mode			E_u modes		
Mode no.	ν_i (cm^{-1})	s_i	γ_i	ν_i	s_i	γ_i
1	284	8.33	0.141	277	4.12	0.148
2	-	-	-	460	4.65	0.152
3	-	-	-	588	1.88	0.103

that form due to stress in the microcrystals caused by mismatch of thermal expansion between the oxidized silicon substrate and the VO_2 microcrystal[40,83]. As the microcrystals are grown at 1273 K, the mismatch between the coefficients of thermal expansion results in a $\approx 0.7\%$ in-plane isotropic tensile strain on the rutile structure near the phase transition temperature. The M_1 structure then expands by $\approx 1.1\%$ along the a_{M1} axis during the phase transition from rutile to monoclinic, whereas there is little change along the b_{M1} axis. Thus, the monoclinic phase is under a $\approx 0.4\%$ compressive strain along the a_{M1} axis, and $\approx 0.7\%$ tensile strain along the b_{M1} axis[40,83,84]. This leads to a monoclinic M_1 unit cell volume that is only slightly larger than that of bulk VO_2. In this way, it is possible that the effects of strain on the monoclinic M_1 phase are minimized, as our center frequencies are in good agreement with those obtained by Ref. [35] on bulk VO_2. Strain effects could play a larger role in the rutile phase properties.

The overall shape of the electronic conductivity between 2000 cm^{-1} and 6000 cm^{-1} for the rutile metal (Fig. 3.4) is consistent with previous reports[23,24,64]. The overall higher conductivity along the rutile c_r axis compared to the a_r axis is consistent with Ref. [24]. Optical conductivity below 2000 cm^{-1} along the a_r and c_r axes of the rutile phase has not been previously reported in the literature. Our data, which extends down to 200 cm^{-1}, suggests that the higher conductivity along the c_R axis compared to the a_r axis persists down to these frequencies. This is consistent with dc resistivity measurements made on single crystal VO_2[85]. However, the degree of anisotropy was much greater than that seen in our experiment, as the dc conductivity parallel and perpendicular to c_r was reported to be 2500 $\Omega^{-1}cm^{-1}$ and 333 $\Omega^{-1}cm^{-1}$ respectively[85]. An even greater degree of anisotropy is seen in highly strained VO_2 thin films on TiO_2 substrates, where the dc conductivity is measured to be 41.5 times greater along c_R than along a_R. These films are under a 1.92% tensile strain along c_R and a 0.93% compressive strain along a_R[48]. Thus, the anisotropy of the conductivity at low frequencies is very sensitive to strain. Below 1000 cm^{-1}, there

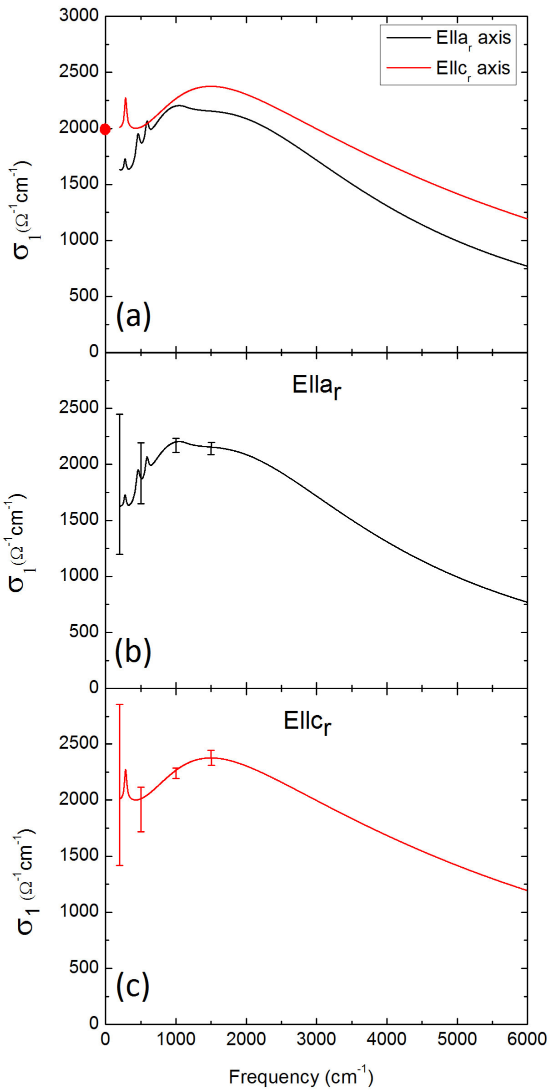

Figure 3.4 — (a) The a_R and c_R axis infrared conductivity ((σ_1) of rutile VO_2 at T=400K. The plots are consistent with the c_R axis *dc* conductivity constraint explained in Appendix 1. The known dc conductivity along c_R is shown by the red circle in (a)[40]. Lifting this constraint produces the error bars shown in Fig. 4 (b) and (c). These error bars arise from systematic uncertainties explained in Appendix A; the systematic uncertainties affect the conductivity (σ_1) of both axes in a similar manner.

is uncertainty in our conductivity data due to the incident spot being larger than the sample. The uncertainty, discussed in greater detail in the Appendix A, is large enough to preclude definitive statements about the frequency dependence of the electronic response at low frequencies. The possibility of localization of the conduction electrons, as evidenced by a peak in the conductivity (σ_1), around 1500 cm^{-1} in both polarizations is within the experimental uncertainty. A similar peak in σ_1 has been seen previously in nano-scale metallic "puddles" of VO_2 near the phase transition[86,87]. However, such a feature has not been seen in previous macroscopic experiments on polycrystalline thin films of VO_2 [23,64].

The agreement between experiment and theory for the phonon frequencies of the rutile structure is on par with the M_1 results (See Table 3.4). The MAD for the rutile modes is 41 cm^{-1}. Interestingly, the 3 E_u modes are still in good agreement for U = 3 eV (their errors are 17, 59, and 61 cm^{-1}), however, the A_{2u} mode is unstable (large negative ν^2) until U is increased to about 5 eV. In rutile TiO_2, this mode is associated with an incipient ferroelectric phase; under negative pressure, calculations show that it softens, resulting in a ferroelectric phase transitions[88]. For values of U smaller than about 5 eV in rutile VO_2, the same ferroelectric-like instability incorrectly appears at the experimental volume. Note

Table 3.4 — Comparison of experimental and theoretical phonon frequencies for rutile VO_2. The mean absolute difference (MAD) between theory and experiment is given for all rutile phonons.

	A_{2u} mode center frequency (cm^{-1})			E_u mode center frequencies (cm^{-1})		
Mode no.	Experiment	Theory	Difference	Experiment	Theory	Difference
1	284	269	15	277	215	62
2	-	-	-	460	398	62
3	-	-	-	588	563	25
			MAD $41cm^{-1}$			

that in VO_2 it is not a true ferroelectric state, since the system remains metallic when the crystal is allowed to distort according to this mode.

As mentioned, microcrystals in the rutile phase are under ≈ 0.7 % tensile strain along the a_R axis. To examine strain effects, we recomputed the phonon frequencies in the presence of -1% strain along the c_R axis, relaxing the in-plane axes. Differences between calculated and measured phonon frequencies changed by less than ≈ 9 cm^{-1}, except for the second highest E_u mode which increased by 22 cm^{-1}. Strain effects of this magnitude are thus not likely to be responsible for the differences between theory and experiment.

3.4 CONCLUSIONS

Polarized infrared micro-spectroscopy of untwinned single domain VO_2 crystals was performed. Single domain samples allow for the measurement of the true anisotropy of the phonons and the electronic response. The four zone-center infrared active phonons of metallic rutile VO_2 have been measured and identified for the first time. The electronic part of the infrared conductivity of metallic rutile VO_2 is weakly anisotropic and is measured to be higher along the c_r the c_r axis as compared to the a_r axis. The oscillator parameters of 14 of the 15 15 zone center infrared active phonon modes of the monoclinic M_1 phase of untwinned VO_2 have been measured for the first time. In addition, we have resolved an A_u mode near 500 cm^{-1} and observe a distinct B_u mode at 367 cm^{-1} not seen in previous measurements reported in Ref. [35]. From our measurements together with the lowest frequency A_u mode seen in Ref. [35], all 15 monoclinic M_1 infrared active phonons are now accounted for. Using first-principles GGA+U calculations we have computed the zone-center phonon frequencies for monoclinic and rutile VO_2. Our calculated results agree well with our measured frequencies.

Chapter 4

Insulating phases of VO_2 are Mott-Hubbard type

4.1 INTRODUCTION

There have been many experimental and theoretical studies of the thermally driven metal-insulator transition (MIT) between the insulating monoclinic (M_1) and the metallic rutile (R) phases of vanadium dioxide (VO_2). Some fraction of these studies attribute the insulating M_1 state to the vanadium-vanadium Peierls type pairing (see Fig. 4.1) that leads to unit cell doubling. Others argue that the insulating behavior in the M_1 phase is primarily a result of Mott-Hubbard correlations. These studies are reviewed in Refs.[89–91], A significant proportion of the literature on the nature of insulating VO_2, particularly in recent years[21,25,27,51,53,59,92–99], has struggled to decouple the contributions of the Mott-Hubbard and Peierls mechanisms because of an emphasis on the M_1 phase. Interestingly, it has long been recognized that measuring the electronic properties of two additional insulating VO_2 phases, the monoclinic M_2 and triclinic T, could potentially settle the debate about the origin of the energy gap, but the measurements have been difficult to achieve.

One of our purposes in this chapter is to refocus attention to the importance of measuring the electronic properties of the monoclinic M_2 and triclinic (T) phases to decouple the effects of the Peierls and Mott-Hubbard mechanisms. This can be seen from the argument put forward by Pouget *et al.* [7], which can be summarized as follows: One starts from a model of an isolated vanadium dimer in VO_2, with one electron per site, analogous to the familiar case of the hydrogen molecule. Both the Peierls and Mott-Hubbard pictures correspond to limiting cases of the Hubbard model for a chain of such dimers, depending on whether the intra-dimer hopping parameter (t) or the intra-atomic Coulomb repulsion (U), respectively, is the dominant energy scale in the system. Interestingly, in both cases, the qualitative description of the electronic structure is the same: an insulator with a bonded spin singlet on the dimer, where the band gap results from splitting of the bonding and anti-bonding a_{1g} bands (the lower and upper Hubbard bands in the Mott picture). As pointed out by the authors of Ref. [7], the only clear distinction between the two cases is how the energy gap responds to changes in the hopping parameter resulting from changes in lattice structure. For the chain of dimers, the bands broaden relative to the isolated dimer, decreasing the gap based on the inter-hopping (t'). In the Peierls limit (U $<<$ t, t'), insulating behavior vanishes as approaches t, the case of undimerized chains. In contrast, the gap is primarily set by U in the Mott-Hubbard limit (U $>>$ t, t'), and thus insensitive to changes in the degree of dimerization. In the M_1 phase, where all of the chains are dimerized and equivalent, it is impossible to decouple the effect of dimerization from intra-atomic Coulomb correlations. This is not the case for the M_2 and T phases.

In this chapter, we present broadband optical spectroscopy data on the M_2 and T phases of VO_2. We have performed infrared micro-spectroscopy and spectroscopic micro-ellipsometry on internally strained VO_2 crystals that undergo a first order phase transition with increasing temperature from the T phase to the M_2 phase. The energy gap and electronic structure are essentially unchanged across this structural phase transition. Moreover, the optical energy gap of 0.6 ($\pm$ 0.1) eV in the M_2 and T phases is nearly the same as that measured by numerous previous measurements on the M_1 phase [21,23,64,86,100,101]; the gap is insensitive to the different vanadium pairing arrangements in the M_1, M_2 and T phases. It follows that the gap in the insulating phases of VO_2 has a common physical origin in intra-atomic Coulomb correlations. This conclusion is supported by calculations also presented in this work. These calculations go beyond the Hubbard model for a chain of vanadium dimers and take into account the multi-band nature of the electronic structure.

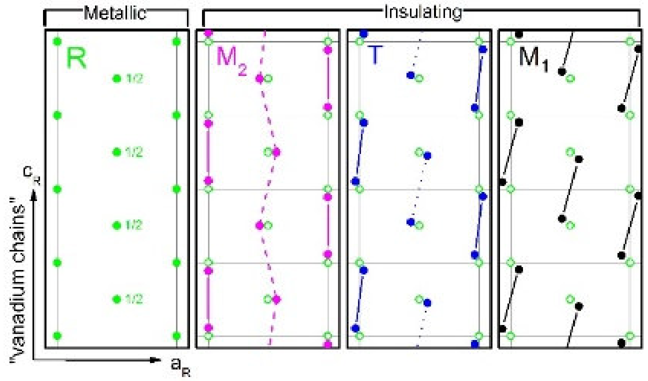

Figure 4.1 — A plan view of vanadium ion positions for the metallic rutile and insulating M_2, T, and M_1 phases of VO_2. In all phases, the vanadium ions at the center of each rutile unit cell (shown by the gridlines) are offset from the others by æ unit cell (denoted by "1/2" in the rutile panel). The vanadium ions in the insulating phases undergo small displacements from the rutile positions (open green circles in the panels of the insulating phases). The rutile lattice vectors c_R and a_R are shown in the lower left corner of the diagram. Vanadium chains in the insulating phases are oriented along the c_R direction.

In the M_1 phase, all of the vanadium ions dimerize and tilt in equivalent chains along the rutile c_R axis (see Fig. 4.1). In contrast, the M_2 phase contains two distinct types of vanadium chains: one type consists of vanadium ions that pair but do not tilt, while the other consists of vanadium ions that tilt but do not pair. The vanadium ions in the latter chain are equidistant, each carrying a localized electron with a spin-1/2 magnetic moment and antiferromagnetic exchange coupling between nearest neighbors[7]. The T phase has two types of inequivalent vanadium chains (or sub-lattices) in which the vanadium ions are paired and tilted to different degrees (see Fig. 4.1.) [7,10]. The T phase can be thought of as an intermediate phase between the M_2 and M_1 phases, where the chains become equivalent in M_1. While the M_1 insulating phase is generally found in bulk the M_2 and T phases can be accessed via chemical doping or strain [7,9,14,102–106].

Nuclear Magnetic Resonance (NMR) and Electron Paramagnetic Resonance (EPR) have determined the presence of localized *d*-electrons with about one Bohr magneton magnetic moment on the unpaired vanadium chains of the M_2 phase[7,9,104]. While this localization is a clear hallmark of a Mott-Hubbard insulator, the situation in the dimerized chains is less clear. The NMR and EPR measurements reveal that the electrons on the dimerized chains are covalently bonded. Therefore, as alluded to above, it is ambiguous whether the dimerized chains should be thought of as Peierls insulators, or Mott-Hubbard insulators with the valence electrons forming covalently bonded singlets which are localized on the dimers. It has been argued that the M_1 and T insulating phases of VO_2, which differ only slightly in free energy from the M_2 phase, cannot have a grossly different energy gap and should thus also be classified as Mott-Hubbard insulators[7,107]. Although strong, this argument needs experimental verification – presented here– via direct measurement of the M_2

and T phase energy gaps, which can then be compared to each other and to the literature values of the M_1 phase energy gap.

4.2 EXPERIMENTAL METHODS

Pure VO_2 crystals were grown with a self-flux method and thoroughly characterized with transport and X-ray diffraction measurements[105]. X-ray diffraction together with resistance measurements have determined that upon heating, the crystal first goes through an insulator-to-insulator transition and a structural transition between the T phase and the M_2 phase [105]. The temperature dependent resistance data displayed in the inset of Fig. 4.2 clearly shows two discontinuities along with hysteresis, indicative of first order phase transitions. The resistance increases by about a factor of two upon the structural transition from the T phase to the M_2 phase,

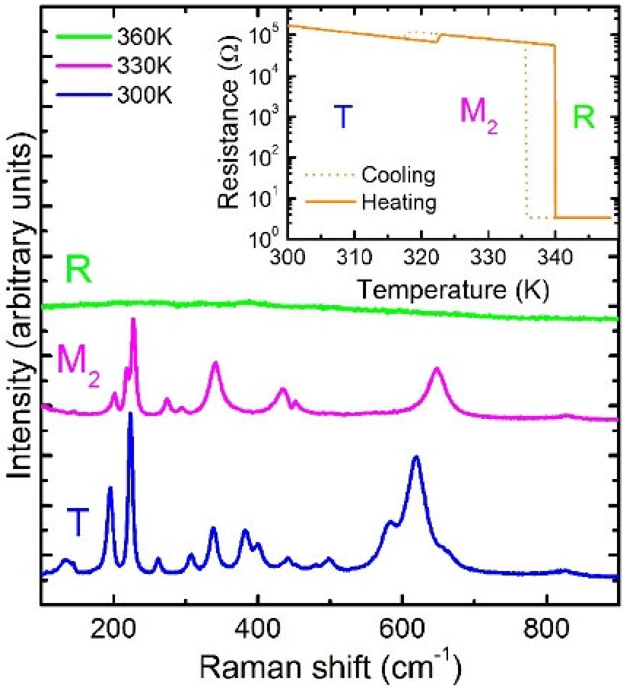

Figure 4.2 — Raman spectra of a typical VO_2 crystal studied in our work. Spectra are shown for the T, M_2 and R phases. The dc resistance of the crystal is plotted as a function of temperature in the inset.

consistent with previous measurements in the literature[14]. Upon further heating, the crystal undergoes an insulator to metal transition and a structural change from the M_2 phase to the metallic R phase. Unpolarized Raman micro-spectroscopy on the T, M_2, and R phases, presented in Fig. 4.2, verifies the structural assignment from x-ray diffraction when compared to unpolarized Raman spectra in the literature[103,108]. Our crystals are in the shape of rods with approximately square cross-sections between 50 μm and 100 μm wide, and with lengths between 1 mm and 3 mm. The rutile c_R axis, which points along the vanadium chains in the insulating phases, is oriented along the long axis of the crystals. Through an optical microscope, we observe that the crystal increases in length by $\approx 0.6\%$ upon transitioning from the T phase to the M_2 phase, and decreases in length by ≈ 1.7 % across the MIT from M_2 to R. These changes in length are consistent with the changes in the lattice parameters along the vanadium chains measured with x-ray diffraction in previous works [13,109]. The surface of the crystal is identified by X-ray diffraction as the (110) plane in the rutile basis which transforms to two coexisting, twinned surfaces (201) and $(\bar{2}01)$ in the monoclinic M_2 phase[109]. Further twinning occurs as the 2-fold rotational symmetry of the M_2 phase is lost upon transitioning to the T phase. The result is that for each M_2 twin, there are two possible T phase twins, which differ from each other by a 180° rotation along the c_R (b_{M2}) direction[12].

The small size of the VO_2 crystals calls for specialized infrared and optical micro-spectroscopy techniques to obtain reliable data with good signal-to-noise ratio. Infrared reflectance micro-spectroscopy between 150 and 6000 cm^{-1} was performed at beamline U12IR at the National Synchrotron Light Source, Brookhaven National Laboratory[68]. Infrared polarizers were employed to obtain reflectance spectra parallel and perpendicular to the long axis of the crystals, i.e. the rutile c_R direction. Absolute values of the infrared reflectance spectra in the T and M_2 insulating phases were obtained by normalizing them to the nearly featureless spectra of the rutile metal.

Generalized spectroscopic micro-ellipsometry between 0.6 and 5.5 eV (≈4800 and ~44000 cm^{-1}) was performed at William and Mary using an in-house focusing set-up coupled to a Woollam Variable Angle Spectroscopic Ellipsometer (W-VASE). Spectroscopic ellipsometry has the notable advantage over reflectance spectroscopy alone in that it preserves information related to the phase shift upon reflection, enabling the accurate determination of both the real and imaginary parts of the optical constants of the material. Data for three angles of incidence was obtained on the crystals oriented with their long axis parallel and perpendicular to the plane of incidence. The ellipsometry focusing setup introduces an angular spread in the incident beam of about $\pm 1^{\circ}$ which the data analysis takes into account. The same crystals and heating arrangement were used for both the reflectance and ellipsometry experiments. All data sets were analyzed together the W-VASE software with Kramers-Kronig consistent oscillators to obtain the broadband, frequency dependent complex conductivity parallel and perpendicular to the vanadium chains in the T and M_2 phases.

Details of the analysis of the ellipsometry and reflectance data are given in Appendix B.

4.3 RESULTS AND DISCUSSION

We present the first report on polarization dependent optical conductivity data on the infrared-active phonons of M_2 and T phases in Fig. 4.3. For the M_2 phase (space group $C2/\mathrm{m}$), group theory predicts 6 A_u phonon modes for light polarized parallel to the b_{M_2} axis oriented along the vanadium chains, and 9 B_u phonon modes for light polarized perpendicular to the b_{M_2} axis. We observe 5 A_u and all 9 B_u phonon modes in the experimental spectra. It is possible that the sixth A_u phonon mode has a weak dipole moment and therefore is not seen in experiment. The discontinuous structural phase transition to the T phase is

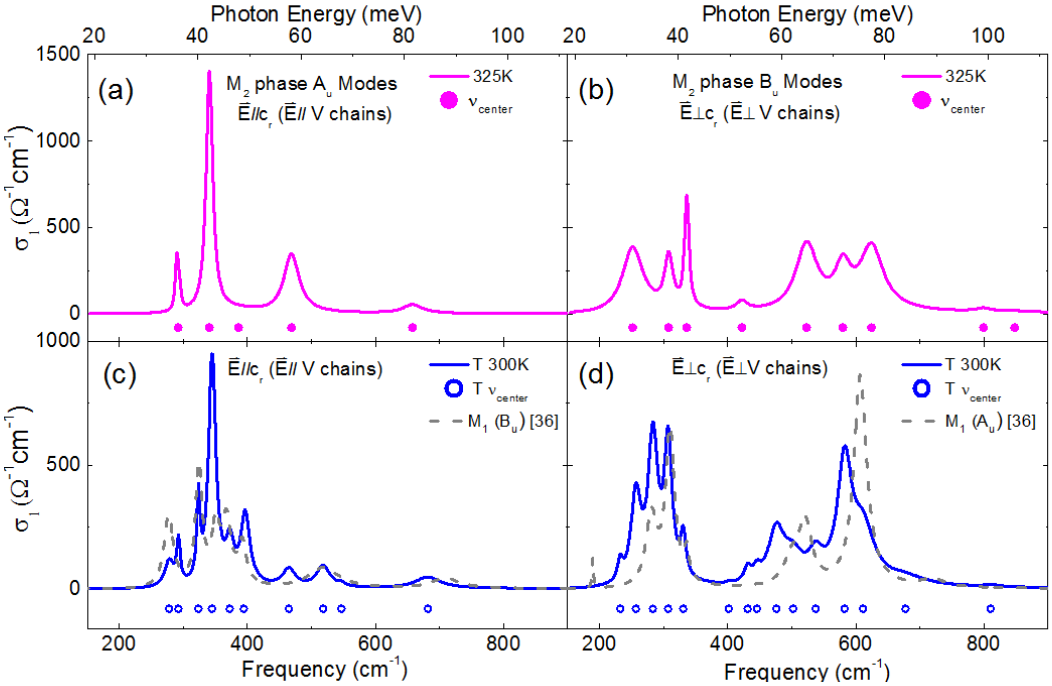

Figure 4.3 — Polarization dependent optical conductivity (σ_1) showing the infrared active phonon spectra of the M_2 phase (panels (a) and (b)), and the T phase (panels (c) and (d)). The center frequencies of the phonon features are denoted by circles labeled ν_{center}. The previously reported M_1 phase infrared active phonon spectra[36] (Chapter 3) are compared to the triclinic phase spectra in (c) and (d).

captured by the significant increase in the number of phonon features in the T spectra in both polarizations. This is explained by the lower symmetry of the triclinic structure (space group $P\bar{\bar{1}}$, $C\bar{1}$ in Pouget's notation[7]). In Fig. 4.3, we include the M_1 spectra from our previous work for comparison[36]. The M_1 phonon spectra resemble the T phonon spectra and lead to the conclusion that the T phase is merely a slight structural distortion of the M_1 phase. Indeed this is consistent with past observation of the continuous crossover from the M_1 to the T phase

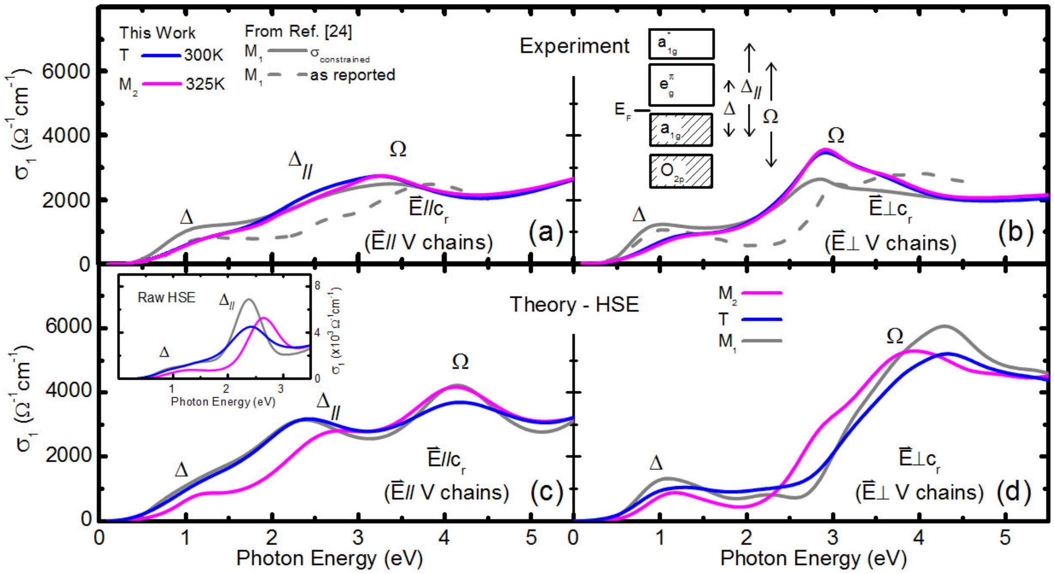

Figure 4.4 — Experimental optical conductivity σ_1 of the M_2 and triclinic T phases parallel to the vanadium (V) chains (a) and perpendicular to the vanadium (V) chains (b). Phonon features, which occur below 0.11 eV, are not shown. For comparison, accurate optical conductivity of the M_1 phase is extracted from the reflectance spectrum reported in [24] by using the complex conductivity of the T phase measured in this work as a constraint above 4 eV (see text). The inset in panel (b) shows an effective energy level diagram along with optical interband transitions that appear in the conductivity spectra. First-principles DFT optical conductivities calculated via the HSE functional are presented in (c) and (d). The calculated "raw" conductivities are broadened by 0.3 eV. The calculated conductivity for $E /\!/ c_R$ contains a very sharp $\Delta_{\parallel}$ feature (see inset of panel (c)). To account for lifetime effects not handled in the static HSE treatment, the $\Delta_{\parallel}$ feature, which is assigned to transitions between the lower and upper Hubbard bands in the Mott picture, is further broadened to a FWHM of 1.5 eV in the main panel of (c), which better models the experiment.

without latent heat[7]. This is in contrast to the first order phase transition between the M_2 and T phases.

We now turn to the inter-band transitions in the optical conductivity that a measure of the electronic structure. From Fig. 4.4, one can immediately see the optical conductivity, and thus the electronic structure, of the M_2 and T is nearly the same. This finding is remarkable given that there are obvious differences in the structural and magnetic properties between the two phases, as discussed above. Interestingly, numerous measurements on single crystals and thin films of the M_1 phase give almost the same magnitude of the energy gap as we measure in the M_2 and T phases [21,23,64,86,100,101]. The optical energy gap is the spectral region with vanishing conductivity. Above the gap, the optical interband transition labeled Δ, is quite rigid across this wide range of VO_2 samples.

For a direct comparison to the M_1 phase, in Figure 4.4 we show optical conductivity extracted from the reflectance spectrum of Verleur *et al.* on single crystals [24]. The complex conductivity is not uniquely determined by the reflectance intensity spectrum without knowledge of the reflectance phase. In addition to the optical conductivity reported in Ref.[24], we present an alternative determination of the optical conductivity using the T phase complex conductivity measured here to approximate the value of the M_1 reflectance phase shift in the high energy region of the spectrum. Using this constraint leads to an M_1 conductivity spectrum with a lower uncertainty than that reported in the original work, where the reflectance phase shift was not measured. The M_1 optical gap is nearly the same as that in the M_2 and T phases, and similar optical interband features are present in all three phases.

A schematic of the effective electronic structure of the vanadium *d*-bands for the three insulating VO_2 phases is shown in the inset of Fig. 4.4 (b). There are two features of particular note, labeled Δ and $\Delta_{||}$. The interband transition Δ

across the energy gap is centered about 1.2 eV for all three phases and has little polarization dependence. Similarly, $\Delta_{||}$ occurs around 2.5 eV in all phases for polarized along the vanadium chains, and is thus ascribed to transitions the bonding and anti-bonding a_{1g} bands. These can be thought of as the lower upper Hubbard bands in the Mott picture. The features labeled Δ occur at 3 eV or higher energies and are primarily optical interband transitions between O_{2p} states and the empty vanadium *d*-states. We emphasize that the robustness of the insulating phase band structure, despite the change in lattice structure, is a remarkable result that is not anticipated by conventional band theory.

4.4 THEORY

To investigate this behavior further, the Krakauer group at William and Mary performed *ab initio* hybrid DFT calculations on the three insulating phases with the Heyd-Scuseria-Ernzerhof (HSE) functional[110,111]. Calculated optical conductivities were determined from the imaginary part of the optical dielectric tensor, using the Vienna *Ab initio* Simulation Package (VASP)[112–115] with HSE (screened) exact-exchange fraction $\alpha=0.05$ and screening parameter $\mu=0.2$. The optical conductivity calculations are for vertical-only transitions (initial and final states are at the same k-point). The theoretical conductivities were broadened by 0.3 eV, except as indicated, to account for quasiparticle lifetime effects not included in HSE. With suitably chosen α, the HSE functional can, in many instances, provide a good description of electronic properties ranging from band to Mott-Hubbard insulators as shown in previous work [56,116]. The percentage α of exact-change in hybrid DFT can be semi-quantitatively related to the value of the Hubbard U parameter in DFT+U, with larger values of α (and U) yielding larger optical gaps [47,56,116]. Hybrid DFT and DFT+U both provide a mean-field treatment of on-site $3d$ correlation on the V atoms. Previous M_1 and M_2 HSE calculations[27,46,117] yielded too large band gaps compared to experiment. This can be attributed to using an α which is too large for $3d$ oxides[56], such as the default HSE06 value of $\alpha=0.25$[111]. The results of our hybrid DFT calculations are presented in Fig. 4.4 (c) and (d). In agreement with the experiment, we find that the energy values of the inter-band transitions, particularly Δ across the optical gap, are quite similar for all three phases. DFT+U calculations (U=5.7 eV and J=0.8 eV, using LDAUTYPE=1 in VASP, not shown) yield qualitatively similar results. This insensitivity to the change in lattice structure in all three insulating phases is incompatible with the Peierls picture. It is interesting to note that the $\Delta_{//}$ feature in the raw HSE result is much sharper than in experiment (see Fig. 4.4). This is indicative of short lifetimes for carriers excited between the bonding and anti-bonding a_{1g} bands in the real system that is not captured in the static HSE theory. Such lifetime broadening is characteristic of significant electron-electron interactions in these orbitals of Mott-Hubbard character. This is additional evidence that the splitting of the a_{1g} bands, and consequently the energy gap, arises from Coulomb correlations. The most recent iteration of DMFT electronic structure calculations finds energy gaps for the M_1 and M_2 phases that are consistent with our experimental results [54].

4.5 CONCLUSIONS

To conclude, the nature of the VO_2 insulating phases is now clear. The optical spectroscopy data presented in this work clearly demonstrates that the electronic structure of the VO_2 insulating phases is robust to changes in lattice structure and vanadium-vanadium pairing. In particular, the energy gap is insensitive to the dimerization of the equally spaced vanadium ions with localized electrons in the M_2 chains. This result is incompatible with a Peierls gap and is strong evidence that the gap arises due to Mott-Hubbard type Coulomb correlations. The negative Knight shift is indicative of localized electrons on the equally spaced vanadium ions in the M_2 chains. Its absence in the dimerized chains of all three phases[7] elucidates the key subtlety of the insulating VO_2 states: in contrast to a more conventional Mott insulator, where valence electrons are localized on individual ions, the dimerized vanadium chains chains contain bonded spin singlets which are localized on the vanadium dimers. This fact has made it difficult to conclusively distinguish between the Peierls and Mott-Hubbard pictures in the exhaustively studied M_1 phase. Study of the M_2 and T phases, with their non-equal V chains, is essential to decouple the effects of dimerization and electronic correlations. Seen in a broader context, our work paves a path for disentangling the contributions of the electronic and structural degrees of freedom to phase transitions in other correlated electron systems.

Chapter 5

Modification of electronic structure in compressively strained VO_2 films

5.1 INTRODUCTION

Strongly interacting degrees of freedom in condensed matter systems often lead to novel emergent properties such as metal-insulator transitions, colossal magnetoresistance, and high phase transition temperature (T_c) superconductivity.[89,91,118,119] Because they arise from multiple strongly interacting degrees of freedom, these emergent properties are highly sensitive to external factors such as temperature, strain, chemical doping, and applied fields. The true potential of strongly correlated systems lies in this sensitivity to external parameters. With sufficient understanding, the properties of these materials could be *engineered* to match specific applications. The technological impact of harnessing these novel properties for applications cannot be overstated.

Additional experimental data are needed to further inform our understanding of these materials. Unfortunately, the same sensitivity to external parameters that makes these materials so promising for future applications also makes experimental characterization difficult. The emergent properties can vary widely among different samples of the same material, as different growth techniques and conditions result in variations in strain, stoichiometry, and microstructure. Thus, for experimental measurements of these systems to provide meaningful insight, the external parameters, the intrinsic interacting degrees of freedom, and the resulting properties must all be well characterized. Hence, measurements on samples subject to external perturbations, for example pressure and strain[8,62,108,109,120,121], can provide additional insight into the underlying physics of these systems.

Vanadium dioxide (VO_2) is perhaps the canonical strongly correlated transition metal oxide; its relatively simple unit cell and stoichiometric composition make it an ideal material to study strong correlations. Bulk VO_2 undergoes a metal-insulator transition (MIT) at T_c=340K between an insulating phase below the T_c and a metallic phase above the T_c. The MIT is accompanied by a structural transition between the insulating monoclinic M_1 lattice and the conducting rutile (tetragonal) lattice (See Fig. 5.1(a)). As the vanadium atoms are in the 4+ valence state, there is expected to be one electron in the vanadium *d*-orbitals. The crystal field of the oxygen octahedron splits the vanadium *d*-orbitals into two higher energy e_g^σ orbitals, which contain lobes pointing towards the oxygen atoms, and the remaining three lower energy t_{2g} orbitals. The t_{2g} orbitals are additionally split into two e_g^π and one a_{1g} orbital. The a_{1g} band has lobes pointing along the rutile c_r (monoclinic M_1 a_M) axis and is slightly lower in energy than the e_g^π band.

Early on, a simple scheme was proposed by Goodenough to explain the role of the structural transition in the MIT in terms of the vanadium *d*-orbitals.[17] The structural change from rutile to monoclinic M_1 has two salient features: a dimerization of the vanadium atoms along the rutile c_R (a_{M1}) direction, and an antiferroelectric type tilting of these vanadium dimers relative to the surrounding oxygen structure. Insulating behavior was proposed to arise as follows. The dimerization would lead to a splitting of the a_{1g} orbitals into bonding (a_{1g}) and antibonding (a_{1g}^*) bands, while the antiferroelectric tilting of the vanadium pairs would lead to an upshift of the e_g^π orbitals away from the Fermi energy to produce a gap between the filled bonding a_{1g} band and the empty e_g^π band[17]. This effective band-structure scheme is qualitatively supported by experimental data on bulk crystals and thin films[23,24,64].

However, a precise quantitative understanding of how this scheme is realized—in particular the roles of electronic correlations and the structural instability in the MIT—had been a matter of debate for decades[9,18,107,122]. Our work in chapter 4 demonstrates that the energy gap in the insulating phases is due to electronic correlations. Nevertheless, a complete understanding of this correlated system as a function of external parameters is necessary to predict and control the emergent properties.

Broadband infrared (IR) and optical spectroscopy is a powerful technique for investigating the MIT in VO_2 because it provides insight into both the lattice and electronic structure, via the IR active phonons and optical interband transitions, respectively. Previous IR and optical spectroscopy experiments have been performed on bulk VO_2 and thin films.[23,24,35,36,64] However, VO_2 films grown on different substrates and by different techniques can have significantly different strain states and microstructure. Because of the extreme sensitivity to external parameters in strongly correlated systems mentioned previously, accurate characterization of the strain and microstructure of various films, and the resultant emergent properties, can provide additional insight into the physics of these materials.

In this work we report the IR and optical properties of a VO_2 film grown on a quartz substrate. The chapter is organized as follows. We start with a thorough description of our preliminary characterization of the sample and then describe the IR and optical spectroscopy experiments. Next, we report our results on the IR active phonons in the M_1 phase. We then report and discuss the strain induced changes of the electronic inter-band transitions in both M_1 and rutile phases. We conclude with a brief summary of important results and their implications. Technical details of the experiment and data analysis are presented in Appendix C.

5.2 EXPERIMENTAL METHODS

A. Sample characterization

The VO_2 film used in this experiment is a 70nm thick VO_2 film on a 0.5 mm thick (001) quartz substrate. The film was synthesized using the Reactive Biased Target Ion Beam Deposition (RBTIBD) method.[123] The growth conditions for optimal stoichiometry are the same as those reported elsewhere.[123,124] An atomic force microscope image of the sample, shown in Fig. 5.1(b), indicates that the VO_2 film consists of many individual grains with an in-plane size of about 100 nm. X-ray diffraction shows that the individual

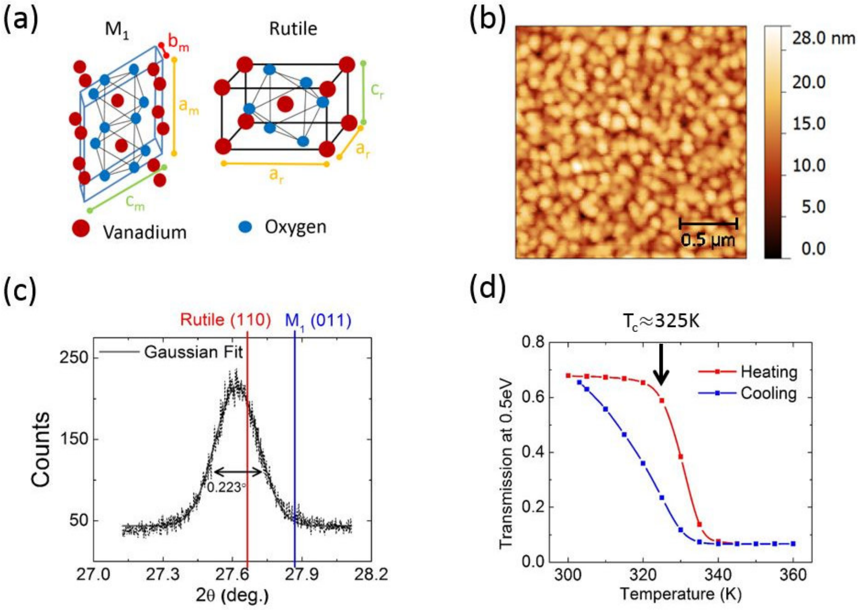

Figure 5.1 — (a) Lattice structure of the M_1 and Rutile phases of VO_2. (b) AFM image at room temperature showing the surface roughness and multi-grain structure of the $(011)_{M1}$ VO_2 film on quartz substrate. (c) X-ray diffraction peak resulting from the $(011)_{M1}$ lattice planes. The Gaussian fit and resulting full width at half maximum is shown. The peak positions for the bulk (011) M_1 and analogous (110) rutile diffraction spots are shown as vertical lines. (d) Transmission through the sample at a photon energy of 0.5 eV, demonstrating the temperature dependence of the transition during heating and cooling runs. Note the T_c onset of 325K is significantly lower than that of bulk crystals (340K).

VO_2 grains are oriented such that the (011) plane of the monoclinic M_1 phase is in is in the plane of the substrate (See Fig. 5.1(c) and Appendix C). This becomes the the (110) plane in the rutile structure. However, there is no preferred orientation orientation of the grains with respect to rotations about the out of plane direction. direction.

The first-order phase transition in this film exhibits the classic hysteresis usually observed in VO_2. The temperature dependent transmission through the VO_2 film-substrate system at 0.5 eV provides a clear picture of the hysteresis loop for the

MIT in this particular film (See Fig. 5.1(d)). The photon energy of 0.5 eV is just below that of the energy gap in insulating VO_2 resulting in minimal absorption and high transmission intensity. The transmission drops with the occurrence of metallicity in the vicinity of the MIT due to the increased reflectance and absorption of the metallic phase. The T_c of the film is depressed from the bulk T_c of 340 K to 325 K. The 15 K width of the hysteresis loop in this film is somewhat broader than what is seen in VO_2 crystals.[106] Such broadening of the hysteresis and the phase transition is typical of polycrystalline VO_2 thin films because of variation in grain size and strain inhomogeneity. This inhomogeneity is consistent with the width of the x-ray diffraction peak shown in Fig. 5.1(c).

B. Spectroscopic methods

Spectroscopic measurements were performed to study the optical properties of the VO_2 film on quartz between 7.5 meV and 6.0 eV. This broad spectral range is necessary to characterize both the electronic and lattice degrees of freedom. Specifically, temperature dependent spectroscopic ellipsometry was performed in the spectral range between 0.6 eV and 6.0 eV at temperatures of 300 K and 360 K. The VO_2 is in the M_1 insulating phase at 300 K and in the rutile metallic phase at 360 K. Due to its self-referencing nature, spectroscopic ellipsometry enables very precise measurement of the complex dielectric function of the sample. To extend our spectral range into the far-IR, near-normal incidence reflectance between 7.5 meV and 1 eV was obtained at 300 K and 360 K. In addition to the VO_2 film on quartz, the same temperature dependent spectroscopic measurements were performed on the (001) quartz substrate. In order to obtain the optical constants of the VO_2 film, the ellipsometry and reflectance data for the substrate and the VO_2 film-substrate system was fit with Kramers-Kronig consistent Drude, Lorentzian, Tauc-Lorentzian, and Gaussian oscillators. We report the optical constants of the VO_2 film at 300 K and 360 K in the insulating and metallic phases respectively. Spectra and fits, in addition to technical details about the modeling procedure, are included in the Appendix C.

5.3 RESULTS AND DISCUSSION

A. Sample strain

In a polycrystalline thin film that is not lattice matched to the substrate, such as the one studied in this chapter, the resultant strain state of the film is particularly dependent on the growth technique. Stresses occur between neighboring grains, and have been shown to affect the T_c of VO_2.[125] Such strain is sensitive to the grain size and film microstructure and both these properties are influenced by the growth conditions. There are additional factors present in sputtered films[126]. Of particular note is a process referred to as “shot in which compressive strain arises as a result of the sample being bombarded energetic particles during growth. Compressive in-plane strain in sputtered films is often attributed to this effect[127,128]. Thermal strain from the mismatch of the coefficient of thermal expansion between the film and substrate may also be present.

The out of plane strain can be calculated by comparing the measured x-ray diffraction data shown in Fig. 5.1(c) with the literature. X-ray diffraction shows that the $(011)_{M_1}$ plane spacing is 3.23 Å in the present sample. From the literature, the $(011)_{M_1}$ plane spacing ranges from 3.1978 Å and 3.2067 Å for bulk VO_2.[129],[15] Averaging the literature values implies a tensile strain in the out of plane direction of 0.89%. This type of tensile strain would result from compressive strains in the plane of the substrate. The transition temperature for the MIT is expected be most sensitive to strain along the a_M (c_R) direction.[52] Depression of the T_c to 325K, as is the case in our film, has been seen in VO_2 nanorods with a compressive strain of 1.5% along a_{M1}.[109] Similar strong dependence of the T_c as a function of strain has been seen in VO_2 films on TiO_2[130]. In both cases, compressive strain along a_{M1} results in depression of the transition temperature. Thus it is reasonable to conclude that the VO_2 film we studied has a compressive strain of about 1.5% along a_{M1}.

The a_M axis contracts by about 1% across the phase transition into the rutile phase. This would tend to relax compressive strains along c_R (a_{M1}) in the metallic phase. Some partial relaxation of the in-plane strain is evidenced by the shift of the x-ray diffraction peak towards the bulk rutile value shown in the Appendix C. However, as the out of plane strain in the metallic phase is still tensile, the in plane strain is still somewhat compressive. Additional changes to the strain as the sample is heated across the MIT could be induced due to the mismatch of thermal expansion coefficients between the VO_2 film and quartz substrate. The coefficients of thermal expansion of a_R VO_2, c_R VO_2, and a-axis quartz are $4x10^{-6}$/K, $25x10^{-6}$/K, and $16x10^{-6}$/K, respectively[11,131]. Thus, this is at most a 0.1% effect over the 60 K temperature range investigated in this work and has negligible impact on the strain state of the film.

Here we discuss the stoichiometry of the VO_2 films we have studied in this work. One effect of oxygen deficiency is to reduce T_c. However, oxygen deficiency also increases disorder in the film which significantly reduces the jump in the dc conductivity across the metal-insulator transition[124]. In the films studied in our work, the optical conductivity in the low frequency limit changes by four orders of magnitude across the metal-insulator transition. This is consistent with stoichiometric VO_2 with minimal oxygen deficiency, comparable to single Moreover, the fact that we clearly see VO_2 optical phonon features in the is further evidence that the film is composed of crystallites with minimal due to oxygen deficiency. Hence the reduction in T_c in our films is due to compressive in-plane strain rather than oxygen deficiency.

B. IR active phonons and lattice dynamics

Due to the polycrystalline nature of the film, we measured the reflectance with unpolarized light. Thus, features due to IR active phonons of both A_u and B_u symmetries are expected to appear in the reflectance data in the insulating M_1 phase. However, the relative strengths of each phonon will depend on the orientation of the dipole moment relative to the plane of the sample: phonons with in-plane dipole moments will have a larger contribution to the effective optical constants.[35,36] The dipole moments of the A_u phonon modes, which lie parallel to b_M, are at 45 degrees out of the plane of the substrate in this film geometry. In contrast, the B_u modes have dipole moments in the a_M-c_M plane. Depending on the specific B_u mode in question, the dipole moments could be anywhere from 0 to 45 degrees out of plane. Thus, all 15 IR active phonons should, in principle, contribute to the measured spectrum.

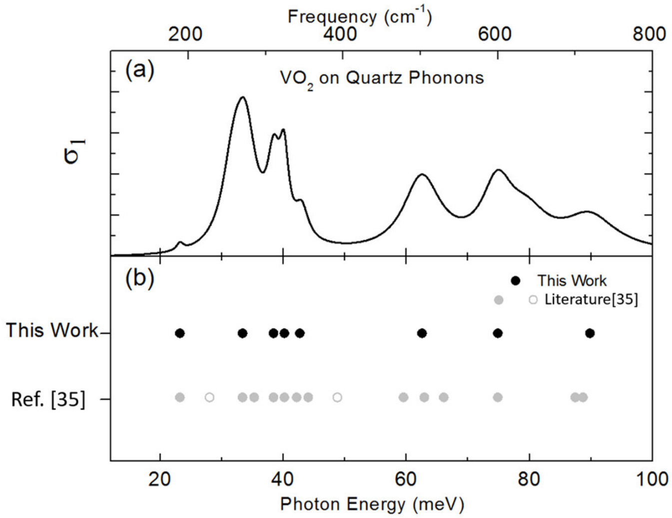

Figure 5.2 — (a) Measured imaginary part of the complex dielectric function (ε_2) of the VO2 film in the phonon region. (b) The measured center frequencies of the IR active phonons of the VO2 film are compared to previous data taken on bulk crystals[35]. Open circles denote phonon modes from Ref. [35] that are not obvious in the spectra measured in this work (See Text).

The measured imaginary part of the complex dielectric function in the phonon region of the VO$_2$ film is shown in Fig. 5.2(a). We are able to resolve 8 IR-active phonons in this work. The IR active phonons in VO$_2$ crystals have been previously characterized by optical spectroscopy [35,36]. It is not unusual that we resolve fewer than the expected 15 IR-active phonons, as some VO$_2$ phonons overlap. Moreover, the sample is a thin film, resulting in much weaker phonon features in comparison to those of the quartz substrate which dominate the measured spectrum in this region. More importantly, the clearly resolved VO$_2$ phonon center frequencies differ from the bulk values by at most 1.3% (See Fig. 5.2(b)). Raman spectroscopy performed on films grown by the same method also shows negligible shift in the phonon center frequencies compared to bulk VO$_2$.[132] Remarkably, the lattice dynamics are virtually unchanged relative to bulk VO$_2$ in a film where the T$_c$ is so significantly depressed.

Previous experiments have seen that spectral features due to the rutile phase phonons are fairly weak and difficult to resolve from the metallic background.[35,36] In this work, IR active phonon features in the rutile phase are not observed in the reflectance spectrum. Apart from the high conductivity of VO_2 in the metallic phase, the absence of rutile phonon features in this work can be attributed to the thin film nature of the sample and strong phonon features of the quartz substrate.

C. Inter-band transitions and electronic structure

i. Assignment of spectral features

In the absence of polarization dependent data due to the polycrystalline nature of the film, features in the optical conductivity cannot be unambiguously assigned to specific interband transitions. However, energy scales of the measured spectral features can still be discussed within the context of band theoretical results on VO_2[48,78]. A schematic view of the band structure of VO_2 is shown in Fig. 5.3 to support the following discussion. Note that the lower (LHB) and upper (UHB) Hubbard bands, which, in the rutile phase, arise from electronic correlations not considered by conventional band theory, are shown explicitly in Fig. 5.3.

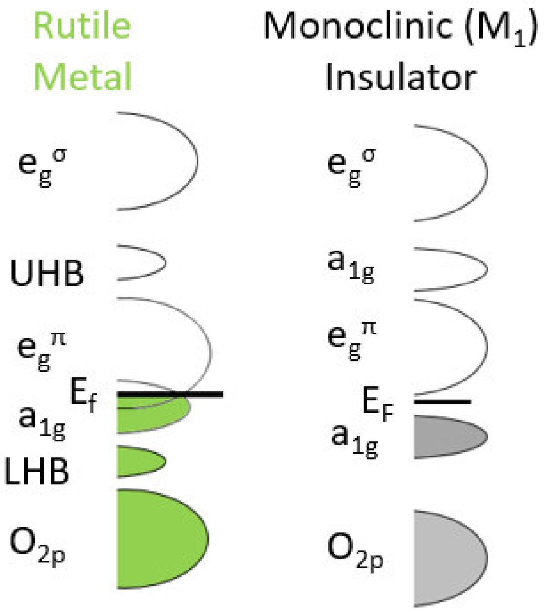

Figure 5.3 — Schematic showing energy levels of the relevant vanadium and oxygen bands in the metallic and insulating states of VO_2. The Fermi level is denoted as E_F. The possible (partial) Hubbard splitting of the a_{1g} band due to correlation effects in the rutile metal is shown explicitly.

The measured optical conductivity for the rutile phase at 360K is shown in Fig. 5.4(a). Some of the lower energy inter-band transitions in this compressively strained sample differ significantly from those measured previously on bulk VO_2 and thin films.[23,24,35,64] The VO_2 film on quartz exhibits a broad Drude-like metallic response “q” and an interband transition “s” which are consistent with previous works. Feature “s” at 3.1 eV is attributed to transitions between the O_{2p} orbitals and the vanadium e_g^π bands. However, in this strained VO_2 film on quartz, we resolve additional features: a pseudo-gap type feature in the low frequency electronic response “p”, and well-defined features, “r” and “t”, at 2.2 and 5eV, respectively. The pseudo-gap type feature, “p”, has been seen in a few previous works.[36,86] Compressive strain along c_r is expected to lower the energy of the a_{1g} band[17]. That compressive strain results in a lowering of the energy of the

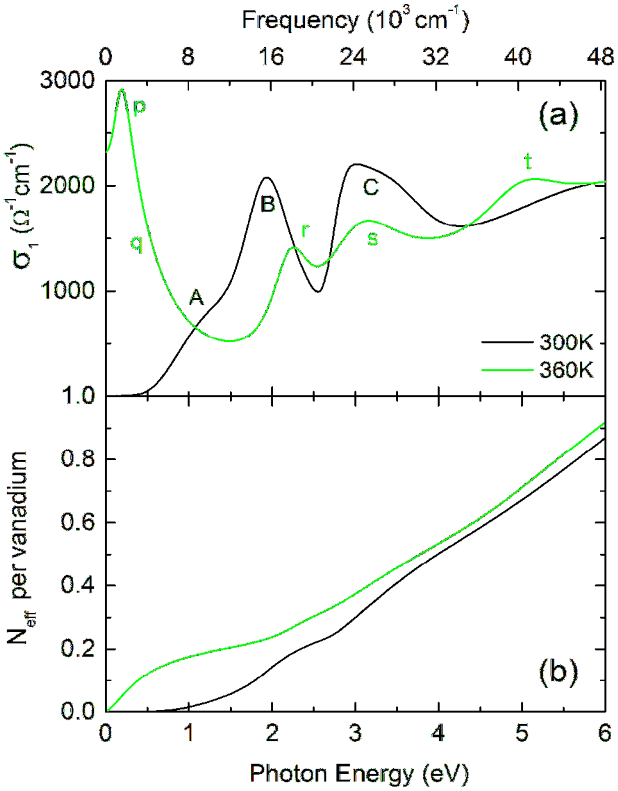

Figure 5.4 - (a) Optical conductivity σ_1 for the rutile (green) and M_1 (black) phases as a function of photon energy. Phonons have been subtracted from the conductivity of the M1 phase and this procedure has negligible impact on the calculation of Neff. Spectral features are denoted by lower and upper case letters for the rutile and M_1 phases respectively. The assignment of these spectral features to specific inter-band transitions is discussed in the text. (b) The effective number of carriers per vanadium atom (See text).

a_{1g} band is supported by X-ray emission spectroscopy experiments on strained VO_2 films grown on TiO_2.[133] The slight lowering of the filled a_{1g} bands relative to the e_g^{π} bands could account for the prominence of the pseudo-gap type feature "p" if this feature is due to optical transitions between those two bands. This lowering in energy of the a_{1g} band, due to compressive strain, would increase the occupation of the bottom half of the a_{1g} band. Increased occupation of the a_{1g} band could lead to a reduction in screening and an increase in electronic correlation effects for electrons in the a_{1g} bands, similar to the explanation presented by Zylbersztejn and Mott for the insulating M_1 phase.[18]

Correlation effects in the rutile phase could lead to a degree of splitting of the a_{1g} band into lower and upper Hubbard bands.[134] A "satellite" of the a_{1g} band, consistent with this type of lower Hubbard band, has been seen previously in photoemission experiments on bulk VO_2.[21] We interpret feature "r" as transitions from the filled parts of the a_{1g} bands (both the unsplit portion and the lower Hubbard band) to the unfilled upper Hubbard band. Such splitting could also account for feature "t" if it is assigned to the transition between the O_{2p} and upper Hubbard bands. There is also likely some absorption near 5 eV due to transitions between the O_{2p} and e_g^σ bands, as the O_{2p} to e_g^π transition is seen at 3 eV, and the crystal field splitting between e_g^π and e_g^σ is expected to be on the order of 2 eV.[135] That a well resolved feature at 5 eV is not present in the M_1 phase supports the assignment of feature "t" to a transition involving the upper Hubbard bands, as these bands might be expected to shift more significantly across the MIT. In this scenario, the upper Hubbard band would need to lie at an energy very close to that of the e_g^σ bands. This would imply a correlation induced Hubbard splitting of a comparable magnitude to the crystal field splitting, and is expected to be much larger than the splitting caused by a Peierl's type lattice distortion.

Increased correlations due to compressive strain, as discussed above, would result in more states being shifted into the satellites of the a_{1g} orbital, and could account for why we are able to clearly resolve features “r” and “t” in this sample. It is also possible that correlation effects lead to significant splitting of the a_{1g} bands even in the unstrained rutile phase. Subtle evidence of a transition the Hubbard bands was seen previously in rutile VO_2 on sapphire near 3 eV.[23] However, this feature could not be clearly resolved from the O_{2p} to e_g^π transition. Thus, it’s also possible that this feature has in fact been shifted to a lower energy in our particular film.

The measured optical conductivity for the M_1 phase at 300 K is shown in Fig. 5.4(a). Features “A” and “C” are consistent with previous works.[23,24,64] Feature “A” is attributed to transitions between the filled bonding a_{1g} and the empty e_g^π bands, while feature “C” is attributed to transitions between the filled O_{2p} and empty e_g^π bands. The energy gap of ≈ 0.6 eV is similar to that seen in bulk VO_2 crystals and other thin films[22–24].

We observe an additional feature, “B”, which is different from previous works. While a strong feature at low energy, around 0.9 eV, is seen in single crystals for light perpendicular to a_M,[24] feature B in the present work is somewhat stronger and at a much higher energy, 1.9 eV. A similar strong feature at 1.9 eV is not seen in previous work on thin films grown on sapphire and TiO_2.[23,64]

Interestingly, the transition between a_{1g} and a_{1g}^* ,which has been seen in previous experiments on bulk crystals and thin films around 2.5 eV[23,24], is not not clearly present near this energy in the VO_2 on quartz data. It is likely that this this transition has been down-shifted as a result of strain. It is possible that feature "B" is in fact the $a_{1g}$to a_{1g}^* transition, having been shifted to lower energies in this particular film. Such an interpretation is not unreasonable, given that the analogous feature in the rutile, feature "r", occurs at a very similar energy to feature "B". However, recent dynamical mean field theory (DMFT) calculations show that the splitting between a_{1g} and a_{1g}^* should increase with compressive strain along the a_M axis.[52] Such an increase in splitting would result in a shift of the a_{1g} to a_{1g}^* transition to higher energies, into the vicinity of feature C. Indeed, there is fine structure in feature "C" that would be consistent with such an explanation.

Note that the evidence for Hubbard bands in the rutile metal suggests that correlation effects are significant enough to govern the evolution of VO_2 properties upon lowering temperature. In Goodenough's band theory picture, the anti-ferroelectric displacement of the vanadium atoms in the M_1 structure is necessary to raise the energy of the e_g^π bands above the Fermi energy to produce an energy gap.[17] It is interesting to note, however, that in both the present experiment and previous work,[23] the O_{2p} to e_g^π transition is not shifted appreciably, certainly much less than the 0.6eV band gap of M_1 VO_2. This could indicate that the e_g^π band itself is not as strongly dependent on the change in lattice symmetry as expected. Alternatively, the O_{2p} bands may also shift significantly across the transition.

ii. Spectral weight transfer

As the "f-sum rule" is a fundamental statement of conservation of charge in a material, it should be conserved across the MIT. The total spectral weight (A_{total}) is conserved as follows. Note that the following equations employ Gaussian (cgs) units.

$$\mathrm{A_{total}} \equiv \int_0^\infty \sigma_1(\nu)\,\mathrm{d}\nu = \frac{\mathrm{ne^2}}{\mathrm{4cm_0V}} \tag{5.1}$$

Where $\sigma_1(\nu)$ is the real part of the optical conductivity as a function of photon energy hcν, n is the number of electrons in a volume V of the material, e is the elementary charge, and m_0 is the free electron mass. By integrating to a finite frequency, one can consider the spectral weight (A) below a certain photon energy (hcν_c)

$$A(\nu_c) = \int_0^{\nu_c} \sigma_1(\nu) d\nu \tag{5. 2}$$

It is interesting to define N_{eff} which, in the spirit of equations (1) and (2), gives us the *effective* number of carriers with optical mass equal to m_0 that contribute to absorption below a certain photon energy, $hc\nu$.

$$N_{eff}(\nu_c) = \frac{4cm_0V}{e^2} \int_0^{\nu_c} \sigma_1(\nu)\, d\nu \tag{5.3}$$

The optical conductivity and effective number of carriers is shown in Fig. 5.4(b) as a function of photon energy. The volumes used for this calculation is ½ of the rutile[11] and ¼ of the M_1[15] unit cell volumes from the literature. This corresponds to the volume of a single formula unit, and thus a single vanadium atom. While there are some slight shifts in spectral weight up to and exceeding 6 eV, 95% of the spectral weight has been recovered by 4 eV. That the f-sum rule is still not fully satisfied at such high energies clearly indicates a rearrangement of the electronic structure at even higher energies. For example, feature “t”, clearly resolved in the rutile phase at 5 eV, is not present in the M_1 phase. Such rearrangement at higher energy scales supports the hypothesis that the MIT in VO_2 is electronically driven. Previous optical spectroscopy measurements have also shown shifts in spectral weight across the MIT up to and exceeding 6 eV.[23,64]

The spectral weight of the conduction electrons (features “q” and “p”) in the rutile phase will be largely contained below 1.8eV in the broad-Drude-like While one might naively expect one conduction electron per vanadium atom, N_{eff} at this energy is only 0.21. This indicates that either the effective electron mass (m*) of the conduction electrons is several times m_0 and/or the spectral weight of the correlated vanadium $3d$ electrons has shifted to energies higher than 1.8 eV.

5.4 CONCLUSIONS

The properties of strongly correlated condensed matter systems can change dramatically when subject to external perturbations such as strain. In the VO_2 film on quartz film investigated in this work, compressive strain along the a_{M1} (c_R) direction results in the T_c being shifted down to 325 K from the bulk T_c of 340 K. Broadband IR and optical spectroscopy was used to characterize both the electronic and lattice-structural degrees of freedom in this film to elucidate the cause of this significant change in T_c, and its implications regarding the nature of the MIT in VO_2.

Strain affects the inter-band transitions by altering the relative energies of the bands, as well as their orientation in real space. Such changes can have important implications in correlated system where the Coulomb repulsion between electrons, orbital overlaps, and screening play nontrivial roles. While the energy gap in the M_1 phase is quite similar in various single crystal[24] and thin film[22,23] samples, some of the inter-band transitions in this strained VO_2 film differ significantly. In particular, two new features are observed. Features at 2.2 eV and 5.2 eV are observed in the rutile phase which we attribute to transitions between the filled a_{1g} and O_{2p} states and the upper Hubbard band. It is possible that this feature is more prominent because the compressive strain along c_r increases the occupation of the a_{1g} orbital, thereby reducing screening and enhancing correlation effects. A new feature is seen around 1.9 eV in the monoclinic M_1 phase; the values of ε_2 and σ_1 are significantly higher at this energy than in bulk crystals or other thin films. A definitive assignment of the a_{1g} to a_{1g}^* optical interband transition is not possible at present although there are two possible scenarios: Either it has been shifted down to 1.9 eV due to strain and appears as feature "B", or it appears as fine structure in feature "C" near 3 eV.

Interestingly, unlike the inter-band transitions, the IR active phonons in these strained films are very similar to their bulk counter-parts, indicating that the forces between the vanadium and oxygen ions remain largely unchanged despite the strained nature of this film. Nevertheless, this strain is sufficient to cause significant changes in the transition temperature and the optical inter-band transitions. This would indicate that the T_c is more sensitive to changes in the orbital overlaps and occupation than it is to changes in the lattice dynamics. reinforces the conclusion made in chapter 4 that the MIT in VO_2 is driven by changes in electronic correlations and orbital occupations rather than by lattice dynamics. The change in lattice structure could then occur as a consequence of the variations in electronic structure and interactions.

As the electronic and optical properties of VO_2 are incredibly sensitive to strain, this system has potential for applications for which strain engineering could be used to tune these properties. We have measured and documented the IR and optical properties of VO_2 film on quartz substrate. This is a necessary step towards fully realizing the potential of strain engineering this material.

Chapter 6

Repeatable nanoscale phase coexistence in VO_2 films

6.1 INTRODUCTION

It is generally believed that in first-order phase transitions in solids, the formation of phase domains must be affected to some extent by random processes. The randomness would lead to unreliable performance in nanoscale devices that have the potential to exploit the transformation of physical properties in a phase transition. Here we show that nanoscale randomness is completely suppressed in the thermally driven metal-insulator transition (MIT) in sputtered vanadium dioxide (VO_2) films. The nucleation and growth of domain patterns of metallic and insulating phases occur in a strikingly reproducible way. The completely deterministic nature of domain formation and growth in films with imperfections is a fundamental finding. Moreover, it opens the door for realizing reliable nanoscale devices based on the MIT in VO_2 and similar phase change materials.

The metal-insulator transition (MIT) in vanadium dioxide (VO_2)[89–91] has the potential to lead to a number of disruptive technologies, including ultra-fast data storage, optical switches, and transistors which move beyond the limitations of silicon[136–138]. For applications, VO_2 films are deposited on crystalline substrates to prevent cracks observed in bulk VO_2 crystals across the thermally driven MIT. Near the MIT, VO_2 films exhibit nanoscale coexistence[61,86,87] between metallic and insulating phases, which opens up further potential applications such as memristors, tunable capacitors,[139–142] and optically engineered devices such as perfect absorbers[143]. The phenomenon of phase coexistence is quite broadly observed across strongly correlated condensed matter systems, occurring for example, in the high-T_c superconducting cuprates[144,145], the colossal magnetoresistive manganites [146–148], as well as the oxides of vanadium[61,86,149–151]. Highly ordered patterns[61,144,145,148,151] result in response to long range interactions. Generally speaking, the spatial periodicity of these patterns ranges from very small (nanometers or less)[144,145] for strong interactions, such as Coulomb interaction between domains, to hundreds of nanometers or more for somewhat weaker interactions [61,148,150,151] such as long-range elastic mismatch with a substrate. The increasing periodicity as the interaction strength decreases is attributed to the free energy cost of forming the boundary between domains. In In this situation, random processes, such as fluctuations between phases[151] or irreproducibility in the domain pattern upon thermal cycling[150] have been observed. In contrast, amorphous patterns are also commonly observed when imperfections disrupt the long range interaction.[86,147] Generally speaking, there is sparse experimental data on the reproducibility of these patterns.

Due to the stochastic nature of nucleation of a new phase during a first order phase transition, it was expected that this randomness constituted an inherent challenge to creating reproducible phase transition based devices on the scale of the domain size. Until now, the expectation for these systems was that although some regions may preferentially transition due to inhomogeneity and defects, some degree of randomness was unavoidable[97,147,150]. The primary result of our work is that it is *possible* to realize completely reproducible metal-insulator phase domain patterns in a VO_2 film. Insight gained through our work could be applied to VO_2 and across the entire range of similar correlated materials, whose novel phase transitions have tremendous potential for technological impact[152]. The primary finding in this work is obtained with the technique of scattering-type scanning near-field infrared microscopy (s-SNIM). This technique was utilized to image the patterns formed by coexisting metallic and insulating domains in the thermally driven MIT in a sputtered VO_2 film. We achieved unprecedented spatial over a broad temperature range which allowed us to obtain s-SNIM images in same area of the film for repeated heating and cooling runs.

6.2 EXPERIMENTAL

In this work, we study a 45 nm thick VO_2 film grown by RF sputtering on (001) sapphire. In such films, the monoclinic angle ($\approx 123^\circ$) of the M_1 phase tends to align in plane along the 120° angles of the hexagonal sapphire lattice. Thus, grains in this film will prefer one of six possible orientations, differing by an out of plane rotation, due to the rotational symmetry of the hexagonal sapphire substrate[153]. Sputtered films tend to have some additional compressive in-plane strain due to an effect known as "shot peening[126]." Compressive strain along the a_{M1} (c_R) axis stabilizes the rutile phase, resulting in a somewhat lower T_c. These films are ideal for this work in that they have distinct topographic features, in the form of "valleys", which can be used to ensure that images are consistently taken in the same area. Thermal drift was minimized by placing the sample and measurement region at the center of a circular heating stage, which was designed in-house. A silicon diode based thermometer and a resistive heating element were mounted on the stage and these components along with a Lakeshore model 335 temperature controller were employed for thermal management. A slow temperature ramp rate $\approx$ 0.2K/minute was used to minimize overshooting (<0.1K) of the set-point temperature. Minute differences in this overshoot can result in an image that appears somewhat more progressed in one run as opposed to another. Once the set point temperature is obtained, it is held stable within 0.1 K for the full duration of the scan.

In s-SNIM, infrared light is scattered from a metal coated tip of a tapping mode atomic force microscope (AFM)[154]. The scattered light contains information about the near-field interaction between the tip and the optical properties of the region of the sample immediately below the tip. This procedure allows for the simultaneous collection of topographic and optical images of a given region of the film, with resolution on the order of the AFM tip radius, approximately 15 to 20 nm. The pseudo-heterodyne detection scheme and demodulation of the optical signals at the third harmonic are used to reduce various background contributions[154,155]. The s-SNIM technique is primarily sensitive to the local dielectric function at the incident infrared wavelength. However, the local topography can influence the signal, i.e. the signal is generally higher in a valley than on a topographic peak. This surface roughness ($\approx$ 3 nm RMS) induced s-SNIM contrast can be seen in the low temperature (purely insulating) images, and causes a variation of around 10%. The wavelength of 10.6 μm used in this work is within the band gap of insulating VO_2, and above the infrared active phonon region. The large change in optical constants across the MIT at this wavelength results in significant infrared contrast between metallic regions (high infrared signal) and insulating regions (low infrared signal), much greater than that caused by the topography. That the s-SNIM images presented here are due to the MIT is clear because they are temperature dependent while the topography is temperature independent.

6.3 RESULTS AND DISCUSSION

Representative s-SNIM images obtained in the same spatial region are presented in Fig. 6.1 Each row represents a separate heating or cooling run through the phase coexistence regime. The nucleation and growth of phase domain patterns are reproducible for the heating runs and the cooling runs respectively. However, somewhat different patterns are observed in the heating runs compared to the cooling runs. As has been seen previously in polycrystalline VO_2 films, the MIT is percolation-type in which phase domains

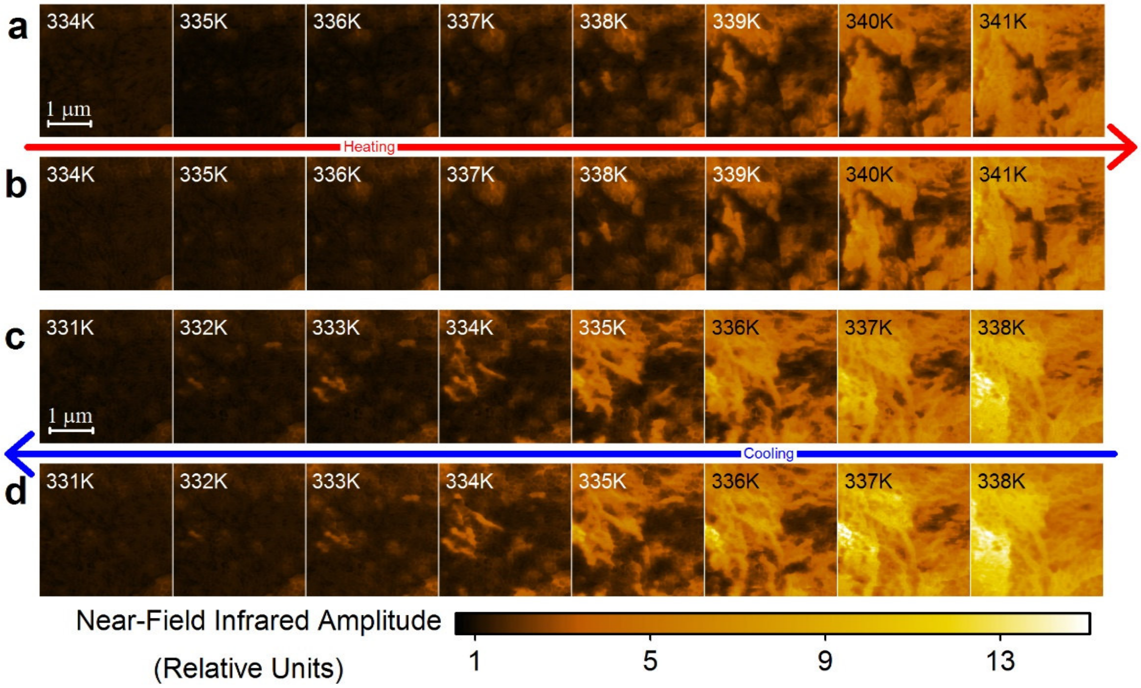

Figure 6.1 — Near-field infrared amplitude images of the same region at different temperatures are displayed. Higher infrared amplitude corresponds to metallic regions, while lower signals correspond to insulating regions. The signals are normalized to the average signal of the completely insulating 329 K image (not shown). Rows a and b show separate heating runs. Rows c and d show separate cooling runs.

first nucleate and then grow in amorphous, fractal-like patterns[86,87,149]. The patterns are static and stable in time, provided the temperature is held constant. constant. While the shapes of these phase domains are reminiscent of those observed in random percolation models of phase transitions, the fact that these domains nucleate and grow in the same way on separate runs through the MIT is evidence that deterministic effects alone dictate the domain patterns. It follows that the domain patterns depend on factors such as grain boundaries, relative orientation of grains, impurities, defects, and dislocations, which are "quenched", or frozen into the film at the time of growth. While the variance introduced by this “quenched disorder” can be treated as random in theoretical models[156], this does not imply that phase domain formation is necessarily a probabilistic (or random) physical process.

The s-SNIM images were taken over a number of runs through the metal-insulator transition. To investigate the reproducibility of the patterns produced by the phase domains, raster scans were taken in the same area on the film in repeated thermal runs. We performed two heating runs in three different regions of the film for a total of six heating runs. In none of the regions was any evidence of randomness observed. Three cooling runs were performed at the location shown in Fig. 6.1 to compare the patterns to the heating runs in the same location and to verify the repeatability for cooling. The three cooling runs showed reproducible patterns of coexisting phases (two of the three cooling runs are shown in Fig. 6.1). In all of the above runs, the sample was first brought to a temperature completely outside of the phase coexistence regime where it was fully metallic (for cooling) or fully insulating (for heating).

To obtain further insight into the domain pattern formation, we report a non-monotonic temperature cycle through the phase coexistence region in a common area of the film in Fig. 6.2. Interestingly, although the same pattern reemerges at 341 K, the phase domain patterns on the two heating portions of

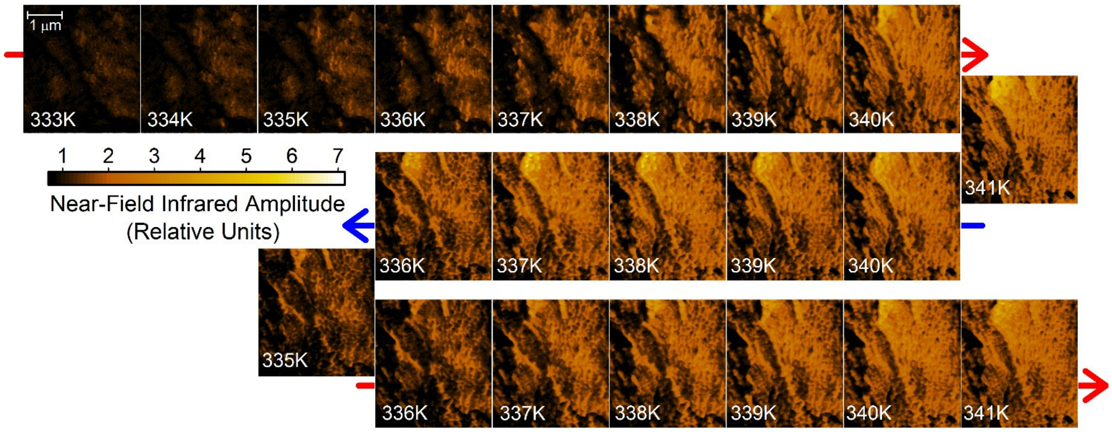

Figure 6.2 — Near-field infrared amplitude images are obtained during a non-monotonic temperature cycle through the phase coexistence regime. Arrows denote either heating (red) or cooling (blue). The near-field infrared amplitude is normalized to that of the insulating phase in each image. The area scanned here is different from the one shown in Figure 6.1.

the cycle are quite different. Hence, it is not necessary to exit the coexistence regime regime to reset the memory of the system.

We emphasize that nucleation occurs at precisely the same location in each uni-directional, monotonic temperature excursion across the MIT (See Fig. 6.3 b,c,d, and e). As the sample temperature crosses the equilibrium temperature, where the free energies of both phases are equal, it is thermodynamically preferred to form a domain ($\Delta G_{\mathrm{Domain}}<0$). Kinetically, however, the always positive strain and interfacial free energy terms oppose the formation of domains below a critical size (r*). Thus, any new domain must pass (tunnel) through the nucleation barrier (ΔG^*). This tunneling is an inherently stochastic process. Nucleation occurs at each site in a given time interval with a probability (P_N) proportional to $e^{-\Delta G^*_{local}/k_B T}$ (See Fig 6.3h)[157]. In contrast to homogeneous nucleation, which

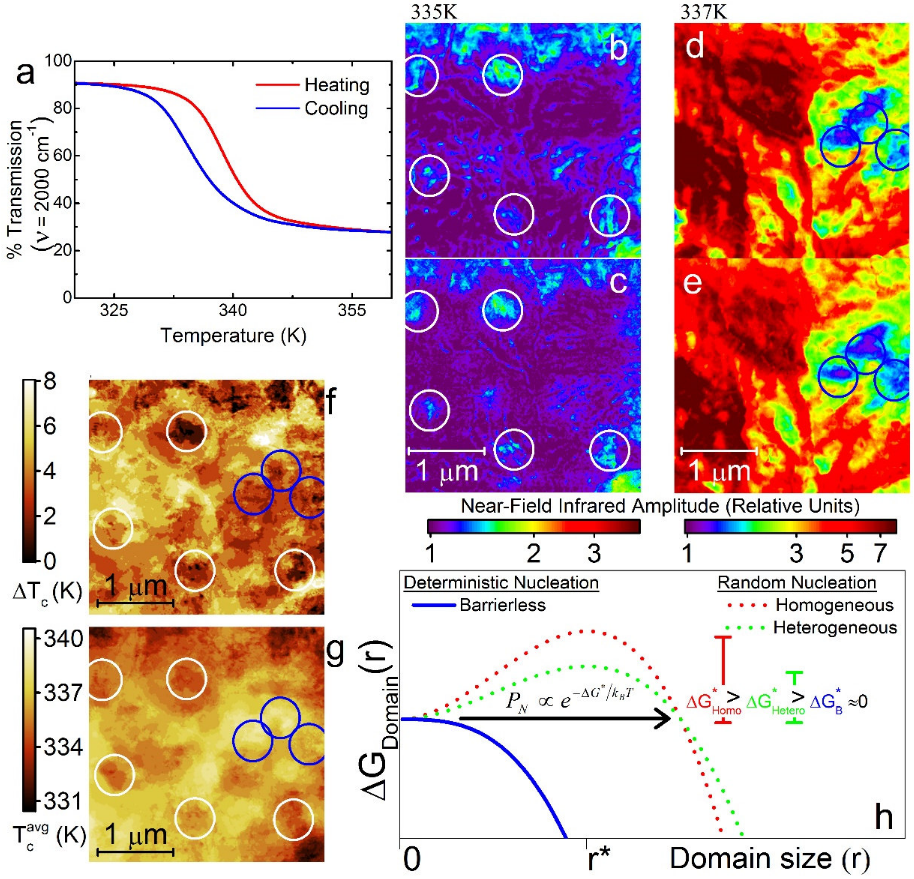

Figure 6.3 — a, Macroscopic thermal hysteresis loop measured via infrared transmission through the film-substrate system. b,c,d,e s-SNIM images demonstrating the nucleation sites on heating (b and c), and cooling (d and e) of the same area as shown in Fig. 6.1. f and g, Local hysteresis width (ΔT_c) and local phase equilibrium temperature (T_c^{avg}) respectively for the area shown in b,c,d,e. White (blue) circles in b,c,d,e,f,g serve to guide the eye to some of the nucleation sites which occur on heating (cooling). h, Schematic of the free energy landscape for a domain of characteristic linear dimension r for different types of nucleation sites. Note that here we make the distinction between heterogeneous nucleation and "barrierless nucleation". Barrierless nucleation is a special case of heterogeneous nucleation where, unlike the more general case, the nucleation barrier is completely removed, and nucleation thus occurs deterministically.

occurs in the homogeneous bulk, heterogeneous nucleation occurs at some inhomogeneity such as a defect or grain boundary. In heterogeneous nucleation, the size, shape and free energy of forming the critical nucleus can be altered significantly thereby reducing the barrier to nucleation. Nevertheless, as long as a barrier to nucleation exists, the process is inherently stochastic. In the analysis and discussion that follows, we explain that the highly reproducible patterns observed here are due to barrierless nucleation, and deduce qualitative features of the phase transition kinetics.

Quenched disorder locally alters the free energy balance between the phases[158]. As a result, the *local* temperature where the free energy of both phases is equal $\left(T_{eq}^{local}\right)$ is shifted from the bulk value. As neither phase is thermodynamically preferred at this temperature, some degree of superheating or undercooling is in general necessary to overcome the nucleation barrier. It is natural to consider an elementary (local) hysteresis loop, where each pixel has both a heating and cooling transition temperature. Equivalently, each pixel has a hysteresis width (ΔT_c) and an average of the cooling and heating transition temperature (T_c^{avg}). The latter is essentially a measure of T_{eq}^{local}, if one assumes that the local degree of undercooling and overheating is the same $(\frac{1}{2}\Delta T_c)$. In contrast, ΔT_c is related to the local nucleation barrier. While one could consider a more complicated model, which includes interactions such as strain between domains[159], the re-emergence of the same 341K pattern from different histories (Fig. 6.2) indicates that the simpler model is sufficient.

We note that nucleation occurs at sites where the local $\Delta \mathrm{T_c}$ is suppressed (See Fig 6.3f), which confirms that the nucleation barrier is greatly reduced, if not completely removed, at these sites. At such a site, the MIT can proceed along a barrierless path, and hence occurs completely deterministically (see Fig. 3h). As one might expect, on heating, nucleation occurs where the local equilibrium temperature (T_c^{avg}) is relatively low. Conversely, on cooling, nucleation occurs where T_c^{avg} is relatively high (See Fig. 6.3 b,c,d,e,f and g). Note that to determine the local transition temperatures used in Fig. 6.3, we employ a threshold of 1.45 for the normalized infrared amplitude, above which the pixel is considered to be metallic. We define the local transition temperature as the temperature where the signal first crosses the threshold for both the heating and cooling directions. The observed local characteristics (See Fig. 6.3 f and g) – and thus our conclusions – do not change appreciably for a broad range of reasonable thresholds. Appropriate thresholds are those that exceed the topography induced contrast, but are still low enough to capture the subtle contrast near nucleation.

Both ΔT_c and T_c^{avg} contribute to the shape of the thermal hysteresis loop observed in macroscopic measurements of the MIT. Inhomogeneity in T_c^{avg} can prevent the propagation of the new phase, resulting in a broader transition ≈ 15 K in width as seen in the infrared transmission measurement (Fig. 3a). The variation observed on the microscopic scale is ≈ 9 K and is attributed to the finite field of view of the s-SNIM images. In contrast, macroscopic VO_2 single crystals have very sharp transitions, and don't exhibit phase coexistence unless subject to external strain[8,40,105,106,160]. In such crystals, the hysteresis width width is set by the smallest local ΔT_c.

Interestingly, several authors have reported that there is a correlation between the size of VO_2 single crystals and the width of the hysteresis. It is found that the width of the hysteresis of the MIT can be increased greatly, to as much as 35 K for single domain VO_2 nano-particles[161,162]. The hysteresis width is systematically lessened in nano-particles with increasing size and number of grain boundaries[162]. This trend holds for free-standing VO_2 crystals, from the somewhat larger VO_2 "nanorods"[163] - which have a hysteresis width of approximately 5 K - to millimeter scale free-standing VO_2 crystals which have hysteresis widths of approximately 2 K[102]. A small single domain VO_2 nanoparticle is quite likely to not contain a barrierless nucleation site. The huge hysteresis width observed in these crystallites is a clear indication that the nucleation barrier at other sites is so large that these stochastic nucleation processes occur rarely. In contrast, nucleation is *functionally deterministic* in sputtered VO_2 films: nucleation occurs reliably - only at the barrierless sites - each time the temperature crosses T_{eq}^{local}.

Note that in contrast with the extremely large hysteresis observed in isolated nanocrystallites, *films* of very small VO_2 particles (<<100 nm) can have very if not negligible hysteresis widths (See Fig. 6.4)[164]. Although this seems contradictory, these two situations are in some sense polar opposites. While isolated nanocrystallites have minimal nucleation sites, films such particles have a an extreme density of grain boundaries and the associated dislocations, defects, complex geometry, etc. which are likely candidates for nucleation sites. Note that the s-SNIM images strongly suggest that grain boundaries do not necessarily stop the growth of phase domains. It is thus not necessary for each grain in the nano-particle film to contain a nucleation site.

The qualitative characteristics of macroscopic hysteresis loops (See Fig. 6.4) can be explained in terms of the availability of nucleation sites and the crystallinity/homogeneity of the sample. The sharpness of the transition is determined by the crystallinity/homogeneity of the sample. Domains can only form in regions where the temperature is above (below) the average T_c^{local} on heating (cooling). In such a region, superheating (undercooling) occurs unless the region contains a nucleation cite. Where the nucleation sites are sparse, such as nanocrystallites or a polycrystalline film such as the one studied here,

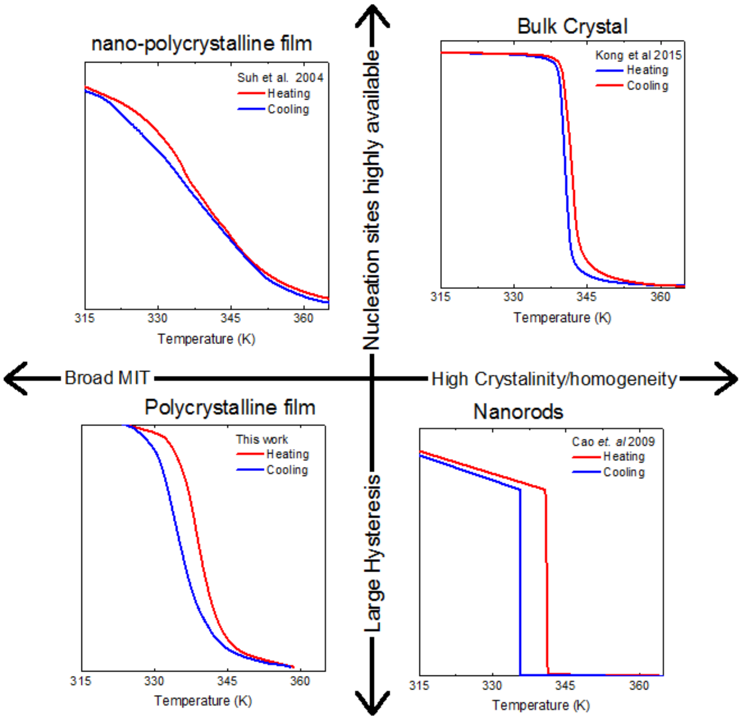

Figure 6.4 – Effects of crystallinity and availability of nucleation sites on the macroscopic hysteresis loop.

the hysteresis effect can be considerable. In cases where nucleation sites are readily readily available, the hysteresis is much smaller.

It is evident that the multi-grain structure of the sputtered VO_2 film is essential to deterministic behavior, as some evidence of randomness has been seen previously in VO_2 samples without grain boundaries. Dramatic spontaneous symmetry breaking has been attributed to the structural phase transition accompanying the MIT in a particularly clean VO_2 film[150]. Furthermore, differences in the metal-insulator domain pattern was reported on cooling VO_2 nanorod crystals[97]. There is experimental evidence that grain boundaries play a role in nucleation[149,162] but we cannot rule out other factors, perhaps below the length scale of our measurement, that may be necessary to create a nucleation site. One such which has been suggested previously via DFT+U calculations, is an oxygen at a grain boundary[162]. Quite possibly, a critical concentration of oxygen vacancies per unit volume is required for nucleation.

6.4 CONCLUSIONS

To conclude, we have shown that the phase domain patterns which form during the thermally driven MIT in a VO_2 film can behave in a completely deterministic way. It is clear from the present result that quenched disorder can be used to reliably control the spatial distribution of phase domains. Interestingly, nanoscale inhomogeneity in the ultra-fast optically driven MIT[97,164] suggests that our conclusion can be generalized to the MIT driven by optical pulses and also by a dc electric field. Our work provides the motivation for further meaningful exploration into reliable nanoscale VO_2 electronic and photonic devices.

Chapter 7

Conclusions and outlook

At long last, we can state with confidence that the insulating phases of VO_2 are Mott-Hubbard insulators. One should acknowledge that while such bold claims have been made before, in a number of directions, they have ultimately not lead to broad consensus in the field. Towards this end, it is worth reiterating that the insulating phases are now quite well characterized and the physical reality is quite clear:

1.) Coulomb repulsion (the Hubbard U) in the a_{1g} band is the dominant contributor to the quantitative details of the band structure. That the band structure effects (t and t') are small is established here, as the M_2 to T phase transition studied in Chapter 3 has negligible effect on the band structure. That the electronic structure observed here is remarkably similar to the previous work on the M_1 phase[21–25], and that the transtition between the

M_1 and T phases is continuous, enables this conclusion to be extended to the three known insulating phases: M_1, M_2, and T. When the insulating behavior arises primarily from intra-atomic Coulomb repulsion, such an insulator is classified as Mott-Hubbard type.

2.) The dimerized chains are somewhat unconventional Mott-Hubbard insulators in that the valence electrons form singlet pairs, revealed by NMR[7] and EPR[55,104], which are localized on the vanadium dimers as opposed to the more conventional situation where electrons are localized to individual atoms. The localized electrons on the undimerized vanadium ions in the M_2 phase represent a more conventional Mott-Hubbard scenario [7].

In truth, this picture was quite appealing following the work of Pouget *et al.* in 1974[7]. The inability of the single particle band theory (LDA) calculations in 1994 to open an energy gap made the necessity of electronic correlations abundantly clear[45]. However, there has been some ambiguity in the recent theoretical works. Moreover, the interpretation of recent experimental results has been highly model-dependent and ultimately ambiguous. The conclusive experimental verification in our work that the insulating phases are firmly in the Mott-Hubbard limit represents a significant milestone in the study of this material. This insight removes the previous ambiguity, and ultimately permits a re-interpretation of these and other results within a clear and consistent framework.

There is a subtlety that bears particular clarification. That the quantitative value of U in the a_{1g} band is strongly affected by the occupation of the e_g^π band – through screening – is strongly suggested by the results presented in Chapter 5. This is in line with the photoemission experiments[21,25] and the qualitative theoretical description presented early on by Mott[18]. In the insulating phases – where the e_g^π band is empty – the screening, and thus the value of U, should be insensitive to slight changes in lattice structures. However, fine details in the lattice structure might be expected to have significant consequences when the a_{1g} and e_g^π bands both cross the Fermi energy, as in this situation their relative occupancies - and thus the effective U - can vary. It is important to note that this sort of sensitivity to lattice structure is not a Peierls effect. It is instead a more subtle effect that involves the interaction of the lattice with the electronic correlations. Further work in this regime, either in the rutile phases or the monoclinic metal phase(s), is necessary to provide additional insight into this effect and the kinetics of the MIT.

In terms of the larger correlated electron problem, VO_2 has a critical role to play. Ultimately, the goal from the computational side of the field is to develop models with predictive power. VO_2 is an ideal proving ground for such models due to the relatively simple unit cell, multiple distinct phases, and high sensitivity to external parameters such as strain. The role of experiment towards this goal going forward will be to fully characterize the material – including the novel phases - in order to fully test and constrain these models. More practically, such an extensive characterization is a necessary step towards harnessing VO_2 for applications.

Certainly, the most exciting potential applications of VO_2 and other correlated materials are on the nanoscale. The potential of these materials for application is dependent on their novel phase transitions. That random domain formation on the nanoscale is not necessarily intrinsic to these phase transitions is something of an unexpected boon (See Chapter 6). However, further work is necessary to discover the ultimate cause. Insights gained through such work could potentially be leveraged in nanoscale devices across correlated systems.

In conclusion, the great debate should be considered put to rest. However, the potential and depth of the VO_2 system is in no way diminished with the conclusion of the great debate. It remains a fertile ground for experimental and theoretical investigations into strong correlations in condensed matter systems. For one, the rutile metal itself is hardly the simple uncorrelated metal it was thought to be at the outset. Moreover, the nature of the more exotic phases such as the monoclinic metal is entirely unclear. The insight gained through solving this classic problem will serve as an invaluable tool in addressing the outstanding questions in VO_2 and other strongly correlated systems.

Appendix A

Modeling of experimental data for determining optical constants presented in Chapter 3

A.1 SPOTSIZE CORRECTION

It is necessary to account for the fact that, at long wavelengths, the microscope spot size is larger than the crystal (See Fig. A.1). It is natural to model this situation in the following way.

$$T_{Eff} = F(\nu)T_{VO_2+Sub} + (1 - F(\nu))T_{Sub}$$

Where *F(ν)* is the percentage of light first incident on the VO_2 at a given frequency, T_{VO_2+Sub} is the absolute transmission through the VO_2 and substrate, and T_{Sub} is the absolute transmission through the substrate. $\frac{T_{Eff}}{T_{Sub}}$ is the data that was actually measured. $\frac{T_{Eff}}{T_{Sub}}$ is equivalent to $\frac{T_{VO_2+Sub}}{T_{Sub}}$ at higher frequencies, when all of the light is falling on the crystal At low frequencies it is necessary to use $F(\nu)$ to extract $\frac{T_{VO_2+Sub}}{T_{Sub}}$ from $\frac{T_{Eff}}{T_{Sub}}$, as $\frac{T_{VO_2+Sub}}{T_{Sub}}$ is the real data of interest.

The size and shape of the sample and the spot are the same between the two phases. Thus, $F(\nu)$ is the same for all phases and polarizations. This assumes that the transmission is a simple geometric sum of the infrared light passing through the crystal and that passing through the area around it. This ignores potential scattering and plasmonic effects due to the material's polarizability and shape. The lack of any strong dispersive features in the transmission spectra supports the notion that scattering and plasmonic effects are not significant.

Because of the complex shape of the measured crystal, and the presence of surrounding crystals of different thicknesses, *F(ν)* cannot be calculated precisely. The error bars in Fig. 3.4 are due to this uncertainty. The known rutile *dc* conductivity along c_R, the known spot profile of the objective, and the size of the measured microcrystal, were used

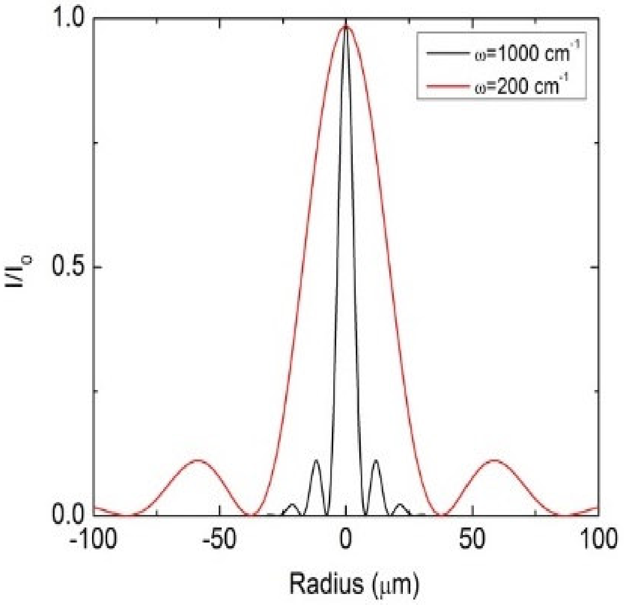

Figure A.1 — Intensity profile of a 0.58 NA Schwarzschild objective at two representative frequencies.

to constrain *F(ν)*. For a 0.58 NA Schwarzschild objective, the spot size starts to exceed 50 microns at 1000 cm^{-1} (See Fig. A.1) and becomes larger than the size of the crystal. Thus, we used an *F(ν)* equal to 1 above 1000 cm^{-1}. In the low frequency limit, the transmission through a film depends only on the *dc* conductivity[52]. The *dc* conductivity along c_r for nano-rods is known to be 2000 $\Omega^{-1}cm^{-1}$ [40]. To make the measured data consistent with this constraint, *F(ν)* must be 0.77 at 200 cm^{-1}. The intermediate values of *F(ν)* were then interpolated with a parabolic curve connecting the two constraining points at 200 cm^{-1} and 1000 cm^{-1}, with the vertex of the parabola at (ν =1000 cm^{-1}, F(ν)=1).

If the *dc* conductivity constraint is lifted, *F(ν)* is still constrained in that it must return a positive transmission in rutile VO_2. This sets a lower limit on *F(ν)* at 200 cm^{-1}; *F(*200 cm^{-1}*)* must be greater than 0.68. However, this would yield a very large $\sigma_1(\nu)$ in the *dc* limit. A more reasonable lower limit for *F(*200 cm^{-1}*)* of 0.72 was considered as it yields a *dc* conductivity along c_r of 3000 $\Omega^{-1}cm^{-1}$, 50% larger than that measured by Ref. [40].

Finite element analysis was used to check the reliability of the *F(ν)* values. The optical image of the sample was discretized, and *F(ν)* was calculated numerically using the following formula.

$$F(\nu) = \frac{\int_{microcrystal} I(\nu, x, y)dxdy}{\int_{All\ Space} I(\nu, x, y)dxdy} \qquad \text{A.1}$$

Where $I(\nu\ x, y)$ is the intensity of the spot at a given position for a specific frequency. While the different thicknesses of the surrounding crystals make an exact calculation of $F(\nu)$ impossible, it is useful in that it can establish an upper limit on $F(200\ \mathrm{cm}^{-1})$. We note that the surrounding crystals are much thicker than the crystal being measured and therefore contribute an insignificant amount to the measured transmission spectra.

A spatial aperture was used during the experiment to "apodize" the canonical Schwarzchild intensity distributions shown in Fig. A.1, reducing the intensity in the higher order rings at the cost of increased width of the central maximum[68], thereby ensuring that the crystal being measured contributes overwhelmingly to the transmission spectra at the expense of the surrounding crystals. Thus, in actuality, $F(200\ \mathrm{cm}^{-1})$ will be greater than what would be implied by the intensity distributions in Fig. A.1. Supposing that all of the light falls within the first order minima, finite element analysis yields an $F(200\ \mathrm{cm}^{-1})$ of 0.97. Likewise, assuming that all of the light falls within the second order minima yields an $F(200\ \mathrm{cm}^{-1})$ of 0.63. While 0.97 is unreasonably high, and 0.63 is less than the physical limit of 0.68 discussed above, averaging these values and adding an extra 5% provides a reasonable upper limit on $F($200 cm$^{-1})$ of 0.85. Figure A.2 shows the uncertainty in the optical constants due to the uncertainty in $F(\nu)$ using the above considerations to bound $F(200\ cm^{-1})$ between 0.72 and 0.85.

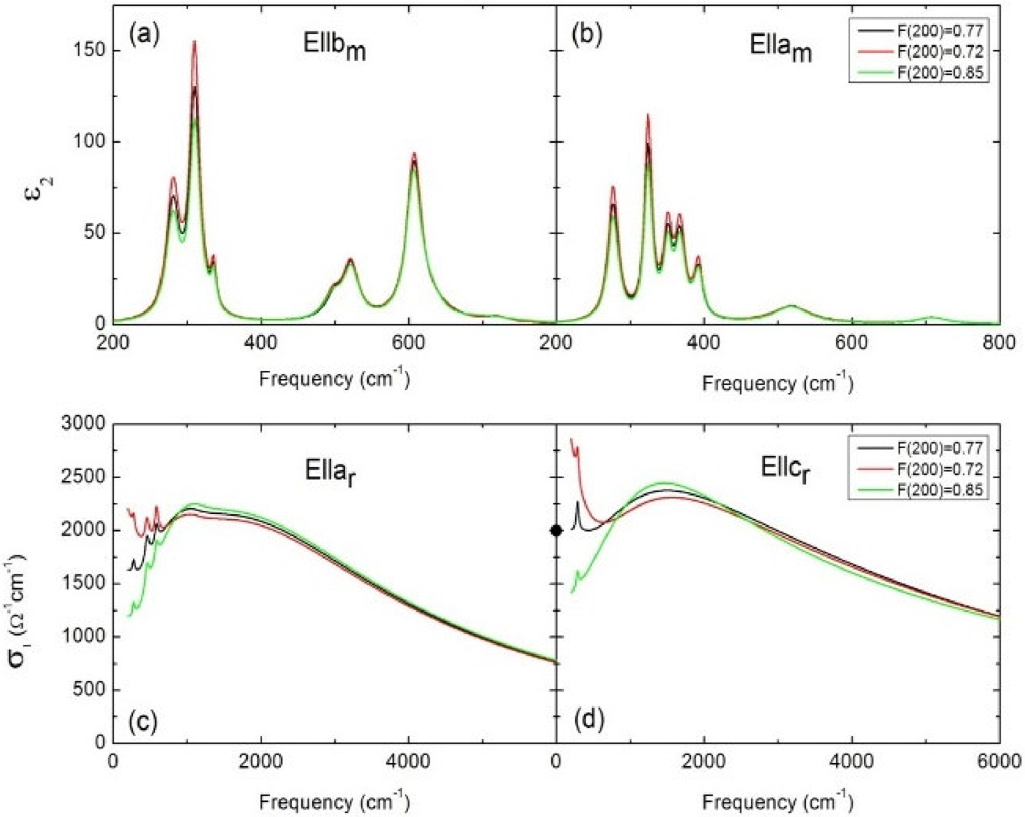

Figure A.2 — The uncertainty caused by the spread in F(ν) for monoclinic (M_1) VO_2 (a) and (b), and rutile VO_2 (c) and (d). Black curves show the optical constants consistent with the rutile c_r axis dc conductivity constraint (black circle). Red curves show the optical constants using the lower limit on F(200 cm^{-1}). Green curves show the optical constants using the upper limit on F(200 cm^{-1}).

A.2 SPECTRA AND FITS

The normalized transmission spectra were modeled using WVASE 32, spectroscopic analysis software from J.A. Woollam Co. The microscope objective leads to a range of angles of incidence from 15 degrees to 35 degrees. The angle of incidence was modeled as 25 degrees. As the variance in the modeled transmission between angles of incidence between 15 and 35 degrees is less than 1%, this approximation has a negligibly small effect on the modeling. Spectra and fits are shown in Fig. A.3.

The rutile transmission spectra in the phonon region warrant special comment. The phonon features in the rutile phase spectra are much weaker than those of the monoclinic M_1 phase. However, there are four reproducible features above our noise level, one when $\vec{E}//c_R$, and three when $\vec{E}//a_R$. Fig. A.3 (e) and (f) show the data, and the generated transmission with the phonon oscillators (grey) and without the phonon oscillators (red) present in the model. It is clear that while the features are weak, the phonon oscillators are necessary to achieve an acceptable fit.

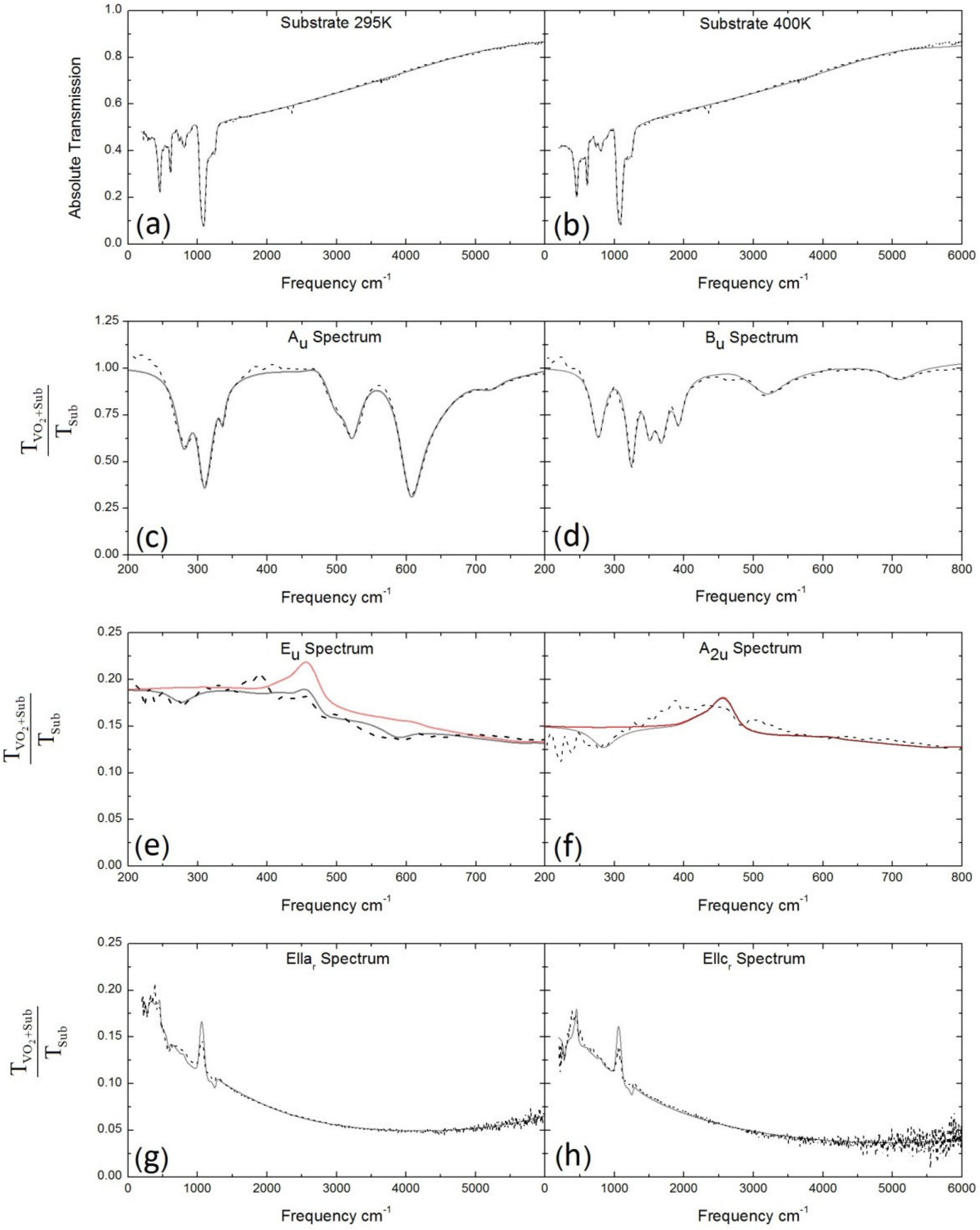

Figure A.3 — Representative spectra and fits for the substrate at (a) 295K and (b) 400K; monoclinic (M_1) VO_2 at 295K (c) and (d); and rutile VO_2 at 400K (e), (f), (g) and (h). Data are shown as dashed lines and fits are shown as solid lines. The red lines in (e) and (f) show the modeled transmission without the phonon oscillators. Data shown in (c), (d), (e), (f), (g) and (h) is consistent with $F(\nu)$ obtained from the rutile c_r axis dc conductivity constraint ($F(200\ cm^{-1})=0.77$).

Appendix B

Analytical details for the spectroscopy data presented in Chapter 4

B.1 GENERALIZED MICRO-ELLIPSOMETRY

The broadband optical constants reported in this work are extracted from the experimentally measured spectra using WVASE 32, a spectroscopic data analysis software from J.A. Woollam Co. The software generates experimental data from a “model” material with optical constants built up as a sum of Kramers-Kronig consistent oscillators. The parameters of the oscillators are then adjusted iteratively to achieve the best agreement with the experimental data.

Generalized (Jones matrix) spectroscopic ellipsometry was used in the near infrared, visible, and ultraviolet regions of the spectrum. Ellipsometry is a particularly powerful experimental technique in that, due to its self-referencing nature, it returns extremely reliable optical constants. Moreover, it enables the unambiguous determination of both the real and imaginary parts of the function, unlike reflectance or transmission alone. Due to the fact that the is Kramers-Kronig consistent, this benefit is extended into the entire spectrum, even regions, such as the far infrared in this work, where there is reflectance but no ellipsometry data available. This benefit is related to causality and the property of unique analytic continuation of the complex dielectric function.

Jones matrix ellipsometry is more general than the usual, isotropic form, in that it measures the cross conversion between p and s polarized light upon reflection from the sample. Cross conversion occurs when the dielectric tensor of the sample has non-zero off diagonal elements. Taking this cross conversion into account is necessary for anisotropic crystal structures, such as the insulating states of VO_2; the dielectric tensor for an absorbing monoclinic crystal has one independent off diagonal element, as shown below; there is no choice of coordinate system that will diagonalize the tensor. The dielectric tensor is complex symmetric, and the special "3" axis in the monoclinic is along the axis opposite the monoclinic angle.

$$\varepsilon_{Monocinic} = \begin{pmatrix} \varepsilon_{11} & \varepsilon_{12} & 0 \\ \varepsilon_{12} & \varepsilon_{22} & 0 \\ 0 & 0 & \varepsilon_{33} \end{pmatrix}$$

B.1

The triclinic case is, in general, even less symmetric. There are no zero elements guaranteed by symmetry.

$$\varepsilon_{Triclinic} = \begin{pmatrix} \varepsilon_{11} & \varepsilon_{12} & \varepsilon_{13} \\ \varepsilon_{12} & \varepsilon_{22} & \varepsilon_{23} \\ \varepsilon_{13} & \varepsilon_{23} & \varepsilon_{33} \end{pmatrix}$$

B.2

The simple Ψ and Δ parameters, which come from the diagonal elements of the Jones Matrix $\left(\Psi_{\frac{pp}{ss}}\ and\ \Delta_{\frac{pp}{ss}}\right)$, are shown in Fig. B.1 for when the sample is oriented with the vanadium chains parallel and perpendicular to the plane of incidence. Interestingly, in these orientations, there is hardly any structure in the off diagonal elements $\left(\Psi_{\frac{sp}{ss}}\ , \Delta_{\frac{sp}{ss}}\ , \Psi_{\frac{ps}{pp}}\ and\ \Delta_{\frac{ps}{pp}}\right)$ above the noise level. These off diagonal Jones matrix elements come from off diagonal elements of the dielectric tensor. That these off diagonal Jones matrix elements are small is characteristic of an optically uniaxially anisotropic crystal with an optical axis along the vanadium chains. Thus, we choose to model the data using a uniaxial model material for both the M_2 and Triclinic phases.

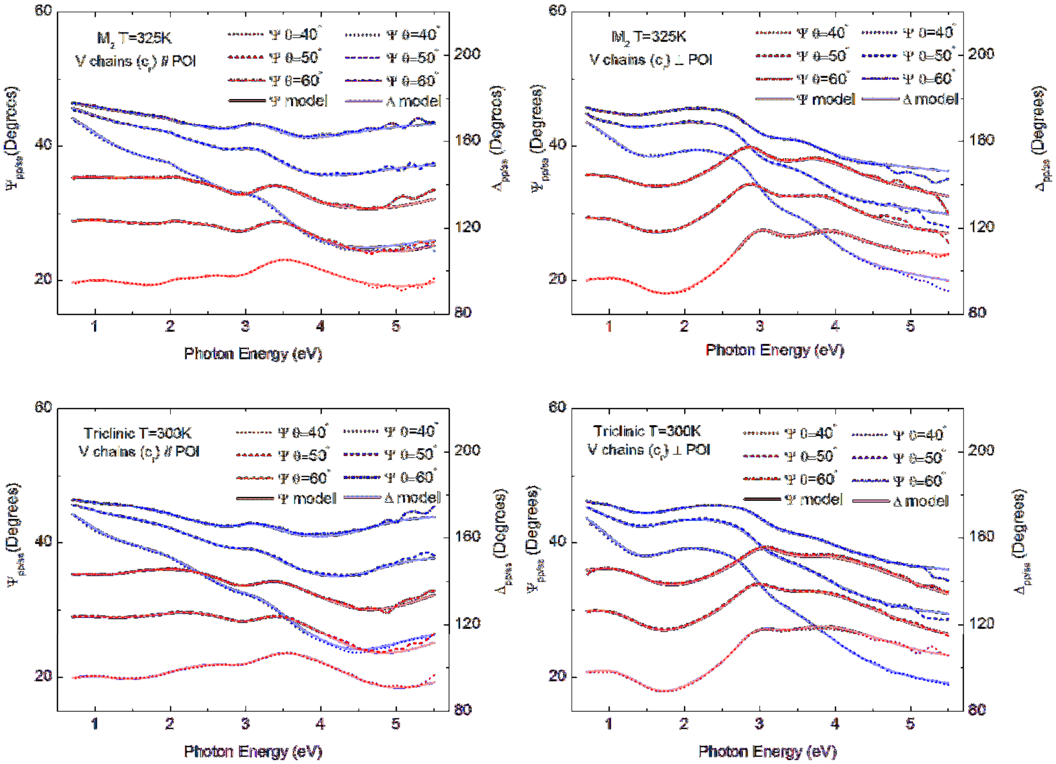

Figure B.1 — Generalized micro-ellipsometry spectra and fits showing the diagonal Ψ and Δ elements of the Jones matrix. Fitting is done using a uniaxial model in which the "V chains" (c_R) direction is the extraordinary ray.

$$\varepsilon_{T\ ,M_2} \approx \varepsilon_{uniaxial} = \begin{pmatrix} \varepsilon_{\perp\ V\ chains} & 0 & 0 \\ 0 & \varepsilon_{\perp\ V\ chains} & 0 \\ 0 & 0 & \varepsilon_{\parallel\ V\ chains} \end{pmatrix} \qquad \text{B.3}$$

Note that this uniaxial model is in no way inconsistent with the expected tensors. The experimental result, then, is simply that the off diagonal elements the dielectric tensor are too small to be measured in the present experiment, that $\varepsilon_{11} \approx \varepsilon_{22}$ for the M_2 and T phases of VO_2.

There are a number of good reasons to expect the uniaxial approximation to be reasonable. First, the insulating phases of VO_2 twin about the vanadium chains (c_R) direction when they cool from the higher symmetry rutile phase. This twinning would be expected to lead to some averaging of optical constants in the plane perpendicular to the c_R direction, and explains why we see don't see significant anisotropy in that plane($\varepsilon_{11} \approx \varepsilon_{22}$). Moreover, that $\varepsilon_{11} \approx \varepsilon_{22}$ is also consistent with our theoretical calculations, even for untwinned VO_2.

B.2 POLARIZED REFLECTANCE MICRO-SPECTROSCOPY

For the far and mid infrared regions of the spectrum, confocal reflectance microscopy is used to extract optical spectra with light polarized both parallel and perpendicular to the vanadium chains. Reflectance, as opposed to transmission, is necessary because the samples, even at thicknesses of around 60 μm, are opaque in the phonon region. This method is quite successful in determining the center frequencies of the phonons, and, where appropriate, separating modes of different symmetries. There is, however, some uncertainty in the absolute values for the following reasons. In the far infrared, the diffraction limited spot size begins to exceed the size of the crystal. Even for optical spectroscopic measurements on macroscopic samples, reflectance is quite sensitive to slight differences in alignment between the sample and reference. Confocal reflectance microscopy is even more sensitive to the alignment due to the fact that the light must pass through a very small aperture after reflection. To address these issues, we normalize to the metallic rutile phase, in a procedure analogous to that used in reflectance spectroscopy, where gold is evaporated in-situ onto the sample for the purpose normalization. Despite the procedure employed, there is, however, some systematic uncertainty in the reflectance spectra in the far infrared.

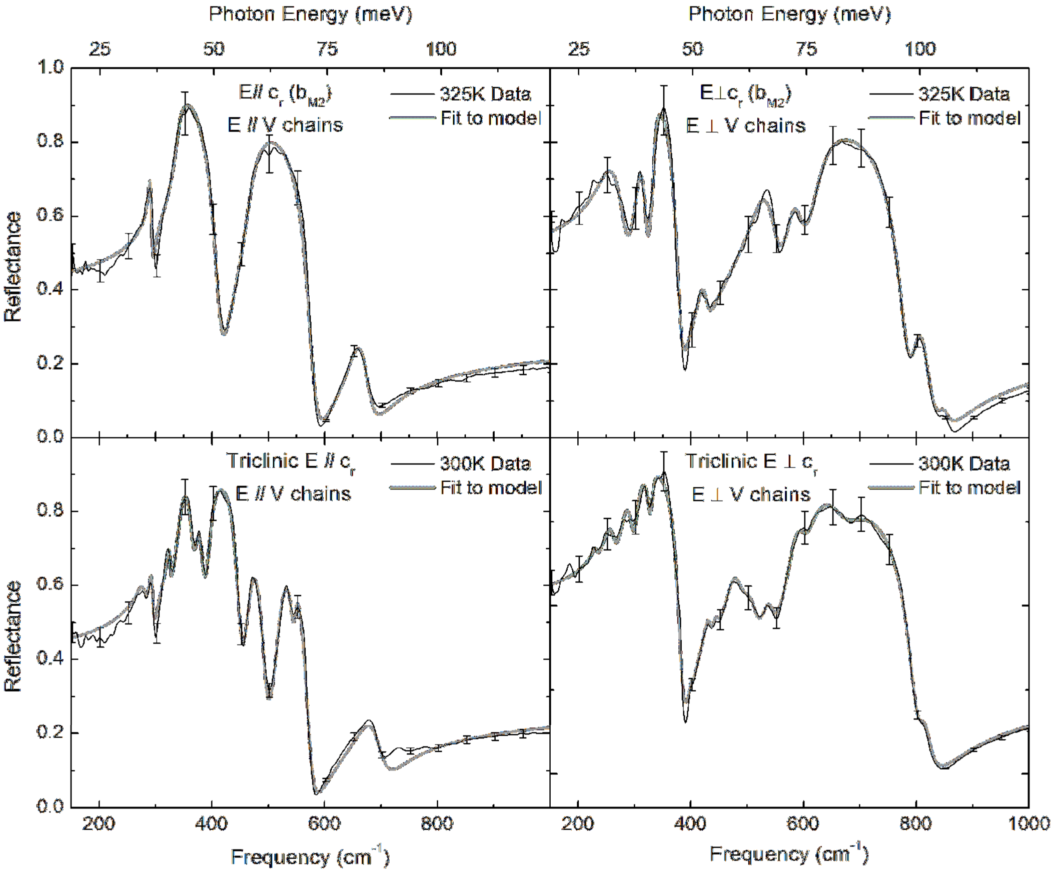

Figure B.2 — Reflectance spectra and Lorentzian oscillator fits in the phonon (far infrared) region. The error bars show systematic uncertainty due to the normalization procedure, alignment, and matching the two detector/polarizer spectral ranges used (see text). The uncertainties affect primarily the Lorentzian oscillator strengths and broadenings. However, this uncertainty in no way affects the structural assignment (see text).

The reflectance spectra and systematic error bars in the far infrared are shown in Fig. B.2. Their extent is determined by the discrepancy in the data sets acquired from the two detectors and polarizer combinations used in this work. The reported data is an equal weighting of the two data sets.

In the mid infrared reflectance spectra are shown in Fig. B.3. Most importantly, the mid-infrared reflectance agrees with the ellipsometry on the central point of the chapter, that there is negligible change between the M_2 and T phases across the phase transition. There is, however, some extra discrepancy between the model and the reflectance spectrum in this region. The black error bars are determined as in Fig. B.2, whereas the red error bars are accentuated by a factor of four. The larger red error bars are to account for the fact that the shorter wavelength mid infrared reflectance spectra are more affected by optical alignment and non-specular scattering. It is not uncommon, even on macroscopic samples, to have some disagreement between ellipsometry and reflectance in this region, because the two techniques are affected differently by non-specular scattering. In this region of the spectrum, it is appropriate to trust the ellipsometric data, due to its self-referencing nature. It should be noted that this mid-infrared region, between the IR active phonons and the lowest lying inter-band transition, contains no spectral features. The reflectance in this region is completely determined by the neighboring phonon and inter-band transition features at lower and higher energies, where the agreement between the raw spectroscopic data and the model is much better

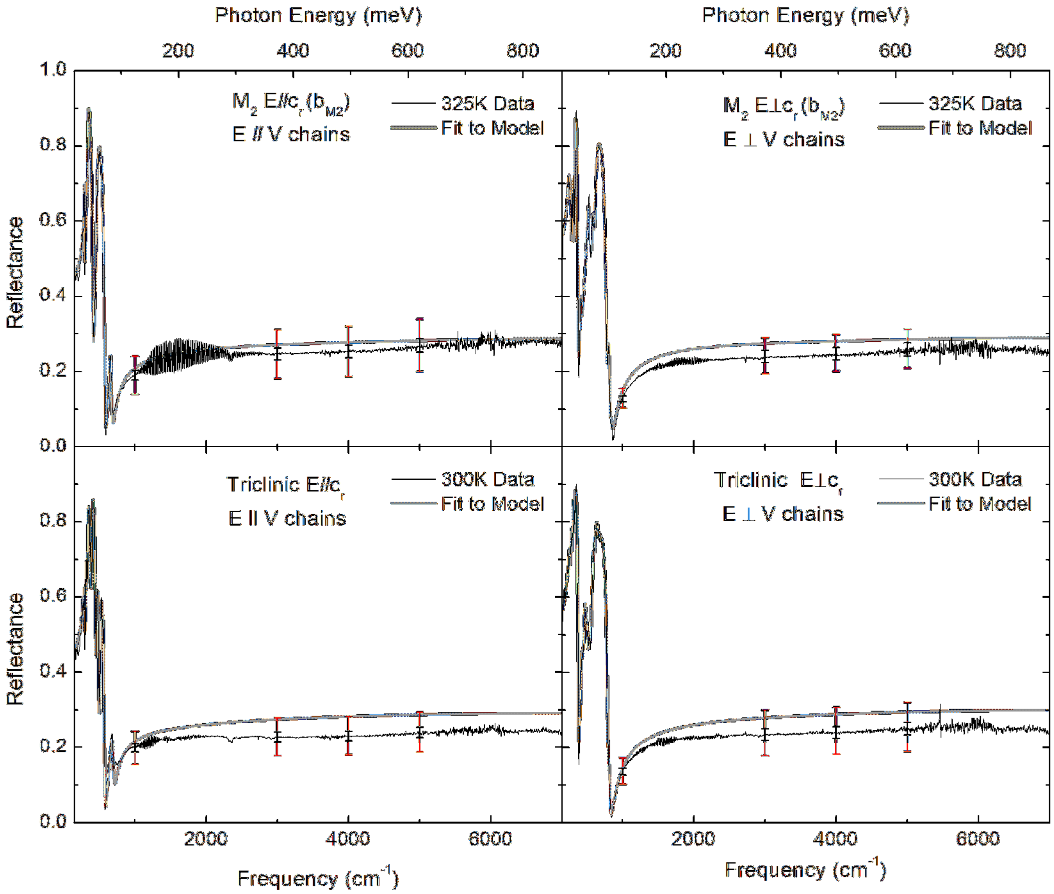

Figure B.3 — Reflectance micro-spectroscopy data and fits in the mid IR. The error bars are representative of systematic uncertainty caused by the normalization procedure, alignment, and matching the two detector/polarizer ranges. The black error bars are determined as in Fig. B.2, while the red error bars are accentuated by a factor of 4 (see text). While there is some uncertainty on the absolute values in this region, reflectance data agrees with the ellipsometry in that there is no significant change in the electronic contribution to either spectrum across the M_2 to T transition.

B.3 CONSTRAINING THE M1 REFLECTANCE SPECTRUM OF VERLEUR *ET AL.* [24].

There is a very large range of complex dielectric functions that will reproduce reproduce the reflectance intensity spectrum measured in [24] (See Fig. B.4). The The uncertainty is greatest near the high frequency edge of the spectrum, and is is due to the fact that phase information, i.e. the reflectance phase, is lost in an intensity spectrum. This phase information is preserved in ellipsometry, which unambiguously determines both the real (σ_1) and imaginary (σ_2) parts of the complex conductivity. It is not likely that the conductivity in the high energy region of the spectrum differs much between the M_1 and T phases, based on our theoretical results and the continuous nature of the phase transition. Certainly any changes should be expected to be considerably less than the uncertainty of Ref. [24]. Using the known complex conductivity of the T phase above 4 eV as a constraint, it is possible to fit the measured reflectance of the M_1 phase without any sacrifice to the quality of the fit (See Fig. B.4 (b)). With this constraint, the Kramers-Kronig consistent complex conductivity that we extract from the reflectance spectrum of Ref.[24] is essentially unique across the spectral range of the reflectance spectrum. This "constrained" conductivity should be thought of as a more accurate result from the experiment performed in Ref. [24]. The minor differences between the M_1 and M_2/T phases that remain after we apply this constraint (See main text) are likely due to systematic differences between the studies, and should thus not be attributed to intrinsic differences between the and M_2/T phases.

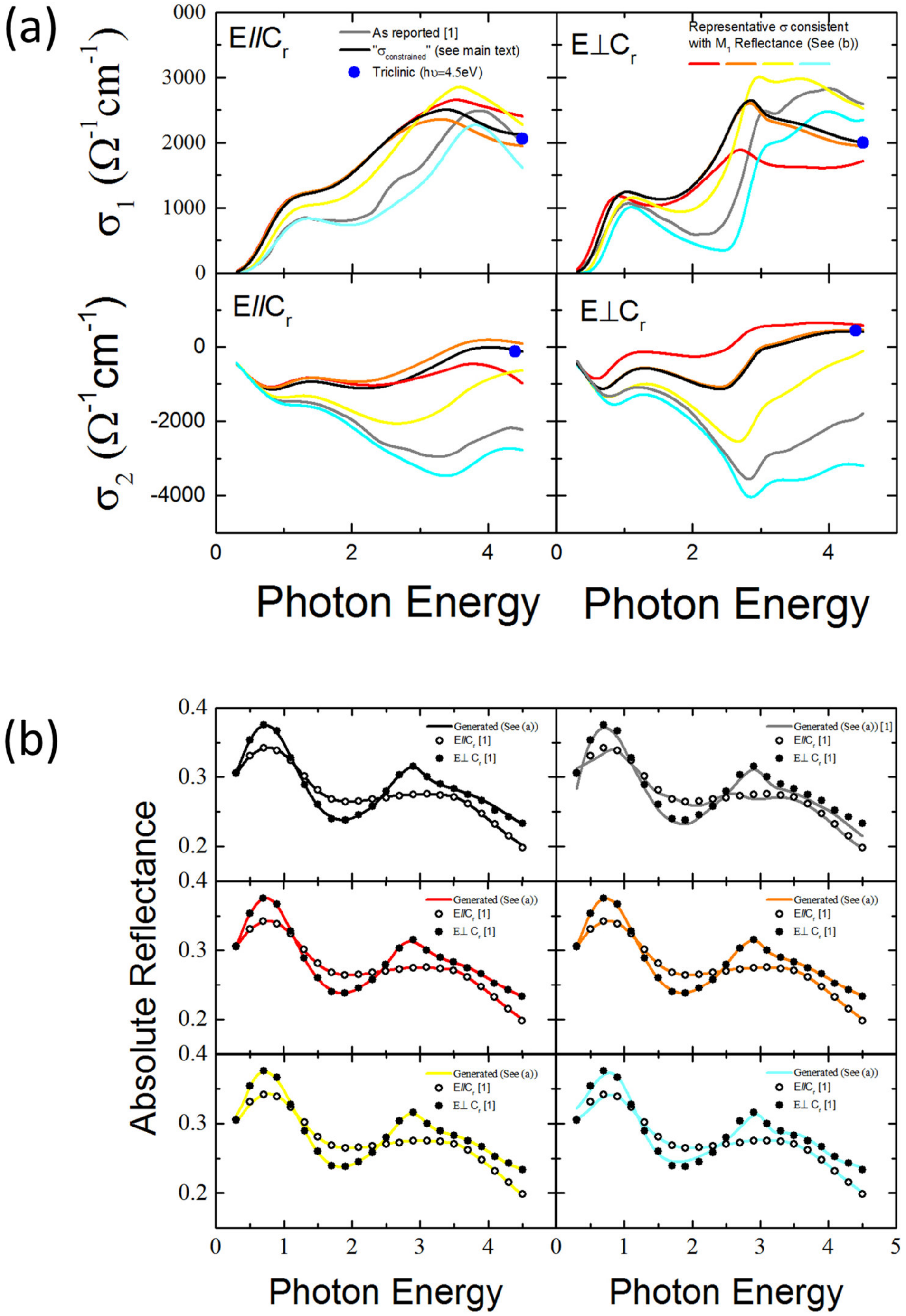

Figure B.4 — The complex conductivities shown in (a) are a representative sample of those that are consistent with the reflectance spectrum measured in [24] on M_1 VO_2. The measured reflectance for light polarized parallel (open circles) and perpendicular to C_r (closed circles) is shown in (b). In each panel of (b), the reflectance generated by one of the representative conductivities shown in (a), denoted by colors, is also shown. The complex conductivity of the T phase at 4.5eV (blue circles) is also shown in panel (a) for reference (see text).

Appendix C

Fits to the data for extracting optical constants discussed in Chapter 5

C.1 EXPERIMENTAL AND ANALYTICAL DETAILS

The measured spectra were modeled using WVASE 32, spectroscopic analysis software from J.A. Woollam Co. A model based on Kramers-Kronig consistent oscillators is created, and the software minimizes the error between the model-based spectrum and experimental spectrum. The VO_2 on quartz substrate system is modeled as three separate layers: the (001) quartz substrate with known optical constants, the VO_2 film whose optical constants are to determined, and an effective medium layer to model the surface roughness of the VO_2 film. The optical constants of quartz were first obtained with model-based fits to the experimental spectra acquired from a bare quartz substrate. The parameters related to the surface roughness were measured directly via an atomic force microscope (AFM). The AFM measurement yielded a RMS surface roughness of 3.7 nm and a 46.7% void fraction. Specifically, the surface roughness is modeled by a 7.4 nm thick effective medium layer with a 46.7% void fraction. The factor of two difference between the measured RMS roughness and the thickness of the effective medium layer is due to the nature of RMS averaging; i.e. the RMS value is ½ the peak to peak amplitude for a square waveform. The thickness of the film was accurately measured by grazing angle x-ray reflectivity with an uncertainty of about one percent. The ellipsometric and reflectance spectra and fits for the VO_2 on quartz film in both the rutile and monoclinic M_1 phase are shown in Figs. C.1, and C.2, respectively. Special comment is warranted for the reflectance data in the far infrared for the metallic phase. The slight downturn at lower frequencies in the reflectance data is evidence of the low lying peak in conductivity shown in the inset in Fig. C.1 (a); Drude oscillators alone are insufficient to fit this feature well.

The 300K reflectance data in the phonon region, shown in Fig. C.1 (d), contains significant contribution from both VO_2 and quartz phonons. Although the spectrum is dominated by quartz features, we clearly observe structure due to some

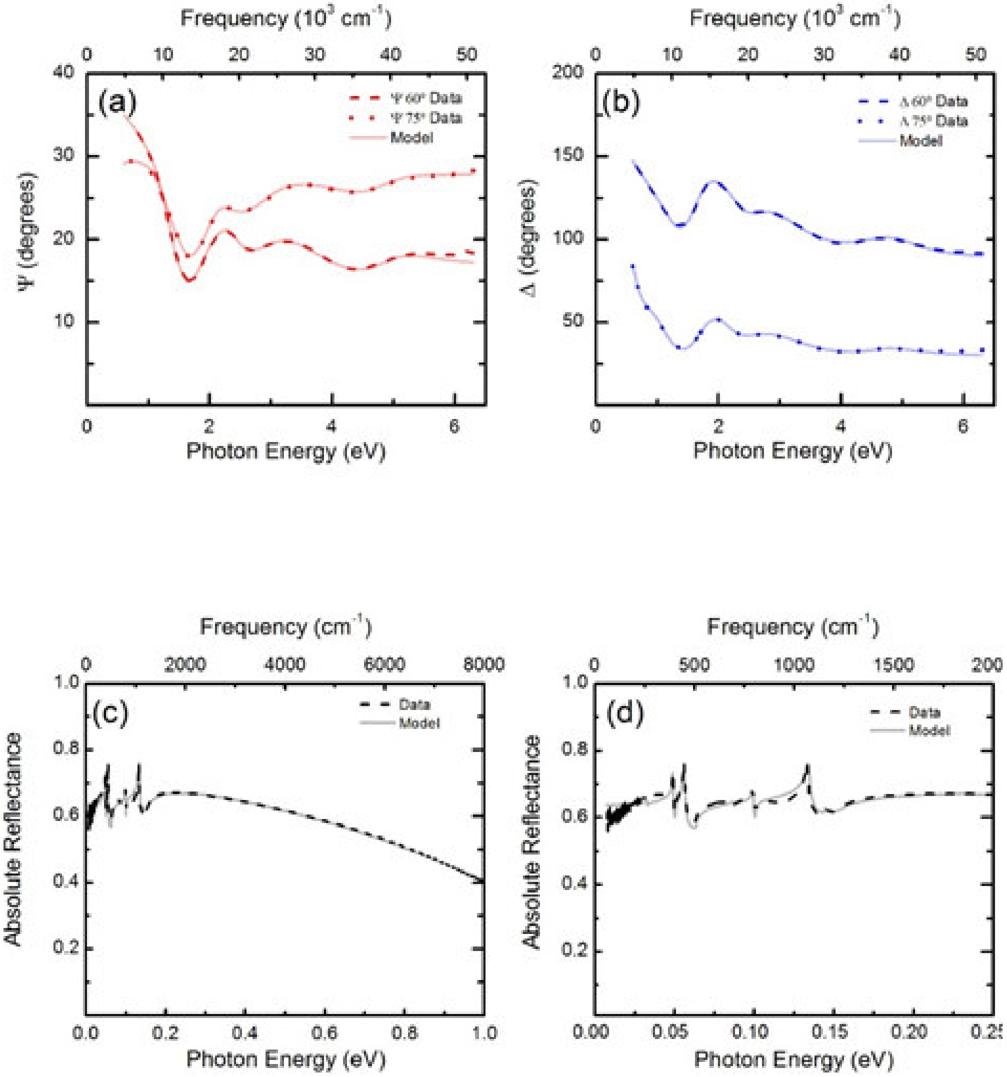

Figure C.1 — Optical spectra and modeled fits for the rutile phase of the VO_2 film on quartz at 360K. Spectroscopic ellipsometry data is shown in panels (a) and (b). The absolute reflectance spectrum is shown in panel (c) between 60 cm^{-1} and 8000 cm^{-1}. The absolute reflectance in the far infrared is shown in panel (d) from 60 cm^{-1} to 2000 cm^{-1}. The oscillations in the reflectance data at low frequencies are due to interference in the quartz substrate.

of the stronger VO_2 phonons. Moreover, the presence of the VO_2 phonon in the raw data is clearly demonstrated when one notes the poor fit to the data reflectance generated from a model with quartz phonons but no VO_2 phonons (Shown in Fig. C.1 (d) as a red line); the fit is significantly improved upon addition of VO_2 phonons to the model. Hence the reported VO_2 phonons are necessary to achieve an acceptable fit to the raw reflectance data.

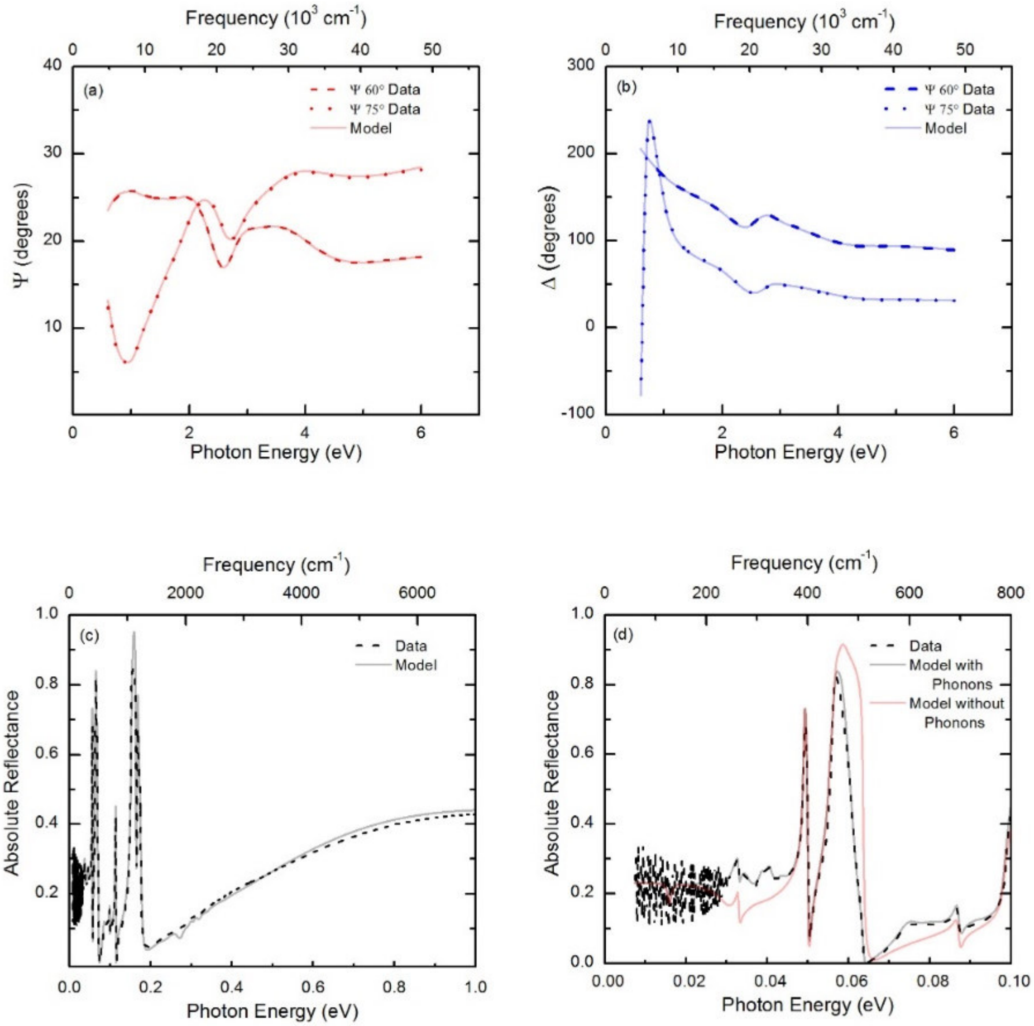

Figure C.2 — Optical spectra and fits for the monoclinic M_1 phase of the VO_2 film on quartz at 300K. Spectroscopic ellipsometry data is shown in panels (a) and (b). The absolute reflectance spectrum is shown in panel (c) between 60 cm^{-1} and 8000 cm^{-1}. The reflectance in the phonon region is shown in panel (d). The red line in panel (d), generated using a model for the VO_2 film on quartz with no VO_2 phonon features to demonstrate the clear need for the VO_2 phonons, in addition to the quartz phonons, to fit the measured spectra (See text). The VO_2 phonon at 189cm^{-1} is more clearly seen in transmission (not shown). The oscillations in the reflectance spectra are due to interference in the quartz substrate.

C.2 EVIDENCE OF STRUCTURAL TRANSITION

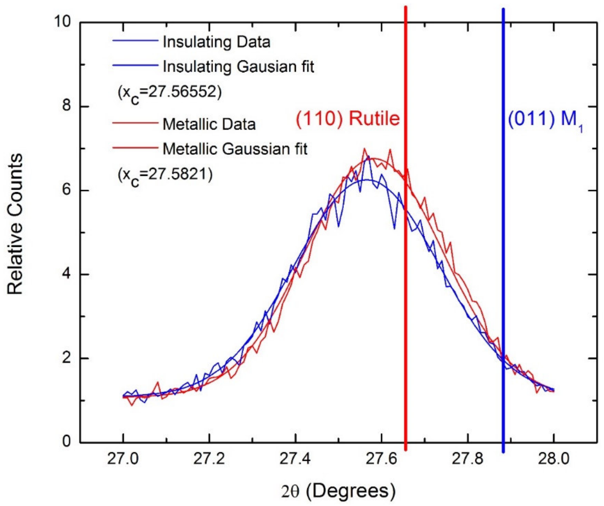

Figure C.3 - Shift in the Bragg peak across the phase transition. The vertical lines show the Bragg peak locations from the literature for bulk VO_2. This shift is consistent with the situation described in the main text. As the strain relaxes somewhat as the film transitions into the rutile phase, the diffraction peak shifts upwards towards the bulk rutile value.

Note that we can rule out the possibility that the metallic phase of VO_2 studied in this work is the exotic monoclinic metal seen by M.K. Liu *et al.*, that occurs without a structural transition to the rutile lattice[61]. Strong infrared phonons are expected to be present in the monoclinic metal as seen by M.K. Liu *et al.*[61].We do not observe any obvious infrared phonon features in the metallic phase which is fully consistent with a rutile metal. Moreover, our x-ray diffraction experiments confirm an upward shift in the Bragg peak position and an increase in its intensity, the

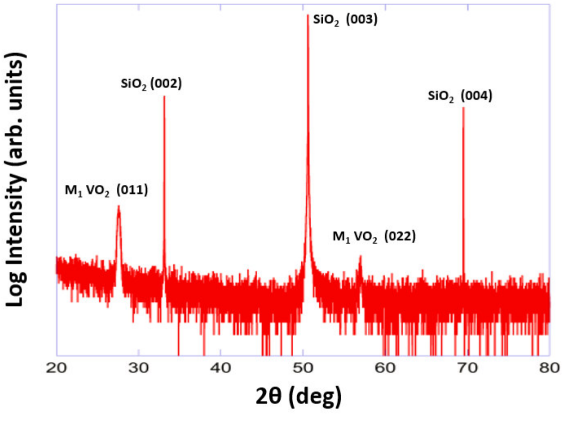

Figure C.4 — An XRD out of plane θ → 2θ scan of the VO_2 thin film and quartz substrate system. The M_1 VO_2 (011) and (022) peaks are clearly seen.

observations being consistent with a structural transition to the rutile lattice (See Fig. C.3).

In figure C.4, we show a broader 2ϑ x-ray diffraction scan in the insulating phase. The twins of the M_2 phase are expected to lead to a doublet in the vicinity of 2ϑ angle of 27.8° [165]. The lack of any observed doublet in the (011) and (022) M_1 VO_2 peaks in figure C.4 rules out the possibility of an M_2 insulating phase.

Bibliography

1. P. A. M. Dirac, Quantum Mechanics of Many-Electron Systems. *Proc. R. Soc. London. Ser. A, Contain. Pap. a Math. Phys. Character.* **123**, 714–733 (1929).
2. P. W. Anderson, More is Different - Broken Symmetry and Nature of Hierarchical Structure of Science. *Science (80-.).* **177**, 393 (1972).
3. F. J. Morin, Oxides which show a Metal-To-Insulator Transition at the Neel Temperature. *Phys. Rev. Lett.* **3**, 34–36 (1959).
4. A. H. Wilson, The Theory of Electronic Semi-Conductors. *Proc. R. Soc. London A Math. Phys. Eng. Sci.* **133**, 458–491 (1931).
5. N. F. Mott, The Transition to the Metallic State. *Philos. Mag.* **6**, 287–309 (1961).
6. J. B. Goodenough, Direct Cation--Cation Interactions in several Oxides. *Phys. Rev.* **117**, 1442–1451 (1960).
7. J. P. Pouget *et al.*, Dimerization of a Linear Heisenberg Chain in Insulating Phases of $V_{1-x}Cr_xO_2$. *Phys. Rev. B.* **10**, 1801–1815 (1974).
8. J. H. Park *et al.*, Measurement of a solid-state triple point at the metal-insulator transition in VO_2. *Nature.* **500**, 431–4 (2013).
9. J. P. Pouget, H. Launois, J. P. Dhaenens, P. Merenda, T. M. Rice, Electron Localization Induced by Uniaxial Stress in Pure VO_2. *Phys. Rev. Lett.* **35**, 873–875 (1975).
10. M. Ghedira, J. Chenavas, M. Marezio, Cation Disproportionation and Pairing in Insulating T-Phase of V0.985Al0.015O2. *J. Phys. C-Solid State Phys.* **10**, L309–L314 (1977).
11. D. B. Mcwhan, M. Marezio, J. P. Remeika, P. D. Dernier, X-Ray-Diffraction Study of Metallic VO_2. *Phys. Rev. B.* **10**, 490–495 (1974).
12. M. Marezio, Twinning in Cr doped VO_2. *Acta Crystallogr.* **29**, 618–621 (1973).
13. M. Marezio *et al.*, Structural aspects of the metal-insulator transitions in Cr-doped VO_2. *Phys. Rev. B.* **5**, 2541 (1972).
14. M. Ghedira, H. Vincent, M. Marezio, J. C. Launay, Structural Aspects of Metal-Insulator Transitions in $V_{0.985}Al_{0.015}O_2$. *J. Solid State Chem.* **22**, 423–438 (1977).

15. J. M. Longo, P. Kierkega, A Refinement of Structure of VO_2. *Acta Chem. Scand.* **24**, 420 (1970).

16. S. Westman, Note on a Phase Transition in VO_2. *Acta Chem. Scand.* **15**, 217 (1961).

17. J. B. Goodenough, *J. Solid State Chem.*, in press.

18. A. Zylbersztejn, N. F. Mott, A. Z. and N. F. Mott, Metal-Insulator Transition in Vanadium Dioxide. *Phys. Rev. B.* **11**, 4383–4395 (1975).

19. J. B. Goodenough, H. Y.-P. Hong, Structures and a Two-Band Model for the System. *Phys. Rev. B.* **8**, 1323–1331 (1973).

20. N. Mott, *Metal-Insulator Transitions* (Taylor & Francis, 1990).

21. T. C. Koethe *et al.*, Transfer of Spectral Weight and Symmetry across the Metal-Insulator Transition in VO_2. *Phys. Rev. Lett.* **97**, 116402 (2006).

22. K. Okazaki, S. Sugai, Y. Muraoka, Z. Hiroi, Metal-Insulator Transition in VO_2 Studied by Optical Spectroscopy. *AIP Conf. Proc.* **850**, 1229–1230 (2006).

23. M. M. Qazilbash *et al.*, Electrodynamics of the vanadium oxides VO_2 and V_2O_3. *Phys. Rev. B.* **77**, 115121 (2008).

24. H. W. Verleur, A. S. Barker, C. N. Berglund, Optical Properties of VO_2 between 0.25 and 5 eV. *Phys. Rev.* **172**, 788 (1968).

25. M. W. Haverkort *et al.*, Orbital-assisted metal-insulator transition in VO_2. *Phys. Rev. Lett.* **95**, 196404 (2005).

26. C. N. Berglund, H. J. Guggenheim, Electronic Properties of VO_2 near the Semiconductor-Metal Transition. *Phys. Rev.* **185**, 1022 (1969).

27. J. D. Budai *et al.*, Metallization of vanadium dioxide driven by large phonon entropy. *Nature.* **515**, 535–539 (2014).

28. E. I. Terukov, W. Reichelt, M. Wolf, H. Hemschik, H. Oppermann, Influence of Substitution of O-16 by O-18 in a Few Vanadium-Oxides on their Semiconductor-Metal Transition. *Phys. Status Solidi A-Applied Res.* **48**, 377–381 (1978).

29. J. R. Brews, Symmetry Considerations and Vanadium Dioxide Phase Transition. *Phys. Rev. B.* **1**, 2557 (1970).

30. A. Cavalleri, T. Dekorsy, H. H. W. Chong, J. C. Kieffer, R. W. Schoenlein, Evidence for a structurally-driven insulator-to-metal transition in VO_2: A view from the ultrafast timescale. *Phys. Rev. B.* **70**, 161102 (2004).

31. F. Gervais, W. Kress, Lattice-Dynamics of Oxides with Rutile Structure and Instabilities at the Metal-Semiconductor Phase-Transitions of NbO_2 and VO_2. *Phys. Rev. B.* **31**, 4809–4814 (1985).

32. H. Terauchi, J. B. Cohen, Diffuse X-Ray-Scattering due to Lattice

Instability Near Metal-Semiconductor Transition in VO_2. *Phys. Rev. B.* **17**, 2494–2496 (1978).

33. I. N. Goncharuk, A. V. Ilinskiy, O. E. Kvashenkina, E. B. Shadrin, Electron-electron correlations in Raman spectra of VO_2. *Phys. Solid State.* **55**, 164–174 (2013).

34. R. R. Andronenko, I. N. Goncharuk, V. Y. Davydov, F. A. Chudnovskii, E. B. Shadrin, Direct observation of the soft mode at a semiconductor-metal phase transition in vanadium dioxide. *Phys. Solid State.* **36**, 1136 (1994).

35. A. S. Barker, H. W. Verleur, H. J. Guggenheim, Infrared Optical Properties of Vanadium Dioxide Above and Below Transition Temperature. *Phys. Rev. Lett.* **17**, 1286 (1966).

36. T. J. Huffman *et al.*, Anisotropic infrared response of vanadium dioxide microcrystals. *Phys. Rev. B.* **87**, 115121 (2013).

37. R. Srivastava, L. L. Chase, Raman Spectrum of Semiconducting and Metallic VO_2. *Phys. Rev. Lett.* **27**, 727–730 (1971).

38. P. F. Bongers, Anisotropy of the Electrical Conductivity of VO_2 Single Crystals. *Solid State Commun.* **3**, 275–277 (1965).

39. S. Kittiwatanakul, J. Lu, S. A. Wolf, Transport Anisotropy of Epitaxial VO_2 Films near the Metal–Semiconductor Transition. *Appl. Phys. Express.* **4**, 91104 (2011).

40. J. Wei, Z. Wang, W. Chen, D. H. Cobden, New aspects of the metal-insulator transition in single-domain vanadium dioxide nanobeams. *Nat. Nanotechnol.* **4**, 420–424 (2009).

41. K. Kosuge, Phase Transition in VO_2. *J. Phys. Soc. Japan.* **22**, 551 (1967).

42. W. H. Rosevear, W. Paul, Hall-Effect in VO_2 Near Semiconductor-To-Metal Transition. *Phys. Rev. B.* **7**, 2109–2111 (1973).

43. J. C. Bonner, M. E. Fisher, Linear Magnetic Chains with Anisotropic Coupling. *Phys. Rev.* **135**, A640--A658 (1964).

44. J. P. D'Haenens, D. Kaplan, P. Merenda, Electron spin resonance in $V_{1-x}Cr_xO_2$. *J. Phys. C Solid State Phys.* **8**, 2267 (1975).

45. R. M. Wentzcovitch, W. W. Schulz, P. B. Allen, VO_2 - Peierls Or Mott-Hubbard - a View from Band Theory. *Phys. Rev. Lett.* **72**, 3389–3392 (1994).

46. V. Eyert, VO_2: A Novel View from Band Theory. *Phys. Rev. Lett.* **107**, 16401 (2011).

47. V. Ivady *et al.*, Theoretical unification of hybrid-DFT and DFT plus U methods for the treatment of localized orbitals. *Phys. Rev. B.* **90**, 1–13 (2014).

48. S. Biermann, A. Poteryaev, A. I. Lichtenstein, A. Georges, Dynamical

singlets and correlation-assisted peierls transition in VO_2. *Phys. Rev. Lett.* **94**, 26404 (2005).

49. J. M. Tomczak, S. Biermann, Effective band structure of correlated materials: the case of VO_2. *J. Phys. Condens. Matter.* **19**, 365206 (2007).

50. J. M. Tomczak, F. Aryasetiawan, S. Biermann, Effective bandstructure in the insulating phase versus strong dynamical correlations in metallic VO_2. *Phys. Rev. B - Condens. Matter Mater. Phys.* **78**, 1–6 (2008).

51. J. M. Tomczak, S. Biermann, Optical properties of correlated materials: Generalized Peierls approach and its application to VO_2. *Phys. Rev. B.* **80**, 85117 (2009).

52. B. Lazarovits, K. Kim, K. Haule, G. Kotliar, Effects of strain on the electronic structure of VO_2. *Phys. Rev. B.* **81**, 115117 (2010).

53. C. Weber *et al.*, Vanadium dioxide: A peierls-mott insulator stable against disorder. *Phys. Rev. Lett.* **108**, 256402 (2012).

54. W. H. Brito, M. C. O. Aguiar, K. Haule, G. Kotliar, Metal-Insulator Transition in VO_2: A DFT + DMFT Perspective. *Phys. Rev. Lett.* **117**, 56402 (2016).

55. J. P. Dhaenens, D. Kaplan, Tuchendl.J, Electron-Spin Resonance in Chromium Doped VO_2. *Solid State Commun.* **15**, 635–638 (1974).

56. C. Franchini, Hybrid functionals applied to perovskites. *J. Physics-Condensed Matter.* **26**, 235202 (2014).

57. J. M. Tomczak, S. Biermann, Materials design using correlated oxides: Optical properties of vanadium dioxide. *Epl.* **86**, 37004 (2009).

58. V. Ivady *et al.*, Theoretical unification of hybrid-DFT and DFT plus U methods for the treatment of localized orbitals. *Phys. Rev. B.* **90** (2014).

59. V. R. Morrison *et al.*, A photoinduced metal-like phase of monoclinic VO_2 revealed by ultrafast electron diffraction. *Science (80-.).* **346**, 445–448 (2014).

60. J. Nag, R. F. Haglund, E. Andrew Payzant, K. L. More, Non-congruence of thermally driven structural and electronic transitions in VO_2. *J. Appl. Phys.* **112** (2012).

61. M. K. Liu *et al.*, Anisotropic Electronic State via Spontaneous Phase Separation in Strained Vanadium Dioxide Films. *Phys. Rev. Lett.* **111**, 96602 (2013).

62. E. Arcangeletti *et al.*, Evidence of a pressure-induced metallization process in monoclinic VO_2. *Phys. Rev. Lett.* **98**, 196406 (2007).

63. L. Bai *et al.*, Pressure-induced phase transitions and metallization in VO_2. *Phys. Rev. B - Condens. Matter Mater. Phys.* **91**, 1–7 (2015).

64. K. Okazaki, S. Sugai, Y. Muraoka, Z. Hiroi, Role of electron-electron and electron-phonon interaction effects in the optical conductivity of VO_2. *Phys. Rev. B.* **73**, 165116 (2006).

65. Q. Gu, A. Falk, J. Wu, L. Ouyang, H. Park, Current-driven phase oscillation and domain-wall propagation in $W_xV_{1-x}O_2$ nanobeams. *Nano Lett.* **7**, 363–366 (2007).

66. B. S. Guiton, Q. Gu, A. L. Prieto, M. S. Gudiksen, H. Park, Single-crystalline vanadium dioxide nanowires with rectangular cross sections. *J. Am. Chem. Soc.* **127**, 498–499 (2005).

67. W.-T. Liu *et al.*, Intrinsic optical properties of vanadium dioxide near the insulator-metal transition. *Nano Lett.* **11**, 466–70 (2011).

68. G. L. Carr, Resolution limits for infrared microspectroscopy explored with synchrotron radiation. *Rev. Sci. Instrum.* **72**, 1613–1619 (2001).

69. W. Kohn, L. J. Sham, Self-Consistent Equations Including Exchange and Correlation Effects. *Phys. Rev.* **140**, 1133 (1965).

70. P. Giannozzi *et al.*, QUANTUM ESPRESSO: a modular and open-source software project for quantum simulations of materials. *J. Physics-Condensed Matter.* **21**, 395502 (2009).

71. V. I. Anisimov, J. Zaanen, O. K. Andersen, Band Theory and Mott Insulators - Hubbard-U Instead of Stoner-i. *Phys. Rev. B.* **44**, 943–954 (1991).

72. J. P. Perdew, K. Burke, M. Ernzerhof, Generalized gradient approximation made simple (vol 77, pg 3865, 1996). *Phys. Rev. Lett.* **78**, 1396 (1997).

73. S. L. Dudarev, G. A. Botton, S. Y. Savrasov, C. J. Humphreys, A. P. Sutton, Electron-energy-loss spectra and the structural stability of nickel oxide: An LSDA+U study. *Phys. Rev. B.* **57**, 1505–1509 (1998).

74. D. Vanderbilt, Soft Self-Consistent Pseudopotentials in a Generalized Eigenvalue Formalism. *Phys. Rev. B.* **41**, 7892–7895 (1990).

75. The vanadium pseudopotential has a reference state of $3s^2$ $3p^6$ $3d^3$ $4s^2$ $4p^0$, cutoff radii (in au) of 2.1,2.0,2.1,2.2,2.0, respectfully, and a local cutoff radius of 1.8 au (the r_{inner} was not reported). The oxygen pseudopotential reference state was $2s^2$ $2p^4$ $3d^0$, cutoff radii of 1.7, 1.7, 1.4, respectfully, and a local cutoff radius and r_{inner} of 1.4.

76. H. J. Monkhorst, J. D. Pack, Special Points for Brillouin-Zone Integrations. *Phys. Rev. B.* **13**, 5188–5192 (1976).

77. A. Togo, F. Oba, I. Tanaka, First-principles calculations of the ferroelastic transition between rutile-type and $CaCl_2$-type SiO_2 at high pressures. *Phys. Rev. B.* **78**, 134106 (2008).

78. V. Eyert, The metal-insulator transitions of VO2: A band theoretical approach. *Ann. Phys.* **11**, 650 (2002).

79. M. Sternik, K. Parlinski, Lattice vibrations in cubic, tetragonal, and monoclinic phases of ZrO_2. *J. Chem. Phys.* **122**, 64707 (2005).

80. A. V Ilinskiy, O. E. Kvashenkina, E. B. Shadrin, Phase transition and correlation effects in vanadium dioxide. *Semiconductors.* **46**, 422–429 (2012).

81. S. Shin *et al.*, Vacuum-Ultraviolet Reflectance and Photoemission-Study of the Metal-Insulator Phase-Transitions in VO_2, V_6O_{13}, and V_2O_3. *Phys. Rev. B.* **41**, 4993–5009 (1990).

82. W. G. Spitzer, R. C. Miller, L. E. Howarth, D. A. Kleinman, *Phys. Rev.*, in press.

83. J. Wu *et al.*, Strain-induced self organization of metal-insulator domains in single-crystalline VO_2 nanobeams. *Nano Lett.* **6**, 2313–2317 (2006).

84. D. Kucharczyk, T. Niklewski, Accurate X-Ray Determination of the Lattice-Parameters and the Thermal-Expansion Coefficients of VO_2 Near the Transition-Temperature. *J. Appl. Crystallogr.* **12**, 370–373 (1979).

85. C. R. Everhart, J. B. Macchesn, Anisotropy in Electrical Resistivity of Vanadium Dioxide Single Crystals. *J. Appl. Phys.* **39**, 2872 (1968).

86. M. M. Qazilbash *et al.*, Mott transition in VO_2 revealed by infrared spectroscopy and nano-imaging. *Science (80-.).* **318**, 1750–1753 (2007).

87. M. M. Qazilbash *et al.*, Infrared spectroscopy and nano-imaging of the insulator-to-metal transition in vanadium dioxide. *Phys. Rev. B.* **79**, 75107 (2009).

88. Y. Liu *et al.*, Negative pressure induced ferroelectric phase transition in rutile TiO_2. *J. Phys. Condens. Matter.* **21**, 275901 (2009).

89. M. Imada, A. Fujimori, Y. Tokura, Metal-insulator transitions. *Rev. Mod. Phys.* **70**, 1039–1263 (1998).

90. A. Perucchi, L. Baldassarre, P. Postorino, S. Lupi, Optical properties across the insulator to metal transitions in vanadium oxide compounds. *J. Physics-Condensed Matter.* **21**, 323202 (2009).

91. D. N. Basov, R. D. Averitt, D. van der Marel, M. Dressel, K. Haule, Electrodynamics of correlated electron materials. *Rev. Mod. Phys.* **83**, 471–541 (2011).

92. A. X. Gray *et al.*, Correlation-Driven Insulator-Metal Transition in Near-Ideal Vanadium Dioxide Films. *Phys. Rev. Lett.* **116**, 1–6 (2016).

93. M. Gatti, F. Sottile, L. Reining, Electron-hole interactions in correlated electron materials: Optical properties of vanadium dioxide from first principles. *Phys. Rev. B.* **91**, 195137 (2015).

94. H. Zheng, L. K. Wagner, Computation of the Correlated Metal-Insulator Transition in Vanadium Dioxide from First Principles. *Phys. Rev. Lett.* **114** (2015).

95. R. Eguchi *et al.*, Photoemission evidence for a Mott-Hubbard metal-insulator transition in VO_2. *Phys. Rev. B - Condens. Matter Mater. Phys.* **78**, 1–6 (2008).

96. D. Wegkamp *et al.*, Instantaneous band gap collapse in photoexcited monoclinic VO_2 due to photocarrier doping. *Phys. Rev. Lett.* **113**, 2–6 (2014).

97. B. T. O'Callahan *et al.*, Inhomogeneity of the ultrafast insulator-to-metal transition dynamics of VO_2. *Nat. Commun.* **6**, 6849 (2015).

98. D. Wegkamp, J. Stähler, Ultrafast dynamics during the photoinduced phase transition in VO_2. *Prog. Surf. Sci.* **90**, 464–502 (2015).

99. B. Mayer *et al.*, Tunneling breakdown of a strongly correlated insulating state in VO_2 induced by intense multiterahertz excitation. *Phys. Rev. B.* **91**, 235113 (2015).

100. T. J. Huffman *et al.*, Modification of electronic structure in compressively strained vanadium dioxide films. *Phys. Rev. B.* **91**, 205140 (2015).

101. M. Nazari *et al.*, Temperature dependence of the optical properties of VO_2 deposited on sapphire with different orientations. *Phys. Rev. B.* **87**, 35142 (2013).

102. T. Kong, M. W. Masters, S. L. Bud'ko, P. C. Canfield, Physical properties of $V_{1-x}Ti_xO_2$ ($0 < x < 0.187$) single crystals. *APL Mater.* **3**, 41502 (2015).

103. E. Strelcov *et al.*, Doping-based stabilization of the M2 phase in free-standing VO_2 nanostructures at room temperature. *Nano Lett.* **12**, 6198–205 (2012).

104. J. P. Dhaenens, D. Kaplan, P. Merenda, Electron-Spin Resonance in $V_{1-X}Cr_XO_2$. *J. Phys. C-Solid State Phys.* **8**, 2267–2273 (1975).

105. B. S. Mun *et al.*, Observation of insulating-insulating monoclinic structural transition in macro-sized VO_2 single crystals. *Phys. status solidi - Rapid Res. Lett.* **5**, 107–109 (2011).

106. B. S. Mun *et al.*, Nonpercolative metal-insulator transition in VO_2 single crystals. *Phys. Rev. B.* **84**, 113109 (2011).

107. T. M. Rice, H. Launois, J. P. Pouget, Comment on VO_2 - Peierls Or Mott-Hubbard - a View from Band Theory. *Phys. Rev. Lett.* **73**, 3042 (1994).

108. C. Marini *et al.*, Optical properties of $V_{1-x}Cr_xO_2$ compounds under high pressure. *Phys. Rev. B.* **77**, 235111 (2008).

109. J. Cao *et al.*, Extended mapping and exploration of the vanadium dioxide stress-temperature phase diagram. *Nano Lett.* **10**, 2667–73 (2010).

110. J. Heyd, G. E. Scuseria, M. Ernzerhof, Hybrid functionals based on a

screened Coulomb potential. *J. Chem. Phys.* **118**, 8207–8215 (2003).

111. J. Heyd, G. E. Scuseria, M. Ernzerhof, Hybrid functionals based on a screened Coulomb potential (vol 118, pg 8207, 2003). *J. Chem. Phys.* **124** (2006).

112. G. Kresse, J. Hafner, Ab initio molecular-dynamics for liquid-metals. *Phys. Rev. B.* **47**, 558–561 (1993).

113. G. Kresse, J. Furthmuller, Efficient iterative schemes for ab initio total-energy calculations using a plane-wave basis set. *Phys. Rev. B.* **54**, 11169 (1996).

114. G. Kresse, J. Furthmuller, Efficiency of ab-initio total energy calculations for metals and semiconductors using a plane-wave basis set. *Comput. Mater. Sci.* **6**, 15–50 (1996).

115. G. Kresse, D. Joubert, From ultrasoft pseudopotentials to the projector augmented-wave method. *Phys. Rev. B.* **59**, 1758–1775 (1999).

116. J. He, C. Franchini, Screened hybrid functional applied to $3d^0$ -> $3d^8$ transition-metal perovskites $LaMO_3$(M = Sc-Cu): Influence of the exchange mixing parameter on the structural, electronic, and magnetic properties. *Phys. Rev. B.* **86**, 235117 (2012).

117. N. F. Quackenbush *et al.*, Stability of the M_2 phase of vanadium dioxide induced by coherent epitaxial strain. *Phys. Rev. B.* **94**, 85105 (2016).

118. D. C. Johnston, The puzzle of high temperature superconductivity in layered iron pnictides and chalcogenides. *Adv. Phys.* **59**, 803–1061 (2010).

119. E. Dagotto, Complexity in strongly correlated electronic systems. *Science (80-.).* **309**, 257–262 (2005).

120. J. M. Atkin *et al.*, Strain and temperature dependence of the insulating phases of VO_2 near the metal-insulator transition. *Phys. Rev. B.* **85**, 20101 (2012).

121. N. B. Aetukuri *et al.*, Control of the metal–insulator transition in vanadium dioxide by modifying orbital occupancy. *Nat. Phys.* **9**, 661–666 (2013).

122. D. Paquet, P. Lerouxhugon, Electron Correlations and Electron-Lattice Interactions in the Metal-Insulator, Ferroelastic Transition in VO_2 - a Thermodynamical Study. *Phys. Rev. B.* **22**, 5284–5301 (1980).

123. K. G. West *et al.*, Growth and characterization of vanadium dioxide thin films prepared by reactive-biased target ion beam deposition. *J. Vac. Sci. Technol. A Vacuum, Surfaces, Film.* **26**, 133 (2008).

124. S. Kittiwatanakul *et al.*, Transport behavior and electronic structure of phase pure VO_2 thin films grown on c-plane sapphire under different O_2 partial pressure. *J. Appl. Phys.* **114**, 53703 (2013).

125. R. A. Aliev *et al.*, Effect of grain sizes on the metal-semiconductor phase transition in vanadium dioxide polycrystalline thin films. *Phys. Solid State.* **48**,

929–934 (2006).
126. H. Windischmann, Intrinsic Stress in Sputter-Deposited Thin Films. *Crit. Rev. Solid State Mater. Sci.* **17**, 547–596 (1992).
127. W. Y. Park, K. H. Ahn, C. S. Hwang, Effects of in-plane compressive stress on electrical properties of (BaSr)TiO_3 thin film capacitors prepared by on- and off-axis rf magnetron sputtering. *Appl. Phys. Lett.* **83**, 4387 (2003).
128. T. Ashida, K. Kato, H. Omoto, A. Takamatsu, Internal Stress and Microstructure of Zinc Oxide Films Sputter-Deposited with Carbon Dioxide Gas. *Jpn. J. Appl. Phys.* **49**, 65501 (2010).
129. G. Andersson, Studies on Vanadium Oxides. 2. the Crystal Structure of Vanadium Dioxide. *Acta Chem. Scand.* **10**, 623–628 (1956).
130. Y. Muraoka, Y. Ueda, Z. Hiroi, Large modification of the metal insulator transition temperature in strained VO_2 fims grown on TiO_2 substrates. *J. Phys. Chem. Solids.* **63**, 965–967 (2002).
131. A. H. Jay, The Thermal Expansion of Quartz by X-ray Measurements. *Proc. R. Soc. London.* **142**, 237–247 (1933).
132. E. Radue *et al.*, Effect of a substrate-induced microstructure on the optical properties of the insulator-metal transition temperature in VO_2 thin films. *J. Appl. Phys.* **113**, 233104 (2013).
133. J. Laverock *et al.*, Strain dependence of bonding and hybridization across the metal-insulator transition of VO_2. *Phys. Rev. B.* **85**, 81104 (2012).
134. S. Biermann, A. Georges, A. Lichtenstein, T. Giamarchi, Deconfinement transition and Luttinger to Fermi liquid crossover in quasi-one-dimensional systems. *Phys. Rev. Lett.* **87**, 276405 (2001).
135. C. Sommers, R. de Groot, D. Kaplan, A. Zylbersztejn, Cluster calculations of the electronic *d*-states of VO_2. *J. Phys. Lettres.* **36**, L157–L160 (1975).
136. S. Hormoz, S. Ramanathan, Limits on vanadium oxide Mott metal–insulator transition field-effect transistors. *Solid. State. Electron.* **54**, 654–659 (2010).
137. H. Zhou *et al.*, Optical and electrical switching properties of VO_2 thin film on MgF_2 (111) substrate. *Ceram. Int.* **42**, 7655–7663 (2016).
138. T. Slusar, J. C. Cho, B. J. Kim, S. J. Yun, H. T. Kim, Epitaxial growth of higher transition-temperature VO_2 films on AlN/Si. *APL Mater.* **4** (2016).
139. T. Driscoll, H.-T. T.-T. Kim, B.-G. G. Chae, M. Di Ventra, D. N. Basov, Phase-transition driven memristive system. *Appl. Phys. Lett.* **95**, 2–5 (2009).
140. L. Pellegrino *et al.*, Multistate Memory Devices Based on Free-standing VO_2/TiO_2 Microstructures Driven by Joule Self-Heating. *Adv. Mater.* **24**, 2929–2934 (2012).

141. Z. Yang, C. Ko, V. Balakrishnan, G. Gopalakrishnan, S. Ramanathan, Dielectric and carrier transport properties of vanadium dioxide thin films across the phase transition utilizing gated capacitor devices. *Phys. Rev. B.* **82** (2010).

142. W. A. Vitale *et al.*, Electrothermal actuation of vanadium dioxide for tunable capacitors and microwave filters with integrated microheaters. *Sens. Actuat A-Phys.* **241**, 245–253 (2016).

143. M. A. Kats *et al.*, Ultra-thin perfect absorber employing a tunable phase change material. *Appl. Phys. Lett.* **101** (2012).

144. T. Hanaguri *et al.*, A "checkerboard" electronic crystal state in lightly hole-doped $Ca_{2-x}Na_xCuO_2Cl_2$. *Nature.* **430**, 1001–1005 (2004).

145. M. Vershinin *et al.*, Local ordering in the pseudogap state of the high-T_c superconductor $Bi_2Sr_2CaCu_2O_{8+\Delta}$. *Science (80-.).* **303**, 1995–1998 (2004).

146. L. W. Zhang, C. Israel, A. Biswas, R. L. Greene, A. de Lozanne, Direct observation of percolation in a manganite thin film. *Science (80-.).* **298**, 805–807 (2002).

147. K. Lai *et al.*, Mesoscopic Percolating Resistance Network in a Strained Manganite Thin Film. *Science (80-.).* **329**, 190–193 (2010).

148. J. Dho, Y. N. Kim, Y. S. Hwang, J. C. Kim, N. H. Hur, Strain-induced magnetic stripe domains in $La_{0.7}Sr_{0.3}MnO_3$ thin films. *Appl. Phys. Lett.* **82**, 1434–1436 (2003).

149. A. Frenzel *et al.*, Inhomogeneous electronic state near the insulator-to-metal transition in the correlated oxide VO_2. *Phys. Rev. B.* **80**, 115115 (2009).

150. M. Liu *et al.*, Symmetry breaking and geometric confinement in VO_2: Results from a three-dimensional infrared nano-imaging. *Appl. Phys. Lett.* **104**, 121905 (2014).

151. A. S. McLeod *et al.*, Nanotextured phase coexistence in the correlated insulator V_2O_3. *Nat. Phys.* **1**, 1–8 (2016).

152. J. Rensberg *et al.*, Active Optical Metasurfaces Based on Defect-Engineered Phase-Transition Materials. *Nano Lett.* **16**, 1050–1055 (2016).

153. S. J. Yun, J. W. Lim, J.-S. Noh, B.-J. Kim, H.-T. Kim, Vanadium Dioxide and Vanadium Sesquioxide Thin Films Fabricated on (0001) or (10-10)Al_2O_3 by Reactive RF-Magnetron Sputter Deposition and Subsequent Annealing Processes. *Jpn. J. Appl. Phys.* **48** (2009).

154. F. Keilmann, R. Hillenbrand, Near-field microscopy by elastic light scattering from a tip. *Philos. Trans. A. Math. Phys. Eng. Sci.* **362**, 787–805 (2004).

155. N. Ocelic, A. Huber, R. Hillenbrand, Pseudoheterodyne detection for background-free near-field spectroscopy. *Appl. Phys. Lett.* **89**, 101124 (2006).

156. S. Liu *et al.*, Random Field Driven Spatial Complexity at the Mott Transition in VO_2. *Phys. Rev. Lett.* **116**, 36401 (2016).

157. R. W. Balluffi, S. Allen, W. C. Carter, *Kinetics of Materials* (Wiley, 2005).

158. Y. Imry, M. Wortis, Influence of Quenched Impurities on 1st-Order Phase-Transitions. *Phys. Rev. B.* **19**, 3580–3585 (1979).

159. A. Sharoni *et al.*, First-order reversal curve measurements of the metal-insulator transition in VO_2: Signatures of persistent metallic domains. *Phys. Rev. B - Condens. Matter Mater. Phys.* **79**, 1–7 (2009).

160. B. S. Mun *et al.*, Observation of insulating-insulating monoclinic structural transition in macro-sized VO_2 single crystals [Phys. Status Solidi RRL 5 , No. 3, R107-R109 (2011)]. *Phys. status solidi - Rapid Res. Lett.* **9**, 206–206 (2015).

161. R. Lopez, L. A. Boatner, T. E. Haynes, R. F. Haglund, L. C. Feldman, Enhanced hysteresis in the semiconductor-to-metal phase transition of VO_2 precipitates formed in SiO_2 by ion implantation. *Appl. Phys. Lett.* **79**, 3161–3163 (2001).

162. K. Appavoo *et al.*, Role of defects in the phase transition of VO_2 nanoparticles probed by plasmon resonance spectroscopy. *Nano Lett.* **12**, 780–6 (2012).

163. J. Cao *et al.*, Strain engineering and one-dimensional organization of metal-insulator domains in single-crystal vanadium dioxide beams. *Nat. Nanotechnol.* **4**, 732–737 (2009).

164. S. A. Dönges *et al.*, Ultrafast Nanoimaging of the Photoinduced Phase Transition Dynamics in VO_2. *Nano Lett.* **16**, 3029–3035 (2016).

165. K. Okimura, T. Watanabe, J. Sakai, Stress-induced VO_2 films with M_2 monoclinic phase stable at room temperature grown by inductively coupled plasma-assisted reactive sputtering. *J. Appl. Phys.* **111**, 73514 (2012).

Vita

My love of learning was established early on by my mother and grandmother, who between them combine for almost 80 years in elementary education. Mom is still going strong. She'll make it to 45 years.

My fascination with the way things work was inspired by my grandfather. Despite an 8th grade education, he was something of a legend when it came to building and fixing things. He remains the most brilliant technical mind I've ever encountered. Any talents I may have are a shadow of his own.

I was born in Kittanning, Pennsylvania in 1987. I received my B.S. degree from Muhlenberg College in 2010. I was lucky enough to be the first graduate student through the door at Mumtaz Qazilbash's lab. There, I gained the invaluable experience and the satisfaction that comes from building a lab from the beginning. It was rarely straightforward, but it all (mostly) worked in the end. I was fortunate for the opportunity to work on vanadium dioxide for my Ph.D., one of the great and classic systems of condensed matter physics.

Publications

First Author Papers

1. T.J. Huffman *et al.* “Highly repeatable nanoscale phase coexistence in vanadium dioxide films” In Review. **arXiv:1612.00855**
2. T.J. Huffman *et al.* “*Insulating phases of vanadium dioxide are Mott-Hubbard insulators.”* Phys. Rev. B. **95**, 075125 (2017).
3. T.J. Huffman *et al.* “*Far Infrared Response of Vanadium Dioxide Microcrystals.*” Phys. Rev. B. **87**, 115121 (2013).
4. T.J. Huffman *et al.* “*Modification of electronic structure in compressively strained vanadium dioxide films.”* Phys .Rev. B. **91**, 205140 (2015).

Other Papers

1. Peng Xu *et al.* “*Novel aspects of charge and lattice dynamics in the hole doped manganite* $La_{0.67}Sr_{0.33}MnO_3$.” Phil. Mag. **95**, 2078 (2015).
2. Z. Xing *et al.* “*Role of electron-electron interactions in the charge dynamics of rare-earth doped* $CaFe_2As_2$.*”* Phys. Rev. B. **94**, 064514 (2016).